2

Solid State Research

1968

Lincoln Laboratory

MASSACHUSETTS INSTITUTE OF TECHNOLOGY

Lexington, Massachusetts

|	2
Solid State Research	1968 Issued 10 July 1968
Lincoln Laboratory MASSACHUSETTS INSTITUTE OF TECHNOLOGY Lexington, Massachusetts	

ABSTRACT

This report covers in detail the solid state research work at Lincoln
Laboratory for the period 1 February through 30 April 1968. The
topics covered are Solid State Device Research, Optical Techniques
and Devices, Materials Research, and Physics of Solids.
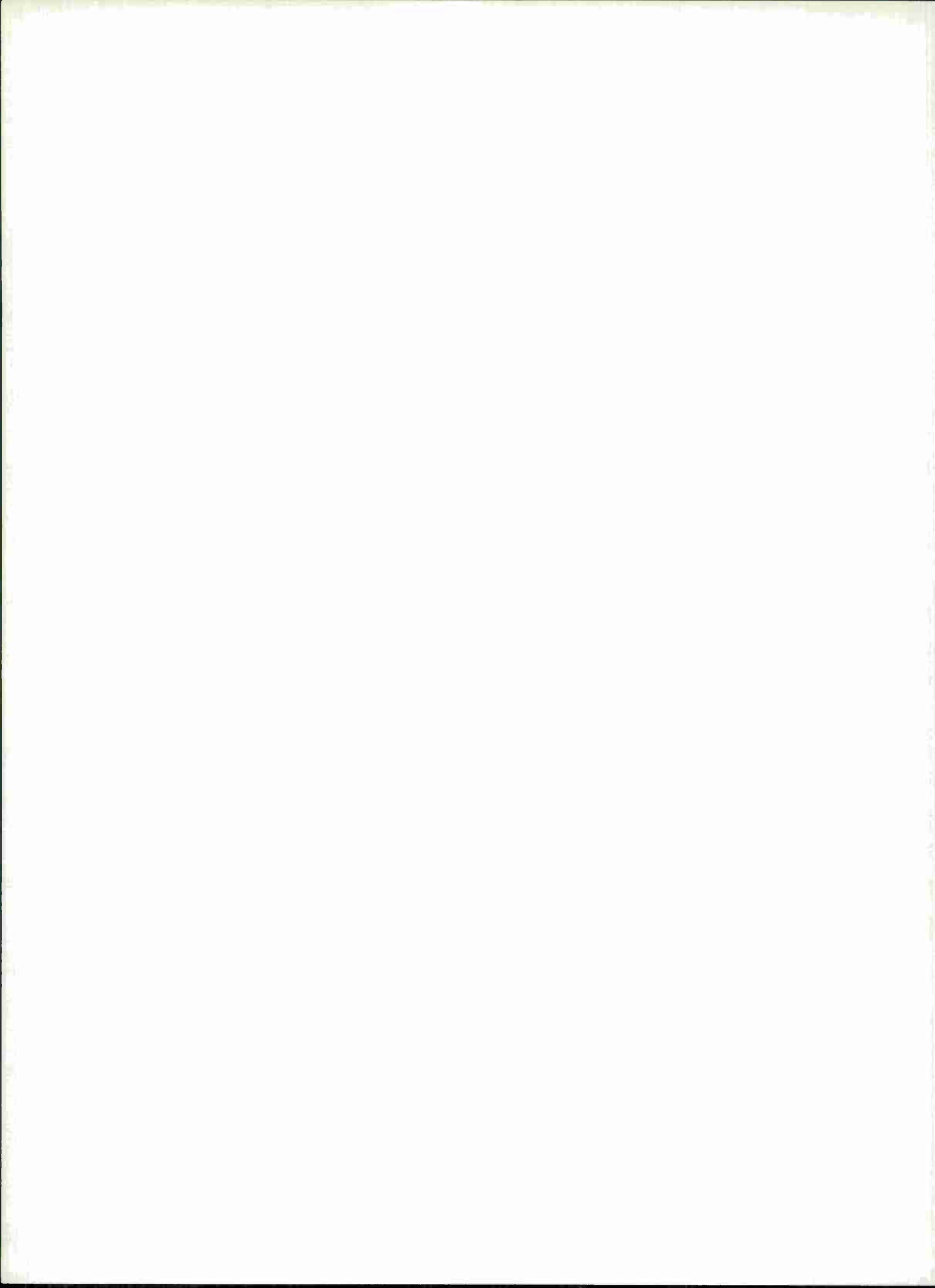
INTRODUCTION

1. SOLID STATE DEVICE RESEARCH

Photovoltaic detectors with long-wavelength cutoffs up to 20 μ at 77°K and up to 30 μ at 12°K have been produced from annealed Bridgman-grown and vapor-grown $Pb_{1-x}Sn_xTe$ crystals in the $0 < x < 0.25$ composition range. Responsivities as high as 190 V/W, detectivities of nearly 10^{10} cm/W sec$^{1/2}$, and external quantum efficiencies up to 37 percent have been obtained at wavelengths up to 12 μ in diodes operated at 77°K. Detectivities at 12°K were generally about an order of magnitude higher than at 77°K.

Photoconductivity at wavelengths up to 15 μ has been observed at 77°K in Bridgman-grown and subsequently annealed crystals of $Pb_{1-x}Sn_xTe$ which had carrier concentrations as low as 2×10^{15} cm^{-3} and 77°K mobilities of about 3×10^4 cm^2/V sec. Detectivity values between 10^8 and 10^9 cm/W sec$^{1/2}$ at 77°K and 10^{10} cm/W sec$^{1/2}$ at 4.2°K were measured. Photoconductive lifetimes of about 10^{-8} and 10^{-6} sec were obtained at the two respective temperatures.

Diode lasers with low thresholds and emission wavelengths up to 28.1 μ have been fabricated from vapor-grown single crystals of $Pb_{1-x}Sn_xTe$ containing Bi as the dominant donor impurity. For $x \geqslant 0.2$, 77°K threshold current densities were less than 1500 A cm^{-2}. With pulse bias, a peak power output of 0.1 W and an external quantum efficiency η_x of 0.08 were observed in a $Pb_{0.8}Sn_{0.2}Te$ diode at 12°K, and a peak power of 0.03 W with $\eta_x = 0.01$ was measured at 77°K. With CW operation at 12°K, 5×10^{-3} W with $\eta_x = 0.03$ was obtained.

Extrinsic far-infrared photoconductivity has been observed at 4.2°K in high-purity n-type epitaxial layers of GaAs grown on Cr-doped semi-insulating GaAs substrates. Responsivities as high as 5×10^3 and 4×10^4 V/W have been measured at 195 and 337 μ, respectively. At 902 μ, the responsivity dropped to 9×10^2 V/W. Measurements of the noise in the detection system at 300 Hz in a 1-Hz bandwidth yield an NEP of 1.2×10^{-11} W at 195 μ, 1.4×10^{-12} W at 337 μ, and 6×10^{-11} W at 902 μ. The time constant of the detector has been determined to be shorter than 1 μsec using a Ge avalanche modulator to chop the incident radiation. A time constant of about 5 nsec was measured using impact impurity ionization in the GaAs.

We have found that proton radiation damage can be used to convert both p- and n-type GaAs into high-resistivity material, and have used this technique to isolate p-n junctions on a diffused GaAs substrate and also to prevent edge breakdown in Au-GaAs Schottky barriers. This technique of creating high-resistivity material should be useful for the fabrication of structures in which thin high-resistivity layers are required.

The photovoltaic response of InSb-MOS detectors to modulated 3.9-μ radiation from an InAs diode emitter has been measured at 77°K following irradiation with short wavelength light in the energy range between 1 and 5 eV. Effects are observed due to trapping and detrapping of electronic charge at oxide states and/or at oxide-InSb interface states; however, the precise model for this trapping has not yet been determined.

II. OPTICAL TECHNIQUES AND DEVICES

The 100-W CO_2 laser amplifier has been operated in the sealed-off mode and yields an output of 88 W compared with 114 W using a flowing gas mixture. The output beam pattern is a close reproduction of the input TEM_{00} mode.

The 1.5-meter stable CO_2 oscillator has been used to drive the above amplifier. An output power of 10 to 15 W is obtained, and the frequency stability should be comparable to that of previous smaller versions once the output window heating is eliminated by the use of lower-loss materials.

An attempt has been made to observe thermal blooming of a $10.6-\mu$ CO_2 laser beam in an absorbing gas. Substantial blooming does occur, but difficulty has been encountered in making quantitative measurements due to the asymmetry caused by convection in our horizontal gas cell and to the lack of a good image detector at the $10-\mu$ wavelength.

Optical heterodyning at 10.6 μm between a current-tunable, single-mode $Pb_{0.88}Sn_{0.12}Te$ diode laser and a stable, single-frequency CO_2 gas laser has produced a controllable beat frequency in a Ge:Cu detector from under 50 to 1300 MHz. From these measurements, we have determined the cutoff frequency of a Ge:Cu detector considered for application in the laser radar system, and have obtained a direct indication of the linewidth of emission from the semiconductor p-n junction laser.

III. MATERIALS RESEARCH

A theoretical analysis of the forced convection method of vapor crystal growth has shown that the growth velocity is proportional to the first power of the available concentration of condensing vapor and to the square root of the carrier gas velocity. These results are supported by experimental data reported previously on the growth of iodine and camphor crystals. The condition required for stability of the growth interface has been formulated in terms of a relationship between the temperatures at the interface, at the edge of the diffusion boundary layer adjacent to the interface, and at the solid source.

Optical transmission measurements have been made at room temperature on single crystals of $Cd_{1-x}Mg_xTe$ alloys with $0 \leqslant x \leqslant 0.46$. The energy gap evaluated from the data increases linearly with increasing x, from 1.50 eV for CdTe to 2.23 eV for x = 0.46.

Photoluminescence spectra due to oxygen in $ZnTe_{1-x}Se_x$, $ZnTe_{1-x}S_x$, and $Zn_{1-x}Cd_xTe$ alloys have been measured at 4.2°K. As expected for the isoelectronic trap model of the oxygen center, the trapping energy decreases with increasing ZnSe and ZnS content, but is essentially independent of CdTe content.

The pressure-composition phase diagram for the $Ba_{1-x}Sr_xRuO_3$ system at 1000°C has been determined by x-ray diffraction measurements on powdered samples. Four different structures, with different proportions of cubic and hexagonal close packing, are observed. The addition of strontium and the application of pressure both favor structures with more cubic and less hexagonal close packing.

A method has been developed for evaluating absolute atomic form factors in solids by analysis of integrated intensity data obtained in x-ray diffraction measurements. Application of this method to data for nickel suggests a transfer of 0.3 electron from the outer levels (4s) to the first inner levels (3d), but this should be considered as a qualitative result.

IV. PHYSICS OF SOLIDS

The optical investigation of the band structure of nickel has now been extended to nickel-copper alloys. Reflection measurements, from 0.2 to 11 eV, in several alloys seem to indicate that below 4 eV the alloys behave according to a "localized states" or to a "minimum polarity" model.

The study of the effect of stress on the impurity spectrum of bismuth-doped silicon has now been completed. All measured relative intensities and transition energies as a function of stress are in agreement with predictions of a strain Hamiltonian derived from effective mass and deformation potential theory.

Two sets of interband transitions, analogous to those in HgTe, have now been observed in the magneto-reflection of gray tin. One of the lowest energy transitions does not fit into the Landau level scheme; it is suggested that this line may arise from transitions between impurity states associated with the Landau levels.

Investigation of the "extra" transitions in the interband magnetoreflection and magneto-electroreflection of InSb, caused by the warping and linear-$\vec{k}$ splitting of the valence band, has been concluded. The warping obtained is in good agreement with the cyclotron resonance results of Bagguley, et al.; the linear-$\vec{k}$ splitting is one-third the value deduced from cyclotron resonance by Robinson, but is in agreement with the theoretical estimate of Kane.

A technique has been developed for determining the Debye temperature, Θ_D, of crystals by means of thermal modulation of x-ray diffraction. This new method, which has been tested on NaCl, gives results in good agreement with other techniques, and, aside from holding promise of surpassing the accuracy of existing DC methods, has the additional advantage of yielding Θ_D from measurements at a single temperature.

Substantial amplification, greater than 25 db/cm, of 9-GHz longitudinal ultrasonic waves has been obtained in n-InSb on application of a pulsed electric field. Theoretical calculations of this effect are in reasonable qualitative agreement with the experiment.

Measurements of the magnetic properties of the high-pressure (orthorhombic) phase of MnAs have been extended to 11 kbars. The variation with temperature of the magnetic moment has been studied as a function of magnetic field and throughout the pressure range.

A study of the properties of the one-dimensional, two-sublattice model of a spiral magnetic structure has been completed. For a range of parameters, a ferrimagnetic conical spiral structure is the ground state. The spin wave spectrum for this case has been investigated.

The well-known spherical model of a ferromagnet has been shown to be thermodynamically identical to a system of infinite-dimensional spins interacting through a Heisenberg Hamiltonian.

It is known that for the Ising model, the onset of magnetic order is characterized by the collapse of the eigenvalue spectrum of a certain linear operator. It has been demonstrated that the same mathematical phenomenon characterizes the onset of ordering in a set of ν-dimensional spins interacting via a Heisenberg Hamiltonian.

Introduction

A new form of temperature-dependent Hartree-Fock theory is being investigated, based on a variational principle for the free energy. The one-electron orbitals used to construct single determinant wave functions must satisfy an equation which is more general than the usual Hartree-Fock equations. This new formulation eliminates some of the paradoxical results of ordinary temperature-dependent Hartree-Fock theory.

Using high-resolution Brillouin scattering techniques, the velocity and attenuation of 28-GHz longitudinal phonons propagating along the x-axis of α-quartz have been measured in the temperature range 300° to 600°K. Although the velocity variation with temperature agrees with the earlier ultrasonic measurements, the hypersonic attenuation agrees with theoretical extrapolations of ultrasonic data only in order of magnitude.

For the first time, light scattering has been observed from screened single-particle electron and also hole excitations. Scattering from electron excitations was found in GaAs, InP, AlSb, and CdTe, and from hole excitations in p-type GaAs doped with cadmium, zinc, and magnesium.

The study of thermal defocusing of a laser beam has now been extended to steady state (and approach to steady state) conditions. Competing conduction and convection processes have been investigated in a number of new experiments.

Methods of achieving single-mode operation of a high-power pulsed ruby laser have been explored. In the best arrangement, a single transverse mode and less than six longitudinal modes are obtained.

CONTENTS

ORGANIZATION

SOLID STATE DIVISION

A. L. McWhorter, *Head*
P. E. Tannenwald, *Associate Head*
M. J. Hudson, *Assistant*
E. P. Warekois

SOLID STATE THEORY

H. J. Zeiger, *Leader*
M. M. Litvak, *Assistant Leader*

Argyres, P. N.*	Kleiner, W. H.
Chinn, S. R.†	Landon, S. N.
Dresselhaus, G. F.	Larsen, D. M.
Hamilton, D. C.	Palm, B. J.‡
Hanus, J. G. C.	Sigel, J. L.†
Kaplan, T. A.	Stanley, H. E.
Kelley, P. L.	

OPTICS AND INFRARED

R. H. Kingston, *Leader*
R. J. Keyes, *Assistant Leader*

Bates, D. H.	McPhie, J. M.
Bostick, H. A.	Quist, T. M.
Carbone, R. J.	Ross, A. H. M.
Freed, C.	Sullivan, F. M.
Gilmartin, T. J.	Swezey, L. W.
Hinkley, E. D.	Zimmerman, M. D.
Longaker, P. R.	

ELECTRONIC MATERIALS

J. B. Goodenough, *Leader*
A. J. Strauss, *Associate Leader*

Anderson, C. H., Jr.	Kasper, H. M.
Andrews, H. I.†	LaFleur, W. J.
Arnott, R. J.	Lavine, M. C.‡
Banus, M. D.	Longo, J. M.
Batson, D. A.	Mastromattei, E. L.
Brebrick, R. F., Jr.	O'Connor, J. R.
Button, M. J.	Owens, E. B.
Capes, R. N.	Plonko, M. C.
Delaney, E. J.	Raccah, P. M.
England, R. E.	Reed, T. B.
Fahey, R. E.	Roddy, J. T.
Ferretti, A.	Searles, I. H.
Finn, M. C.	Smith, F. T. J.
Iseler, G. W.	Steininger, J. M.
Kafalas, J. A.	Wheatley, G. E.

SOLID STATE PHYSICS

J. G. Mavroides, *Leader*
G. B. Wright, *Assistant Leader*

Brandt, R. C.	Krag, W. E.
Burke, J. W.	Melngailis, J.
Carman, R. L.†	Menyuk, N.
Crooker, P. P.	Murphy, H. C.
Dresselhaus, M. S.*	Nill, K. W.
Dwight, K., Jr.	Parker, C. D.
Feinleib, J.	Perry, F. H.
Feldman, B.	Pine, A. S.
Fulton, M. J.	Scouler, W. J.
Groves, S. H.	Stickler, J. J.†
Henrich, V. E.	Strahm, N. D.†
Johnson, E. J.	Tichovolsky, E. J.†
Kernan, W. C.	Waldman, J.†
Kolesar, D. F.	Weber, R.

APPLIED PHYSICS

J. O. Dimmock, *Leader*
T. C. Harman, *Assistant Leader*
I. Melngailis, *Assistant Leader*

Brueck, S. R. J.†	Donnelly, J. P.	Oliver, M. R.†
Butler, J. F.	Ferrante, G. A.	Paladino, A. E.
Calawa, A. R.	Foyt, A. G.	Phelan, R. J., Jr.
Carter, F. B.	Hurwitz, C. E.	Stillman, G. E.
Caswell, F. H.	Lindley, W. T.	Ward, J. H. R., III
Clough, T. F.	Mooradian, A.	Wolfe, C. M.
Donaldson, P. L.	Murphy, R. A.†	Youtz, P.

---

* Leave of Absence

† Research Assistant

‡ Part Time

REPORTS BY AUTHORS
ENGAGED IN SOLID STATE RESEARCH

15 February through 15 May 1968

PUBLISHED REPORTS

Journal Articles*

JA No.			
3104	Shallow Donor Levels of InSb in a Magnetic Field	D. M. Larsen	J. Phys. Chem. Solids 29, 271 (1968)
3108	Magnetic Properties of $La_{0.5}Sr_{0.5}CoO_3$ Near Its Curie Temperature	N. Menyuk P. M. Raccah K. Dwight	Phys. Rev. 166, 510 (1968)
3119	Tellurium Vapor Pressure and Optical Density at 370-615°C	R. F. Brebrick	J. Phys. Chem. 72, 1032 (1968)
3137	Metallurgical and Electronic Properties of $Pb_{1-x}Sn_xTe$, $Pb_{1-x}Sn_xSe$, and Other IV-VI Alloys	A. J. Strauss	Trans. Met. Soc. AIME 242, 354 (1968)
3140	Crystal Growth, Annealing, and Diffusion of Lead-Tin Chalcogenides	A. R. Calawa T. C. Harman M. C. Finn P. Youtz	Trans. Met. Soc. AIME 242, 374 (1968)
3150	Spin-Wave Resonance	R. Weber	IEEE Trans. Magnetics MAG-4, 28 (1968)
3154	Magnetic Ordering and the Electronic Properties of the Heavy Rare-Earth Metals	R. E. Watson[†] A. J. Freeman[†] J. O. Dimmock	Phys. Rev. 167, 497 (1968)
3161	Growth of Single Crystals of ZnTe and $ZnTe_{1-x}Se_x$ by Temperature Gradient Solution Zoning	J. M. Steininger R. E. England	Trans. Met. Soc. AIME 242, 444 (1968)
3176	Dependence of Critical Properties on Dimensionality of Spins	H. E. Stanley	Phys. Rev. Letters 20, 589 (1968)
3185	Self-Trapping in Media with Saturation of the Nonlinear Index	T. K. Gustafson[†] P. L. Kelley R. Y. Chiao[†] R. G. Brewer[†]	Appl. Phys. Letters 12, 165 (1968)

---

* Reprints available.

† Author not at Lincoln Laboratory.

JA No.

3187	Isotope Effect in Superconducting Rhenium	E. Maxwell[*] M. Strongin[*] T. B. Reed	Phys. Rev. 166, 457 (1968)
3191	Continuous Operation of a Long-Lived CO_2 Laser Tube	R. J. Carbone	IEEE J. Quant. Electron. QE-4, 102 (1968)
3196	Comments on "Standing Spin-Wave Resonance in 'Flash-Evaporated' Permalloy Films"	P. E. Tannenwald R. Weber	Phys. Rev. Letters 20, 918 (1968)
3213	Time Dependence in the Thermal Blooming of Laser Beams	R. L. Carman P. L. Kelley	Appl. Phys. Letters 12, 241 (1968)
3230	Linear-$\vec{k}$ Valence Band Splitting in InSb	C. R. Pidgeon[*] S. H. Groves	Phys. Rev. Letters 20, 1003 (1968)
3237	Observation of Interband Transitions in Arsenic	M. Maltz[*] M. S. Dresselhaus	Phys. Rev. Letters 20, 919 (1968)

MS No.

1857	An Effective Hamiltonian for the Optical Properties of Silicon and Germanium	G. F. Dresselhaus M. S. Dresselhaus	Intl. J. Quant. Chem. 1S, 595 (1967)
1859B	The Virial Theorem for a System of Interacting Particles Under External Forces and Constraints	P. N. Argyres	Intl. J. Quant. Chem. 1S, 699 (1967)
1943	Analysis of Distant-Neighbor Interactions in Cubic Spinels	K. Dwight N. Menyuk	J. Appl. Phys. 39, 660 (1968)
1945	Nuclear Magnetic Resonance and Magnetization Studies of $CdCr_2Se_4$	G. H. Stauss[*] M. Rubinstein[*] J. Feinleib K. Dwight N. Menyuk A. Wold[*]	J. Appl. Phys. 39, 667 (1968)
1954	Localized vs Collective Descriptions of Magnetic Electrons	J. B. Goodenough	J. Appl. Phys. 39, 403 (1968)
1955	Magnetic Properties of $SrRuO_3$ and $CaRuO_3$	J. M. Longo P. M. Raccah J. B. Goodenough	J. Appl. Phys. 39, 1327 (1968)
1956	A Localized-Electron to Collective-Electron Transition in the System $(La, Sr) CoO_3$	P. M. Raccah J. B. Goodenough	J. Appl. Phys. 39, 1209 (1968)

---

[*] Author not at Lincoln Laboratory.

Reports

UNPUBLISHED REPORTS

Journal Articles

* Author not at Lincoln Laboratory.

JA No.

3240	Long Wavelength Infrared $Pb_{1-x}Sn_xTe$ Diode Lasers	J. F. Butler T. C. Harman	Accepted by Appl. Phys. Letters
3249	Effect of Pressure on the Structure and Magnetic Properties of $RbNiF_3$	J. A. Kafalas J. M. Longo	Accepted by Materials Res. Bull.
3260	Band Antiferromagnetism and the New Perovskite $CaCrO_3$	J. B. Goodenough J. M. Longo J. A. Kafalas	Accepted by Materials Res. Bull.
MS-2282	Interpolation Methods for Phonon Spectra in Crystals	G. F. Dresselhaus M. S. Dresselhaus	Accepted by Intl. J. Quant. Chem.

Meeting Speeches*

MS No.

1719F	Interstellar OH Maser Emission	M. M. Litvak	Seminar, M. I. T., 10 May 1968
1882D	Raman Scattering from Elementary Excitations	A. Mooradian	Seminar, M. I. T., 5 April 1968
1882E	Raman Scattering from Plasmons and Phonons	G. B. Wright	Seminar, Southern Illinois University, 26 February 1968
2141B	Zero Gap Semiconductors	S. H. Groves	Seminar, Lowell Technological Institute, 3 April 1968
2161	Spark Source Mass Spectroscopy, Recent Developments and Present Capabilities	E. B. Owens	American Chemical Society, San Francisco, 1 April 1968
2165	Polymorphism in Ag_2Te at High Pressures and Temperatures	M. D. Banus M. C. Finn	
2176	Metallic Inclusions and Low Angle Grain Boundaries in $Pb_{1-x}Sn_xTe$ Crystals	J. F. Butler T. C. Harman	Electrochemical Society, Boston, 5 – 9 May 1968
2179	Si-Te System: Partial Pressures and Thermodynamic Properties from Optical Density of the Vapor Phase	R. F. Brebrick	
2166	Electronic Raman Scattering from Impurities in Semiconductors	G. B. Wright A. Mooradian	
2174	The Two Phonon Infrared and Raman Spectrum of CdTe	A. Mooradian G. B. Wright	American Physical Society, Berkeley, California, 18 – 21 March 1968
2183A	Interband Magnetoreflection of Gray Tin	S. H. Groves C. R. Pidgeon[†] A. W. Ewald[†] R. J. Wagner[†]	

* Titles of Meeting Speeches are listed for information only. No copies are available for distribution.

† Author not at Lincoln Laboratory.

Reports

---

[*] Author not at Lincoln Laboratory.

MS No.

2208	Some Properties of LCAO Bloch Functions	H. E. Stanley J. Hanus T. A. Kaplan W. H. Kleiner	
2210	Finite Temperature Single-Determinant Theory	T. A. Kaplan	
2211	Optical Properties of Ni-Cu Alloys at 300 and 77°K from .2-11 eV	W. J. Scouler J. Feinleib J. Hanus	American Physical Society, Berkeley, California, 18 – 21 March 1968
2261	Band Approach to the Transition Metal Oxides	J. Feinleib	
2264A	The d-Electrons in Thiospinels	J. B. Goodenough	
2190	Like-Atom Cluster Formation and Elastic Memory in TiNi	J. B. Goodenough	International Conference on Metal-Nonmetal Transition, San Francisco, 14 – 16 March 1968
2212	The Present Position of Solids Mass Spectroscopy in Trace Analysis	E. B. Owens	American Chemical Society, Bayside, New York, 5 April 1968
2251	Homogeneity Range of Bi_2Te_3 from Optical Density of the Vapor	R. F. Brebrick	American Physical Society, Washington, D. C., 22 – 25 April 1968
2252	Magnetic Properties of MnAs Under Pressure	N. Menyuk J. A. Kafalas K. Dwight J. B. Goodenough	
2264	Band Structure and Magnetic Interactions in Transition-Metal Chalcogenide Spinels	J. B. Goodenough	AIME Annual Meeting, New York, 25 – 29 February 1968
2266	Raman Scattering from Plasmons in Semiconductors	A. L. McWhorter	American Physical Society, Boston, 26 – 28 February 1968
2267	Growth, Properties and Band Structure of $Pb_{1-x}Sn_xTe$ and $Pb_{1-y}Sn_ySe$	T. C. Harman	Conference on Semimetals and Narrow Gap Semiconductors, University of Durham, England, 2 – 4 April 1968
2277	Electronic Structure of Transition Metals	J. Hanus	Colloquium, Brandeis University, 5 March 1968
2278	CO_2 Laser Radar	R. H. Kingston	Seminar, United Aircraft, East Hartford, Connecticut, 7 March 1968
2281	Uses of an Ultra High Power Glass Laser for Basic Research	R. L. Carman	Seminar, Naval Research Laboratory, Washington, D. C., 19 March 1968

Reports

2282	Fourier Expansions for the Electronic Energy Bands in Solids	G. F. Dresselhaus	Seminar, University of Illinois, 22 March 1968
2284	Crystal Growth Research at the M. I. T. Lincoln Laboratory	T. B. Reed	Seminar, Texas Instruments, Incorporated, Attleboro, Massachusetts, 21 March 1968
2285	Recent Results in the Statistical Mechanics of Magnetism	H. E. Stanley	Seminar, University of California, 22 March 1968
2293	Thermal Blooming — Theory and Experiment	R. L. Carman	Seminar, M. I. T., 29 March 1968
2296	Hydrodynamic Modes and Propagation of Intense Light Beams in Liquids and Gases	P. L. Kelley	Seminar, Harvard University, 10 April 1968
2299	Exact Solution for a Linear Chain of Isotropically Interacting Classical Spins of Arbitrary Dimensionality	H. E. Stanley	19th Statistical Mechanics Meeting, Yeshiva University, 10 April 1968
2302	Raman Scattering from Plasmons, Phonons, and Impurities in Semiconductors	G. B. Wright	Seminar, Westinghouse Electric Corporation, Pittsburgh, Pennsylvania, 25 April 1968
2305	Fermi Liquid Effects on Plasma Wave Propagation in Metals	A. L. McWhorter	Seminar, M. I. T., 12 April 1968
2324	Polarons in Indium Antimonide	D. M. Larsen	Seminar, Northeastern University, 7 May 1968

I. SOLID STATE DEVICE RESEARCH

A. PHOTOVOLTAIC DETECTORS OF $Pb_{1-x}Sn_xTe$

Photovoltaic detectors with significantly improved sensitivity have been fabricated from vapor-grown $Pb_{1-x}Sn_xTe$ with compositions between $x = 0.17$ and 0.20, for which the cutoff wavelength at $77°K$ falls in the 8- to 14-μ atmospheric window. The detectivity has been improved by increasing both the quantum efficiency and the zero-bias impedance of the diodes. Most diodes were produced by a combined operation of vapor-growth, annealing, and diffusion which was performed in an evacuated ampoule by varying the temperature. The samples were then cleaved, contacts were made by gold-plating, and leads were attached with a Ga-In alloy. The junctions were 5 to 40μ deep. In most cases, the deeper junctions had higher zero-bias impedances. This seems to correlate with the absence of metallic inclusions from the bulk of vapor-grown crystals, as opposed to regions near the surface where high densities of inclusions have been detected by etching. In order to remove damaged layers from the cleaved faces and to reduce the junction depth, the diodes were stream-etched with an electrolytic solution consisting of 20 g KOH, 45 ml H_2O, 35 ml glycerin, and 20 ml of ethanol.

TABLE I-1 PROPERTIES OF $Pb_{1-x}Sn_xTe$ DETECTORS						
Area (mm^2)	Temperature (°K)	Cutoff Wavelength (μ)	Incremental Resistance (ohms)	Efficiency	Peak Responsivity (V/W)	Peak Detectivity (cm/W sec$^{1/2}$)
0.1	77	9.5	180	0.14	190	5.3×10^9
0.25	77	11	16	0.17	27	4×10^9
0.2	77	10	10	0.33	26	3.5×10^9
0.1	77	12	16	0.37	70	7.5×10^9
0.17	77	10	25	0.32	64	8×10^9
0.18	77	12	10	0.19	18	3.7×10^9
			8	0.43	32	$6.8 \times 10^{9*}$
*After antireflection coating with Se.						

Table I-1 gives representative values of responsivity, detectivity, and efficiency that have been obtained. In the case of the last detector in the Table, an antireflection coating of Se (1/4 wavelength thickness at 10μ) was applied by means of evaporation. This apparently eliminates

the reflection loss over most of the 8- to 14-μ wavelength range, thereby producing an increase by about a factor-of-two in the quantum efficiency.

A. R. Calawa   T. C. Harman
I. Melngailis   P. Youtz

B. PHOTOCONDUCTIVITY IN SINGLE-CRYSTAL $Pb_{1-x}Sn_xTe$

Photoconductivity at wavelengths up to 15 μ has been observed at 77°K in Bridgman-grown and subsequently annealed crystals of $Pb_{1-x}Sn_xTe$. The annealing parameters and the resulting carrier concentrations and mobilities of the crystals used for photoconductors are shown in Table I-2. The two compositions, $x = 0.17$ and 0.20, are of particular interest for detectors because for the 0.17 alloy the photoconductivity at 77°K peaks very close to 10.6 μ, whereas for the 0.20 alloy the peak is at 14 μ, i.e., detectors of this composition cover the 8- to 14-μ atmospheric window.

TABLE I-2						
ISOTHERMAL ANNEALING OF BRIDGMAN-GROWN $Pb_{1-x}Sn_xTe$						
Sample Number	x	Sample Temperature (°C)	Annealing Time (days)	Sample Thickness (mm)	Hall Carrier Concentration at 77°K (cm^{-3})	Hall Carrier Mobility at 77°K ($cm^2/V\,sec$)
66168C	0.17	500 450	22 38	0.29	2.3×10^{15} P	3.1×10^4
661613E2	0.17	650 450	4 50	0.27	5.8×10^{15} P	2.6×10^4
6741	0.20	600 450	8 56	0.25	7.5×10^{15} N	3.2×10^4
673R	0.17	600 450	5 14	0.06	2.6×10^{16} N	2.9×10^4

Contacts to the photoconductors were made by gold-plating and then cold-bonding leads to the gold layer using indium. The samples were then etched both to reduce their thickness and to lower the surface recombination velocity. The etch consisted of 10 parts potassium hydroxide, 1 part hydrogen peroxide, and 10 parts ethylene glycol.

In order to insure uniform cooling and to avoid the danger of thermal stresses, the samples were immersed directly in the liquid coolant in preference to mounting them on a heatsink. To insure that photoconductivity rather than slow thermal effects (bolometer effect or thermoelectric effect) are observed, the response speed was measured by using a GaAs diode laser. Figure I-1 shows the response at 77°K. The 15-nsec response time corresponds to the effective carrier lifetime. In addition to photoconductivity,
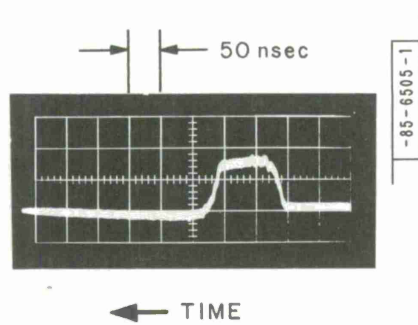
Fig. I-1. Response of $Pb_{0.83}Sn_{0.17}Te$ photoconductor at 77°K to GaAs diode laser pulse.

a photovoltaic effect is observed at the gold contacts, presumably due to the presence of a Schottky barrier. This can be eliminated by focusing the light spot on regions removed from the contacts.
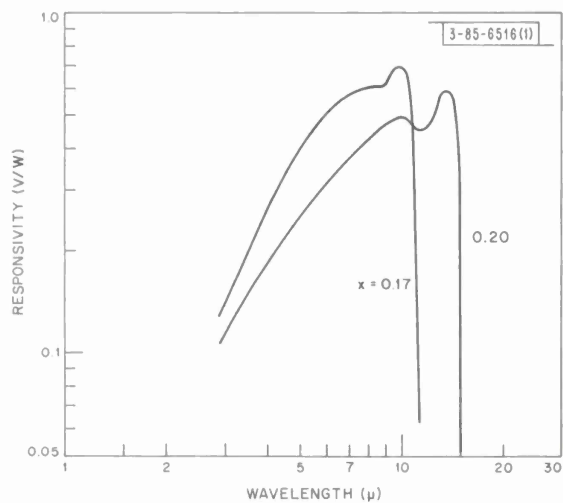
Fig. I-2. Responsivity spectra of $Pb_{1-x}Sn_xTe$ photoconductors at 77°K (samples 94A and 97A).
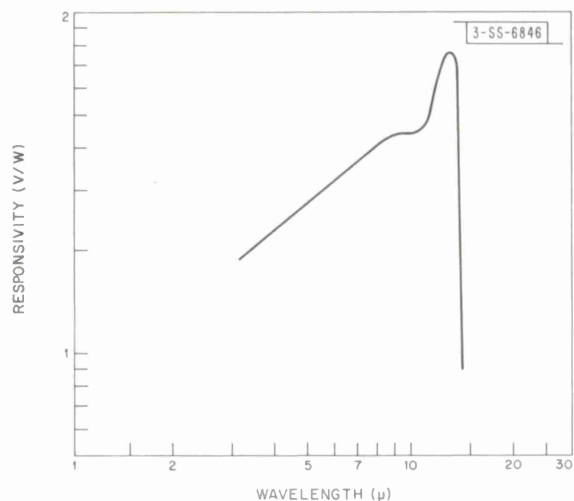
Fig. I-3. Responsivity spectrum of $Pb_{0.83}Sn_{0.17}Te$ photoconductor at 4.2°K (sample 94C).

Figure I-2 shows the response spectra of two photoconductors at 77°K — one for a 0.17 and one for a 0.20 alloy. The response peaks are at 10 and 14 µ, respectively. Near the bandgap, there is a small peak as the radiation begins to penetrate into the bulk where the lifetime of carriers is longer than near the surface. The fact that the peak is small indicates that the surface recombination velocity is not very high. This means that the effective lifetime obtained from the pulse measurements provides an approximate measure of the bulk lifetime. Figure I-3 shows the spectrum of a $Pb_{0.83}Sn_{0.17}Te$ photoconductor at 4.2°K.

Measurements of noise indicate that for some types of contacts there is a considerable current noise with a 1/f type of frequency dependence. So far, we have found that gold-plated contacts produce the least noise. For the photoconductors used at bias currents up to the point where there was evidence of heating, the measured noise was within 50 percent of the Johnson noise calculated for the resistance of the photoconductor at liquid nitrogen temperature. The generation-recombination noise was estimated to be about one order of magnitude smaller than the Johnson noise for the samples used. Hence, Johnson noise appears to be the basic noise limitation at present.

The properties of a number of photoconductors are shown in Table I-3. At the 900-Hz frequency, the noise in the first sample was about 50 percent higher than the Johnson noise for the 42-ohm resistance at 77°K. At 3000 Hz, the measured noise exceeded the Johnson noise by only 25 percent. The detectivity is given for 11 µ and 900 Hz. The peak D_λ^* at high frequencies, which is limited by thermal noise, is about 4.5×10^8 cm/W sec$^{1/2}$.

At 4.2°K, the sensitivity is greatly improved because the lifetime at 4.2° is much longer than at 77°K. Lifetime measurements obtained by observing directly the decay of the photoconductivity current following a GaAs diode laser pulse are shown in Table I-4 for a number

		Dimensions						
Sample No.	Crystal No.	Length Width Thickness (mm)	T (°K)	R (ohms)	I_o (mA)	$\mathcal{R}_v(\lambda_p)$ (V/W)	λ_p (μ)	$D^*(\lambda_p, 900, 1)$ (cm/W sec$^{1/2}$)
94A	66-16	4.0 2.0 0.05	77	42	10	0.7	10	3×10^8
94B	66-16	4.0 2.0 0.03	4.2	52	4	80	14	1.7×10^{10}
97A	67-4	1.5 1.0 0.05	77	13	30	0.6	14	1×10^8

TABLE I-3

PROPERTIES OF $Pb_{1-x}Sn_xTe$ PHOTOCONDUCTORS

TABLE I-4

LIFETIME MEASUREMENTS IN $Pb_{1-x}Sn_xTe$ PHOTOCONDUCTORS

	τ_{eff} (sec)	
T (°K)	Sample 94B	Sample 97A
300	4×10^{-8}	—
198	3×10^{-8}	$\sim 2 \times 10^{-8}$
77	1.5×10^{-8}	1.5×10^{-8}
4.2	1.2×10^{-6}	0.7×10^{-6}

of temperatures. For the crystals for which both responsivity and lifetime measurements were available, the lifetime calculated from the responsivity was in good agreement with the measured lifetime.

The direct radiative recombination lifetime at 77°K is estimated to be of the order of 10^{-5} sec in $Pb_{1-x}Sn_xTe$ with an energy gap of 0.1 eV and with a carrier concentration of the order of 10^{15} cm^{-3}; hence, additional recombination mechanisms which reduce the lifetime must be predominant in these crystals.

<div align="right">I. Melngailis
T. C. Harman</div>

C. LONG WAVELENGTH INFRARED $Pb_{1-x}Sn_xTe$ DIODE LASERS

The long wavelength limit for semiconductor lasers has been extended to $28\,\mu$ using $Pb_{1-x}Sn_xTe$ diode lasers with x up to 0.27. The p-n junctions were diffused into the vapor-grown single crystals in a special fused silica ampoule which remained sealed throughout the entire growth and diffusion-annealing processes. $Pb_{1-x}Sn_xTe$ diode lasers have previously been fabricated by a different method for $x \leqslant 0.17$ (see Ref. 1). The previous maximum wavelength for semiconductor lasers was $22.5\,\mu$, observed in a pressure-tuned PbSe laser,[2] while the long wavelength limit for unstressed semiconductor lasers was $18.8\,\mu$, obtained with $Pb_{1-y}Sn_ySe$ (Ref. 3). Threshold current densities in the present lasers were observed to be dependent on diode surface conditions and could be reduced to 50 percent or less of their original values by etching.

A schematic diagram of the special growth and diffusion-annealing ampoule is shown in Fig. I-4(a). The fused silica ampoule consists of a tubular section about 1.8 cm i.d. and 14 cm long, tapered to a point at the bottom, and with three indentations about 4 cm from the tip. The evacuated (10^{-7} torr) ampoule is suspended in a vertical tubular furnace, which has the temperature profile depicted in Fig. I-4(b). The temperature difference between the source material and vapor-grown crystals was about 1°C. The vapor source, which is a two-phased coarse powder obtained from a quenched ingot of composition $(Pb-Sn)_{0.51}Te_{0.49}$, is contained in the inner quartz tube which has a 1.0 cm i.d. and is 6.5 cm long. The crystals usually grow on the walls of the ampoule in the conical tip region. After a growing time of approximately 20 hours, the tube is air-cooled. Crystals with (100) surfaces 1 mm^2 or larger in area and of composition up to x = 0.27 have been obtained by this method. The rapidly cooled, as-grown crystals have bulk interior carrier concentrations which are given approximately by the
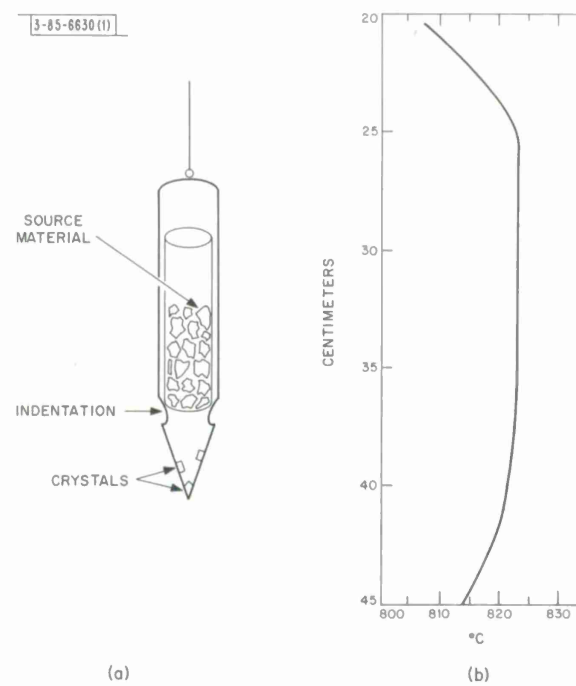
Fig. I-4. (a) Schematic diagram of special vapor growth and diffusion-annealing ampoule (there are three indentations in outer quartz tube which are spaced 120° apart). (b) Section of furnace temperature profile (overall length of vertically positioned furnace is 60 cm).

5

			TABLE I-5			
		ANNEALING PARAMETERS AND OPERATING CHARACTERISTICS OF $Pb_{1-x}Sn_x$Te DIODE LASERS				
	Annealing Time	Annealing Temperature	Emission Wavelength (μ)		Minimum Threshold Current Density (A/cm^2)	
x	(days)	(°C)	12°K	77°K	12°K	77°K
0.15	None	None	11.7	9.5	250	3,000
0.17	2	450	13.0	9.9	55	10,000
0.19	3	450	14.5	11.0	130	9,000
0.20	3	450	15.1	11.2	275	12,500
0.21	2	450	16.8	12.0	175	7,000
0.22	7	450	17.2	—	175	>30,000
0.24	14	400	20.0	—	230	>30,000
0.25[†]	3	450	22.4	14.9	75	5,000
0.27	See text	See text	28.0	—	125	>30,000

† The quenched ingot used for the vapor growth source was doped with 4×10^{19} Bi atoms/cm^3.

points on the metal-saturated solidus lines in Ref. 4 corresponding to the growth temperature of about 825°C. N-type layers of thickness $\geqslant 25\,\mu$ were diffused by isothermally annealing the crystals in a horizontal furnace in the unopened growth ampoule and thus in the presence of the remaining source ingot. This method of preparing junctions utilizes the property[4] that, at least for values of x up to x = 0.27, metal-saturated crystals change from p- to n-type conductivity as the temperature is decreased. From isothermal metal-saturation experiments, type conversion temperatures of 580°, 525°, and 425°C are estimated for x = 0.17, 0.20, and 0.27, respectively. For x < 0.27, annealing parameters for junction formation are given in Table I-5. For x = 0.27, the annealing schedule for preparing junctions was 4 hours at 700°C, 6 days at 650°C, 7 days at 450°C, and 21 days at 400°C, giving an n-region approximately $30\,\mu$ deep. Annealing studies indicate the surface electron concentration of annealed undoped $Pb_{0.73}Sn_{0.27}$Te to be $\leqslant 10^{16} cm^{-3}$. From the annealing schedules followed in the present experiments, we expect that the hole concentration in the p-type substrate is less than the surface n-type carrier density for a distance beyond the n-p junction essentially equal to the junction depth. Hence, p-n junction phenomena in these diodes may occur in a region of relatively low carrier concentration.

After annealing, laser structures in the shape of rectangular parallelpipeds were obtained by cleaving perpendicular and parallel to natural (100) faces. To reduce planarity and reflectivity of the longer pair of sides perpendicular to the p-n junction plane, these were subjected to a chemical etch consisting of equal volumes of a saturated water solution of $Na_2S_2O_8$ and a 15 wt. percent water solution of NaOH (Ref. 5). This leaves the smaller end faces to define the Fabry-Perot cavity. Linear dimensions of the lasers were typically a few hundred microns.

Electrical contacts to the entire top and bottom surfaces were made with electroplated Au followed by electroplated In. The laser structures were mounted in low-inductance packages and leads were attached by room-temperature bonding methods.

It has been found consistently that a final fabrication step consisting of the removal by an electrolytic etch[6] of approximately 10μ of material from the four exposed laser sides reduces the threshold currents by at least 50 percent. This may be due to the removal of a damaged layer at the cleaved faces which exhibits a high rate of nonradiative recombination. Etching studies have shown that such damage exists to a depth of at least several microns.[7] This layer would decrease the effective quantum efficiency for recombination of injected carriers and, by locally reducing the density of injected carriers at a given current level, would produce a region of electromagnetic loss near each end face of the laser cavity. The width of the lossy region would equal approximately the width of the damaged layer plus a diffusion length for bulk minority carriers. Measurements of photoconductivity in $Pb_{1-x}Sn_xTe$ at $4.2°K$ indicate that some crystals of low carrier concentration have carrier diffusion lengths[8] greater than 100μ, so that even a narrow high recombination rate region could be quite important. The volt-ampere characteristics of the diode lasers exhibit a marked increase in zero-bias impedance after the electrolytic etch, which is evidence of the removal of a region with a high recombination rate. In diodes with areas of $2 \times 10^{-3} cm^2$, etching has resulted in an increase of zero-bias impedance to as high as 2×10^4 ohms for $x = 0.20$ at $12°K$, and 2×10^3 ohms for $x = 0.15$ at $77°K$, from typical pre-etch values of 5 ohms at both temperatures.

Several lasers were fabricated at each of a number of compositions, and were evaluated at $77°$ and $12°K$. The experimental arrangement for measuring spectra has been described elsewhere.[1] Emission wavelengths and minimum threshold current densities at each composition are listed in Table I-5. In every case, laser action was evidenced by a spectrum with a well-defined mode structure exhibiting the mode spacing expected for the Fabry-Perot cavity. The emission at 28μ by the $Pb_{0.73}Sn_{0.27}Te$ laser sets a new long wavelength limit for semiconductor lasers. No consistent variation of threshold current with the Pb:Sn ratio is apparent at either $12°$ or $77°K$. Power measurements were performed on a $Pb_{0.80}Sn_{0.20}Te$ laser using a calibrated thermopile positioned to intercept nearly all the radiation emitted from one laser end face. With pulse bias, a peak power output of $0.1W$ at $15A$, corresponding to an external quantum efficiency η_x of 0.08, was observed at $12°K$, and a peak power of $0.03W$ at $25A$, giving $\eta_x = 0.01$, was measured at $77°K$. With CW operation at $12°K$, $5 \times 10^{-3}W$ at $2A$, corresponding to $\eta_x = 0.03$, was observed.

The observation of laser action up to $x = 0.27$ indicates that the bandgap in the $Pb_{1-x}Sn_xTe$ alloy system is probably direct to at least this composition. The variation of the bandgap with composition as determined by the wavelength of the laser emission is consistent with the variation proposed previously.[9]

J. F. Butler
T. C. Harman

D. FAR-INFRARED PHOTOCONDUCTIVITY IN HIGH-PURITY EPITAXIAL GaAs

With the development of vapor and liquid phase epitaxial techniques, it has become possible to prepare high-purity layers of GaAs. The electrical behavior of this material at temperatures

between 300° and 4°K is dominated by shallow donor impurities with ionization energies of about 0.005 eV in the purest material.[10] We report here the observation of extrinsic photoconductivity involving these shallow impurity levels. The high responsivities and short response times observed indicate that high-purity GaAs has considerable potential as a sensitive and fast far-infrared detector.

The results reported here were obtained with vapor phase epitaxial GaAs which was grown on <111> oriented Cr-doped semi-insulating GaAs substrates using an $AsCl_3$-Ga-H_2 flow system.[11] The epitaxial layer was 40 μ thick, and the results of Hall effect measurements gave the net donor concentration, $N_D - N_A$, as $6.8 \times 10^{14} cm^{-3}$ and a Hall mobility at 77°K of 75,000 cm^2/V sec. The net carrier concentration at 4.2°K was $1.4 \times 10^{11} cm^{-3}$, and the corresponding mobility was 2500 cm^2/V sec. The behavior of the resistivity and Hall constant below about 8°K indicated effects of some impurity banding. Ohmic contacts were formed by alloying pure Sn with the GaAs at 300°C in a reducing atmosphere on two opposite edges of the 0.2 × 0.2 cm photoconductive samples. The 4.2° dark resistance of these samples was greater than 3 megohms.
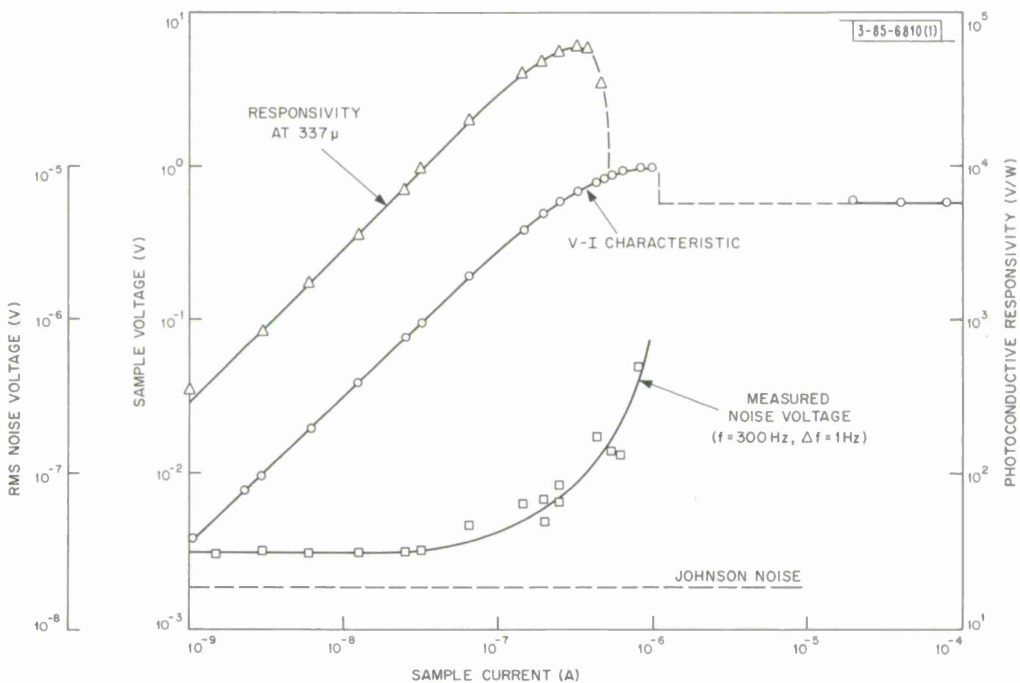
Fig. I-5. Voltage-current characteristic and variation of photoconductive responsivity at 337 μ and noise voltage (f = 300 Hz, Δf = 1 Hz) with sample current.

Figure I-5 shows the V-I characteristic of a photoconductive sample at 4.2°K. Similar behavior was observed in the other samples, and the characteristics are identical in the reverse direction, as expected for ohmic contacts. This behavior is ohmic for low currents and voltages, but as the electric field is increased above about 1 V/cm, the V-I characteristic becomes distinctly nonlinear, with the current increasing rapidly with increasing field. At a critical field strength of about 5 V/cm, the electric field decreases to a lower sustaining value which remains

constant with increasing current. Such behavior, as first observed in compensated Ge (see Ref. 12), is due to impact ionization of electrons from the compensated shallow impurity levels or from an impurity band; it has previously been reported in GaAs (Ref. 13).

The photoconductivity was examined at wavelengths of 195 and 337 μ using the emission from a DCN and HCN laser, respectively, and at 902 μ using the output of a carcinotron. The power level of the sources at 902 and 337 μ was 130 μW, and at 195 μ was 90 μW. The sample was mounted in a detector dewar similar to that used for submillimeter InSb detectors,[14] in which the sample was suspended at the open end of a silver-plated stainless-steel light pipe about 1 meter long and was immersed in liquid He. Two black polyethylene filters, one of which was cold, were mounted in the light pipe to exclude radiation shorter than about 40 μ. A copper cone and 90° bend were mounted at the top of the light pipe to collect the radiation from the source after it traversed a short air path. The photoconductive responsivity measured at 337 μ is shown in Fig. I-5 as a function of sample current. The signal increases linearly with current, as expected, until the field reaches the value where impact ionization begins to occur. The responsivities at the other two wavelengths show the same variation with current. The peak responsivities are 5×10^3 V/W at 195 μ, 4×10^4 V/W at 337 μ, and 9×10^2 V/W at 902 μ.

The sample noise was measured at 300 Hz (the chopping frequency used for the photoconductive measurements) with a low-noise, high-impedance preamplifier and a wave analyzer. The results of these measurements are also shown in Fig. I-5. For electric fields below 0.5 V/cm, the noise is dominated by the Johnson noise of the sample and the load resistor (at 4.2°K) in parallel plus a component due to the amplifier. However, at larger electric fields in the non-linear region of the V-I characteristic, the total noise increases rapidly and becomes dominated by G-R noise. These noise measurements can be combined with the responsivities to calculate an $NEP_\lambda = V_N/R_\lambda$, where V_N is the rms noise voltage, and R_λ is the responsivity at the wavelength λ. The peak values of NEP_λ are 1.2×10^{-11} W at 195 μ, 1.4×10^{-12} W at 337 μ, and 6×10^{-11} W at 902 μ.

The photoconductive time constant was determined to be shorter than 1 μsec by using the free carrier absorption induced by impact ionization in uncompensated Ge at 4.2°K to chop the incident radiation. A time constant of about 5 nsec for the lifetime of the carriers resulting from impact ionization of the shallow impurity levels in GaAs at low electric fields was measured using a method similar to that described by Koenig.[15]

There are three possible mechanisms which must be considered in the operation of a detector of this type. The first is the heating of the sample by the incident radiation, or the bolometric effect. However, since this effect is inherently slow, the high responsivities and short time constants observed indicate that this effect is not predominant. The second mechanism is the photoionization of the shallow impurity levels by the incident radiation. There should be a definite long-wavelength threshold for this effect corresponding to the ionization energy of the impurity state. For highest purity material, this should occur at about 250 μ corresponding to a donor level of ~0.005 eV, but for material with higher donor concentrations the threshold could occur at wavelengths longer than 400 μ corresponding to a donor ionization energy ≲0.003 eV (see Ref. 10). Although this threshold has not yet been located precisely, the fact that the photoconductive responsivity at 902 μ is much lower than that at 337 μ indicates that the threshold is

probably between these two wavelengths and that impurity level photoionization is likely to be the process responsible for the signal at the two shorter wavelengths. The last mechanism, which is probably responsible for the response at 902 μ, is the free carrier hot electron effect as observed in InSb (see Ref. 16). The coupling between the electrons and the crystal lattice is very weak at low temperatures in these materials so that, even at very low electric fields, the average energy of the photo-excited carriers can be appreciably greater than the thermal equilibrium value. Since the mobility is limited by ionized impurity scattering at low temperatures, the mobility of the hot electrons is increased and the sample resistance decreases. The response due to this mechanism should be most important at long wavelengths.

G. E. Stillman   C. D. Parker
C. M. Wolfe   P. E. Tannenwald
I. Melngailis   J. O. Dimmock

E. ISOLATION OF JUNCTION DEVICES IN GaAs USING PROTON RADIATION DAMAGE

We have found that proton radiation damage can be used to convert both p- and n-type GaAs into high-resistivity material, and have used this technique to isolate p-n junctions on a diffused GaAs substrate, to isolate islands of n-type material in an epitaxial layer deposited on semi-insulating GaAs, and also to prevent edge breakdown in Au-GaAs Schottky barriers.

The ion generator used in these experiments is a modified 400-keV Van de Graaff generator designed to accelerate positive ions. The protons are generated by RF excitation, accelerated to 400 keV, and magnetically analyzed. The samples are mounted on a tantalum sample holder, with part of each sample shielded from the ion beam with a molybdenum mask.

The p-n junction devices were formed on a slice of n-type GaAs with $n = 2 \times 10^{16}/cm^3$. Following the diffusion of a Zn-doped p-type layer into the top surface, an array of 0.003-inch gold circles on 0.005-inch centers was plated onto the sample using 0.15-μ pyrolytic SiO_2 as a plating mask. These gold contacts were sufficiently thick (3 μ) that the proton beam could not penetrate them. However, the 1500-Å SiO_2 layer between the contacts, which was left on the sample to reduce sputtering effects, was sufficiently thin so that it had only a slight effect on the proton beam. Consequently, only that part of the sample between the contacts was bombarded. Each sample was then irradiated at room temperature with a proton beam of current density 0.1 μA/cm^2, starting with an energy of 400 keV and subsequently decreasing the beam energy in steps of 20 keV, finishing at 60 keV. At each energy, the sample was exposed for 20 sec, to give a total dose of about 10^{14} protons/cm^2. Before irradiation, the current-voltage characteristics between the contacts were linear with a resistance of about 500 ohms. Following irradiation, these same contacts gave back-to-back diode characteristics, with a leakage current less than 0.1 μA and a breakdown voltage of about 40 V, typical of the substrate. Between a gold contact on the p-layer and an ohmic contact on the substrate, normal diode characteristics were observed.

The islands of n-type material were prepared on a sample which had a 3-μ thick epitaxial layer of n-type material (n ~ 10^{16}/cc) which was deposited on a chromium-doped semi-insulating substrate. The sample was plated with an array of gold-tin contacts which were alloyed. Additional gold was plated to provide a thickness of 3 μ. The sample was then irradiated at 400 keV for 20 sec. Before irradiation, the contact-contact resistance was about 60 ohms; subsequently,

the leakage currents were less than 0.1 μA at 100 V between these same contacts, indicating that the leakage resistance between the islands was in excess of 10^9 ohms.

The Schottky barrier diodes were prepared in a manner similar to the p-n junction devices, except that no p-type layer was diffused into the substrate, and irradiation was done only at 400 keV. Following irradiation, the original 3-μ thick gold contacts were removed and slightly larger semitransparent gold contacts were plated on the same areas. Current-voltage measurements on these devices showed that the reverse breakdown voltage following irradiation had increased substantially compared with the original diode, while the forward characteristic was unchanged. Visual observation of the light emitted from these diodes in reverse bias breakdown indicated that edge breakdown which was present in the original diodes had been suppressed, and that the higher voltage breakdown in the irradiated diodes occurred away from the edge.

We have also done some experiments in which the sample was bombarded before the gold contacts were applied, in order to determine the doping profile of the irradiated regions. These experiments were done by bombarding samples of n-type GaAs with proton beams of intensity 0.1 μA for 20 sec at various energy levels. After bombardment, each sample was plated with gold contacts, and capacity-voltage measurements were done in order to determine the doping profile. The initial results of these experiments are that the damaged region has high resistance (doping levels ~ 10^{13}/cc or less) from the surface of the crystal until the protons approach the end of their range. Near the end of the range, there is evidence of a change in the character of the radiation damage, with an indication that shallow donors are created in this region. The depth of the high-resistance region is about 4 μ at 400 keV.

This technique of creating high-resistivity material is simple and quite easy to use. We feel that it should be a useful tool for the fabrication of other structures in which thin high-resistivity layers are required.

A. G. Foyt   J. P. Donnelly
W. T. Lindley   C. M. Wolfe

F. SHORT WAVELENGTH RESPONSE CHARACTERISTICS OF InSb-MOS PHOTOVOLTAIC DETECTORS

We have continued to study the effects of short wavelength light on the characteristics of InSb-MOS detectors.[17] The photovoltaic response to modulated 3.9-μ radiation from an InAs diode emitter has been measured at 77°K. In our model of the MOS structure, this radiation acts as a probe of the InSb depletion region, and has no effect on the state of the structure. For n-type InSb, the depletion layer, in turn, gives an indication of the charge state of the oxide. The surface of the oxide is illuminated with short wavelength radiation from a monochromator, and the change in the response to the 3.9-μ radiation is measured. At 77°K, there is no response to the InAs radiation so long as the constant irradiation has a wavelength corresponding to photon energies < 1.3 eV or > 4.8 eV. In equilibrium for photon energies > 1.3 eV and < 4.8 eV, the response to the 3.9-μ radiation is relatively constant, independent of the intensity of the constant irradiation, but the time to reach the final value depends linearly on the intensity of the irradiating light, and very strongly on the photon energy.

At liquid nitrogen temperatures, once a response to the 3.9-μ radiation is created by short wavelength irradiation, the response remains for at least several hours, even if the irradiating light is cut off. In fact, the response remains even if the MOS structure is warmed to room

temperature and then cooled again. However, we find that if the sample is warmed to room temperature and then irradiated with short wavelength photons before it is cooled for the next measurement, the response to the 3.9-μ radiation is eliminated. The best wavelength for "killing" the response seems to occur at the peak of the oxide response shown in Fig. I-4 of Solid State Research Report (1968:1). These effects are undoubtedly due to trapping and detrapping of electronic charge at oxide states and/or at oxide-InSb interface states; however, the precise model for this trapping has not yet been determined.

W. E. Krag
R. J. Phelan, Jr.
J. O. Dimmock

REFERENCES

1. J. F. Butler, A. R. Calawa, and T. C. Harman, Appl. Phys. Letters <u>9</u>, 427 (1966), DDC 653367.

2. J. M. Besson, J. F. Butler, A. R. Calawa, W. Paul, and R. H. Rediker, Appl. Phys. Letters <u>7</u>, 206 (1965), DDC 628560; J. M. Besson, A. R. Calawa, and W. Paul, to be published in Phys. Rev.

3. J. F. Butler and T. C. Harman, IEEE Solid-State Device Research Conference, Santa Barbara, California, 19 – 21 June 1967.

4. A. R. Calawa, T. C. Harman, M. Finn, and P. Youtz, Trans. Met. Soc. AIME <u>242</u>, 374 (1968).

5. M. C. Finn, private communication.

6. M. K. Norr, J. Electrochem. Soc. <u>109</u>, 433 (1962).

7. J. F. Butler and T. C. Harman, Electrochemical Society Meeting, Boston, 5 – 9 May 1968.

8. I. Melngailis and T. C. Harman (to be published).

9. J. O. Dimmock, I. Melngailis, and A. J. Strauss, Phys. Rev. Letters <u>16</u>, 1193 (1966), DDC 642225.

10. J. Whitaker and D. E. Bolger, Solid State Commun. <u>4</u>, 181 (1966); D. E. Bolger, J. Franks, J. Gordon, and J. Whitaker, <u>Proceedings of the International Symposium on Gallium Arsenide, Reading, 1966</u> (Institute of Physics and the Physical Society, London, 1967), p. 16.

11. J. R. Knight, D. Effer, and P. R. Evans, Solid State Electron. <u>8</u>, 178 (1965); C. M. Wolfe, A. G. Foyt, and W. T. Lindley, Electrochem. Tech. <u>6</u>, 208 (1968).

12. A. L. McWhorter and R. H. Rediker, Proc. IRE <u>47</u>, 1207 (1959).

13. D. J. Oliver, Phys. Rev. <u>127</u>, 1045 (1962); R. A. Reynolds, Solid State Electron. <u>11</u>, 385 (1968).

14. E. H. Putley, Proc. IEEE <u>51</u>, 1412 (1963).

15. S. H. Koenig, R. D. Brown, III, and W. Schillinger, Phys. Rev. <u>128</u>, 1668 (1962).

16. B. V. Rollin, Proc. Phys. Soc. (London) <u>77</u>, 1102 (1961); E. H. Putley, <u>Physics of III-V Compounds</u>, Vol. 1, R. K. Willardson and A. C. Beer, editors (Academic Press, New York, 1966), p. 289.

17. Solid State Research Report, Lincoln Laboratory, M.I.T. (1968:1), p. 3, DDC 668762.

II. OPTICAL TECHNIQUES AND DEVICES

A. 100-WATT CO_2 AMPLIFIER

Further measurements have been taken of gain, beam size, and frequency pulling on the 9-meter 100-W CO_2 amplifier. Details of the device are given in the previous Solid State Research Report.[†]

Gain measurements were made with a sealed-off gas mixture of CO_2, N_2, He, and H_2 in the amplifier and, although not optimized, the gain was within 30 percent of that obtained with a flowing gas mixture. This probably indicates that under the appropriate conditions the amplifier gain would be the same for flowing or sealed-off gas mixtures. Detailed gain measurements for each tube show that the power gain was fairly well approximated by a solution to the gain equation assuming a constant gain with radial position and the power gain only a function of amplifier length L. The homogeneous saturation equation is

$$\frac{dP}{dz} = \alpha_o \frac{P}{1 + \frac{P}{W_o S}}$$

and, when solved under the restrictions above, yields (when integrated) the gain equation

$$\ln G + \frac{P_{in}}{P_s} (G - 1) = \alpha_o L$$

where

$G = P/P_{in}$, the gain at L within the amplifier,

P_{in} = the input power,

P_s = saturation power = $W_o S$, the beam cross section is S, and

$\alpha_o = cm^{-1}$, the small signal gain parameter.

Figure II-1 shows the theoretical gain curves as a function of the ratio of tube input power to saturation power of the amplifier. The parameters of these curves were determined from the experimental data and, over the region shown, represent the data fairly well. The power output measured for 2- and 10-W input was 56 and 88 W in the sealed-off condition, which would be 73 and 114 W for a flowing gas mixture. The small signal gain for the 20-mm bore tube is 9.3, the 25-mm bore tube is 8, and the 30-mm bore tube is 4.2.

The beam profile as shown in Fig. II-2 is taken at the output of the 9-meter amplifier. The solid curve is Gaussian and closely approximates the measured laser beam radial distribution of the TEM_{00} mode at the amplifier output when the amplifier is in the off condition; but, with amplification, this approximation becomes inaccurate with increasing beam radius, presumably because saturation effects are less at the larger radii, resulting in a larger gain and higher relative power at larger distances from the tube center.

[†] Solid State Research Report, Lincoln Laboratory, M.I.T. (1968:1), p. 11, DDC 668762.
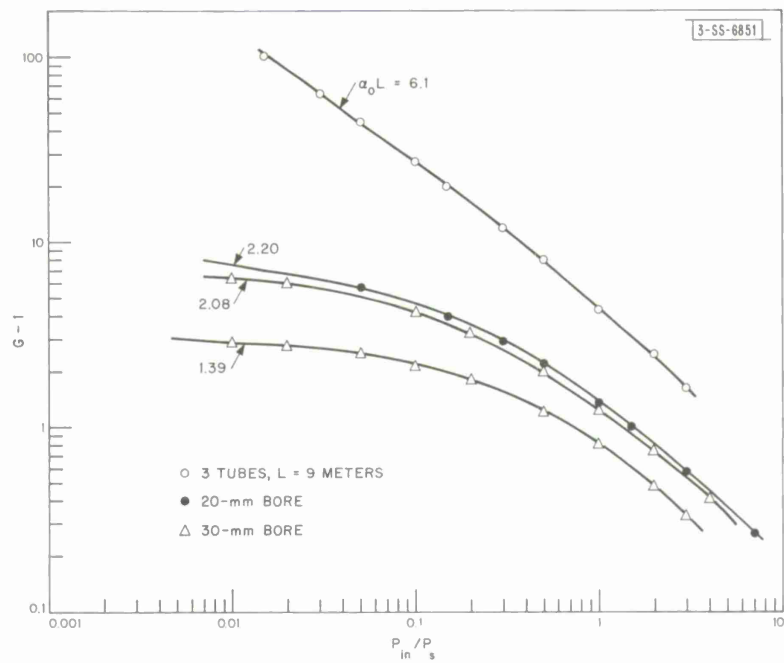
Fig. II-1. CO_2 amplifier tube gain as function of ratio of input power to saturation power.
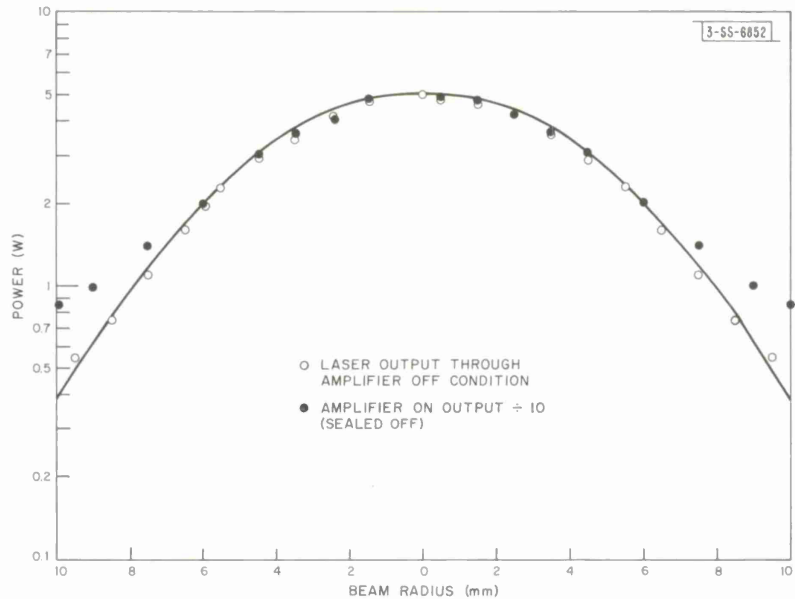

Fig. II-2. Beam profile of laser and amplifier output compared with Gaussian beam shape.

The output of the laser has been monitored with a monochromator which will resolve a frequency difference of 10 GHz at 10 μm. The laser output within this resolution limitation is not shifted with the amplifier on or off, and independent of a static or flowing gas fill condition existing in the amplifier tubes.

R. J. Carbone

B. STABLE LASER OSCILLATOR, DESIGN AND TESTING

The extensive testing of the $1\frac{1}{2}$-meter cavity stable oscillator has been completed. Since its completion over a month ago, this laser was successfully utilized as a single-frequency driver for the 100-W amplifier described in Sec. II-A above.

Two potential problems arose during tests of this 10- to 15-W oscillator. At first, in spite of the 100-MHz cavity mode spacing, this laser would only oscillate in the 00°1 to 02°0 vibrational band of CO_2 during several weeks of continuous testing. Although systematic variations of pressure and excitation current have been tried over more than a 2:1 range, the output would at most shift to some other strong P- or R-branch rotational transition within the 00°1 to 02°0 vibrational band. Subsequently, this behavior was attributed to slightly higher reflectivities in the 9- to 10-μm wavelength region on several output mirrors used in these tests. After changing to mirrors with reflectivities carefully maximized at 10.6 μm, 00°1 to 10°0 vibrational band operation was immediately obtained.

The second potentially very troublesome problem was located when it was noticed that the output mirror holder's temperature increased appreciably with some of the mirrors tried during the testing of the $1\frac{1}{2}$-meter oscillator. Subsequently, it was determined that most of the IRTRAN IV substrates tested had an absorption appreciably greater than that specified by the manufacturer. Because of the unexpected absorption losses in the output mirror and the high output power of the $1\frac{1}{2}$-meter oscillator, the output may shift several rotational transitions before reaching a final equilibrium temperature. Although this settling time is very much longer than found with previous lower power tubes, essentially single-transition, single-frequency operation will ultimately occur.

The absorption problem found with IRTRAN IV will be hopefully overcome by the future use of GaAs substrates. All three GaAs substrates tested so far yielded consistent data which were well below the absorption losses of the best IRTRAN IV tested.

Extensive modifications of the laser processing station were carried out. The resulting versatility in the choice of gas fill enabled us to double to 3 W the single-frequency output power of the older 50-cm cavity (20-cm discharge length) stable lasers. Assembly of the completely redesigned versions of the stable lasers was begun, and testing should commence within a month.

C. Freed

C. THERMAL BLOOMING

From elementary considerations, one would expect lens-like effects when a light beam deposits heat in a fluid. Assuming the refractive index change is proportional to the density change, analytic expressions for the steady-state focal length[1] (negative) and the time development[2] of the focal length of an absorbing medium can be obtained using a simplified model. The validity of this model has been experimentally confirmed in liquid cells.[3]

A cell has been constructed to attempt the measurement of these thermal blooming effects in gases. Because of the relatively high power available, a CO_2 gas laser has been used as the source and pure CO_2 gas at about one atmosphere as the absorber. When necessary, the absorption can be enhanced by the addition of a few torrs of ethylene. Although the blooming in a 2-meter cell with 5-W input in a 1-cm beam is quite substantial ($f \approx -2m$), all attempts at quantitative measurements of the time development have been unsuccessful. The dynamic range and sensitivity of the temperature-sensitive phosphor[4] are inadequate with the laser power now available to us (the beam is visible with appropriate mounting of the phosphor, but the time response under these conditions is poor). An attempt was made to measure the output beam diameter by scanning it across a photoconductive detector, but the lack of cylindrical symmetry due to convection and the shape changes as steady state is approached make interpretation of the results difficult. The cell is now mounted horizontally, and the characteristic time for convection effects is comparable to that for thermal diffusion, causing the above problems.

Several possible changes are under consideration, such as using a wavelength where better image detectors are available, using higher power at $10.6\,\mu$, or using the 10.6 beam only for heat deposition and using a low-power visible beam for measurements.

A. H. M. Ross

D. OPTICAL HETERODYNE DETECTION AT 10.6 μm OF THE BEAT FREQUENCY BETWEEN A TUNABLE $Pb_{0.88}Sn_{0.12}Te$ DIODE LASER AND A CO_2 GAS LASER

We have used a current-tunable $Pb_{0.88}Sn_{0.12}Te$ diode laser to achieve optical heterodyning with a CO_2 gas laser. The beat frequency was continuously controllable from under 50 to 1300 MHz, the high-frequency limit of our Ge:Cu detector. These experiments have yielded the first direct measurement of the linewidth of the emission from a semiconductor p-n junction laser, displayed on a spectrum analyzer as a frequency spread of the heterodyne signal. Preliminary indications are that the linewidth is less than 100 kHz, with power supply ripple in the diode laser circuit presently precluding a more accurate determination. (The linewidth of the CO_2 laser emission is less than a few hundred hertz.[5])

The diode used for the heterodyne experiments was cleaved into a rectangular parallelepiped 1.3 mm long, 0.5 mm wide, and 0.2 mm thick from vapor-grown $Pb_{1-x}Sn_xTe$ material tailored to produce spontaneous emission at $10.6\,\mu$m, for which $x = 0.12$. Ohmic contacts were applied and the diode was attached to the cold "finger" of a liquid helium dewar. A single-pass grating spectrometer was used to measure the wavelength of the laser emission as a function of diode current; curves similar to those of magnetic-field tuning[6] were obtained.

The diode laser line is tunable through six modes from 943.6 to 946.7 cm^{-1} for direct currents from 675 to 1800 mA. (At 1000 mA, the output power is approximately 100 μW.) Within each mode, continuous control is achieved over approximately 0.2 cm^{-1} (6 GHz). The overall tuning range encompasses two adjacent CO_2 rotational transitions: P_{18} at 945.93 cm^{-1}, and P_{20} at 944.15 cm^{-1}. Only the P_{20} transition is close enough to one of the diode laser modes to produce a beat frequency within the limits of our detector. The CO_2 laser, which was especially constructed for highly stable, single-frequency operation,[5] was tuned to the P_{20} transition; the

16

$Pb_{0.88}Sn_{0.12}Te$ diode current was adjusted to produce laser emission in the proper mode. Both beams were directed collinearly onto the Ge:Cu detector, and under these conditions the heterodyne IF detector current is given by

$$i_{IF} = (2qG\eta /h\nu) (P_1 P_2)^{1/2} \sin[2\pi f_{IF}t] \tag{1}$$

where the beat frequency $f_{IF} = c(944.15 - \lambda_{diode}^{-1})$, P_1 and P_2 are the absorbed powers, G is the detector gain, and η is its efficiency. Polarization and nonalignment terms are neglected.

Figure II-3(a) is an oscillograph of the 100-MHz beat signal produced between the P_{20} laser line and the diode laser line emitted at 1135 mA. The sinusoidal variation, in accordance with Eq. (1), is a clear indication of heterodyne operation. The dispersion of a 1250-MHz beat frequency (diode current of 1045 mA), occurring just below the detector cutoff frequency, is shown in Fig. II-3(b). It is evident from the width of the spectrum that the diode laser linewidth is 100 kHz or less. The 1-sec exposure of Fig. II-3(c) represents 100 sweeps of the spectrum analyzer and illustrates the fluctuations in the beat frequency caused by the 100-μA rms ripple in the diode laser current. With a better power supply in conjunction with storage batteries, we hope to reduce the ripple in the diode current.

Figure II-4 shows the range over which the beat frequency was continuously tunable, and the dependence of the beat frequency on diode current. The tuning rate of 12.8 MHz/mA agrees well with that predicted from the grating spectrometer data.

E. D. Hinkley
T. C. Harman
C. Freed

REFERENCES

1. J. P. Gordon, R. C. Leite, R. S. Moore, S. P. S. Porto, and J. R. Whinnery, J. Appl. Phys. 36, 3 (1965).

2. N. M. Kroll and P. L. Kelley, private communication.

3. R. L. Carman and P. L. Kelley, Appl. Phys. Letters 12, 241 (1968).

4. T. J. Bridges and E. G. Burkhardt, IEEE J. Quant. Electron. QE-3, 168 (1967).

5. C. Freed, IEEE J. Quant. Electron. (to be published).

6. J. F. Butler and A. R. Calawa, Physics of Quantum Electronics (McGraw-Hill, New York, 1966), p. 458.
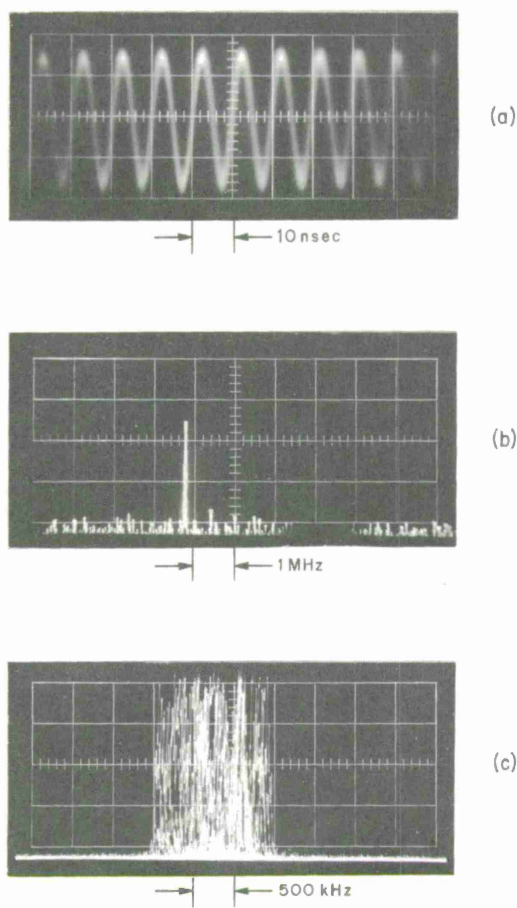
Fig. II-3. Beat frequency signal between $Pb_{0.88}Sn_{0.12}Te$ diode laser line and P_{20} line of CO_2 laser. (a) f_{IF} = 100 MHz, I_d = 1135 mA; (b) f_{IF} = 1250 MHz, I_d = 1045 mA, single scan; (c) multiple (100) scan, illustrating effect of power supply ripple of 100-μA rms in diode circuit.
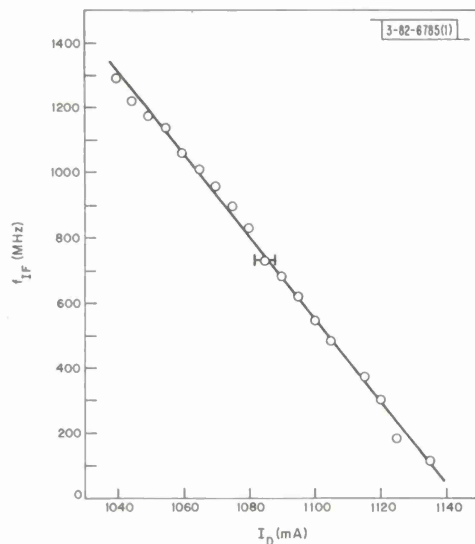
Fig. II-4. Tuning range of beat frequency and dependence on diode current. Frequency values were measured with spectrum analyzer.

18

III. MATERIALS RESEARCH

A. BOUNDARY LAYER ANALYSIS OF FORCED CONVECTION CRYSTAL GROWTH

We have found that forced convection can be used to increase the rate of crystal growth from the vapor phase and to control the morphology of the growing interface.[1-3] The relationship between growth rate and carrier gas velocity has now been derived theoretically by analyzing the properties of the diffusion boundary layer at the interface. In addition, the condition required for interface stability has been formulated in terms of the temperatures at the interface, at the edge of the boundary layer, and at the solid source.
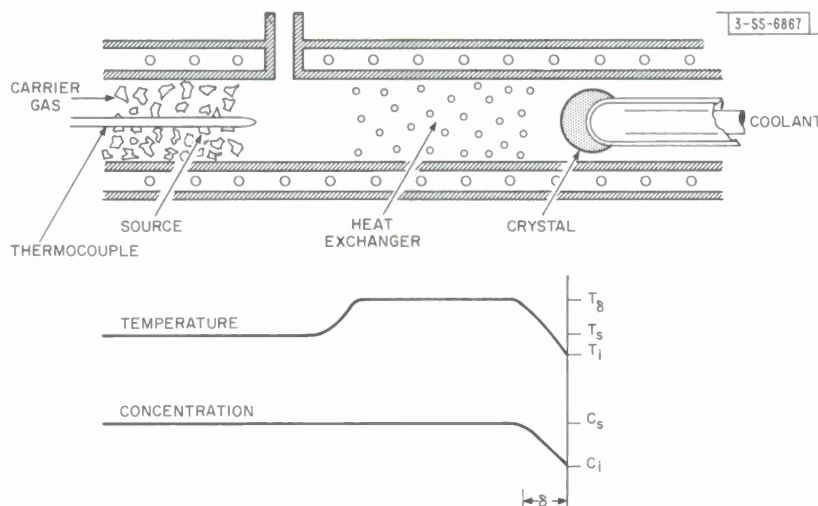
Fig. III-1. Schematic drawing of apparatus for measuring crystal growth velocity as function of carrier gas velocity and temperatures T_i, T_δ, and T_s.

The apparatus used to study forced convection crystal growth is shown in Fig. III-1. An inert carrier gas, passing through a packed bed of polycrystalline material, is saturated with vapor at the source temperature T_s. The concentration C_s of the vapor is related to the saturation vapor pressure p_s by the ideal gas law $C = p/RT$. The saturated gas is then heated to a higher temperature T_δ. Finally, it passes over the growing crystal interface at a lower temperature T_i, where condensation reduces the vapor pressure to p_i (the saturation pressure at T_i), and correspondingly reduces the concentration to C_i. If it is assumed that the temperature and concentration changes occur in a boundary layer of thickness δ adjacent to the interface, forced convection may be regarded as placing a virtual vapor source (at temperature T_s) and a virtual heat source (at temperature T_δ) at a distance δ from the interface.

If diffusion through the boundary layer is the rate-limiting step in crystal growth, the growth rate given by the material balance at the interface is

$$v = \frac{MD(C_s - C_i)}{\rho \delta} \tag{1}$$

where M is the molecular weight of the condensing vapor, D is its diffusion coefficient in the carrier gas, and ρ is the density of the crystal. For forced convection, the thickness of the boundary layer is

$$\delta = B(D/V)^{1/2} \tag{2}$$

where V is the carrier gas velocity, and B is a geometric constant. Substituting Eq. (2) into Eq. (1) gives

$$v = \frac{M(C_s - C_i)\,(DV)^{1/2}}{\rho B} \quad . \tag{3}$$

Thus, the crystal growth velocity is proportional to the first power of the available vapor concentration $(C_s - C_i)$, and to the square root of the carrier gas velocity.
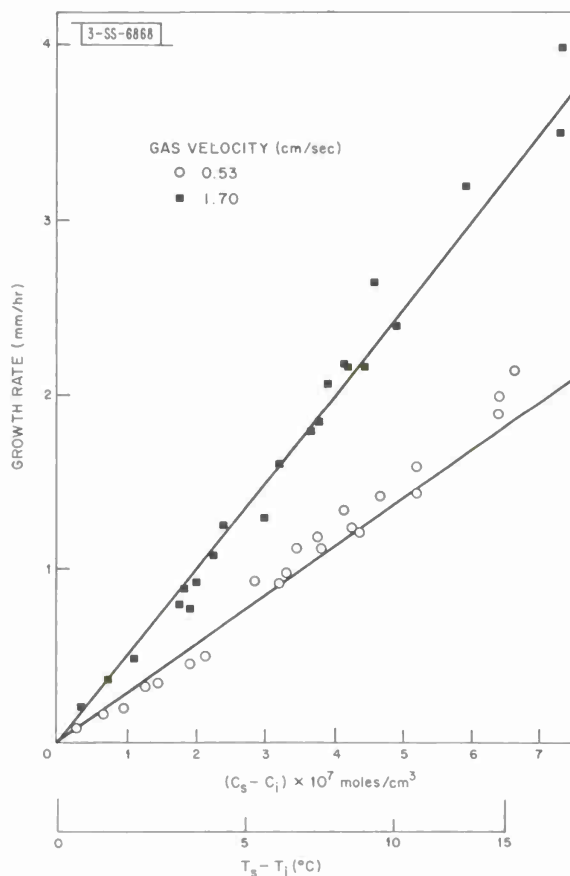
Fig. III-2. Growth velocity of iodine crystals as function of available concentration $(C_s - C_i)$, for two different helium carrier gas velocities. Source temperature $T_s = 90°C$.

Data previously reported[1] for the growth velocity of iodine crystals as a function of the temperature gradient at the interface can be used to test Eq. (3). These data, which were obtained with the apparatus of Fig. III-1 for two different helium carrier gas velocities, have been replotted in Fig. III-2 as a function of the available vapor concentration. In agreement with Eq. (3), it is seen that v is proportional to $(C_s - C_i)$ for a given value of V. The straight lines shown in Fig. III-2 were calculated from Eq. (3) by using the measured values of $(C_s - C_i)$ and V, the published values of M and ρ, and $D = 0.5\,\text{cm}^2/\text{sec}$, the self-diffusion coefficient for helium gas at one atmosphere. The only adjustable parameter was the constant B. The same value of this constant, $0.71\,\text{cm}^{1/2}$, was used to calculate the lines for both values of V. The satisfactory agreement between the lines and the experimental points shows that the data are consistent with the $v \propto V^{1/2}$ relationship of Eq. (3).

The experimental results previously reported[2] for the growth rate of camphor crystals also confirm the proportionality between v and $(C_s - C_i)$. The best fit to the data was obtained for $B = 0.57\,\text{cm}^{1/2}$.

Throughout the preceding discussion, it was assumed that crystal growth takes place at a smooth interface. However, we showed earlier[1-3] that roughening of the interface or even dendrite formation can occur in vapor growth because of interface instability resulting from

constitutional supercooling. We derived[3] a criterion for interface stability in terms of the temperature gradient in the gas phase at the interface and the growth velocity, considered as two independent variables. We shall now extend the earlier treatment by taking account of the relationship between these quantities.

It was shown in Ref. 3 that the growth interface will be stable if $(dp/dx)_i \leqslant (dp_o/dx)_i$, where p is the partial pressure of the condensing component, p_o is the saturated vapor pressure, and x is the distance between the interface and a point in the gas phase. The stability criterion may also be written as $(dC/dx)_i \leqslant (dC_o/dx)_i$, where C_o is the concentration corresponding to p_o.

If the concentration gradient within the boundary layer is assumed to be constant, then for forced convection,

$$(dC/dx)_i = \frac{C_s - C_i}{\delta} \qquad . \tag{4}$$

If it is assumed that p_o is proportional to $\exp\left[-\Delta H/RT\right]$ and that p_i is equal to p_o at T_i, then differentiating $C_o = p_o/RT$ gives

$$(dC_o/dT)_i = \frac{C_i}{T_i}\left(\frac{\Delta H}{RT_i} - 1\right) \qquad . \tag{5}$$

If it is assumed that the temperature gradient is constant within the thermal boundary layer, and that this layer has the same thickness as the diffusion boundary layer, then

$$(dT/dx)_i = \frac{T_\delta - T_i}{\delta} \qquad . \tag{6}$$

Multiplying Eqs. (5) and (6) gives

$$(dC_o/dx)_i = \frac{T_\delta - T_i}{\delta}\frac{C_i}{T_i}\left(\frac{\Delta H}{RT_i} - 1\right) \qquad . \tag{7}$$

To obtain the criterion for interface stability, we set $(dC_o/dx)_i$ equal to $(dC/dx)_i$. From Eqs. (4) and (7),

$$\frac{T_\delta - T_i}{T_i} = \frac{(C_s - C_i)/C_i}{(\Delta H/RT_i) - 1} \tag{8}$$

$$\frac{T_\delta}{T_i} = \frac{(T_i/T_s)\exp\left[(\Delta H/RT_i)\,(T_s/T_i - 1)\right] - 1}{(\Delta H/RT_i) - 1} + 1 \tag{9}$$

The growth interface will be stable only for values of T_δ/T_i equal to or greater than those given by Eq. (9). Values of T_δ/T_i calculated from Eq. (9) are plotted in Fig. III-3 as a function of T_s/T_i for the case in which $\Delta H/RT_i = 15$, the value for a gas obeying Trouton's rule when $p_i = 15$ torrs. We see from Fig. III-3 that along the calculated line the value of T_δ/T_i is always greater than the corresponding value of T_s/T_i. Therefore, stable growth can occur only if the carrier gas, after passing over the source at T_s, is heated to a temperature higher than T_s before it reaches the growth interface. It should be noted that the growth velocity does not appear
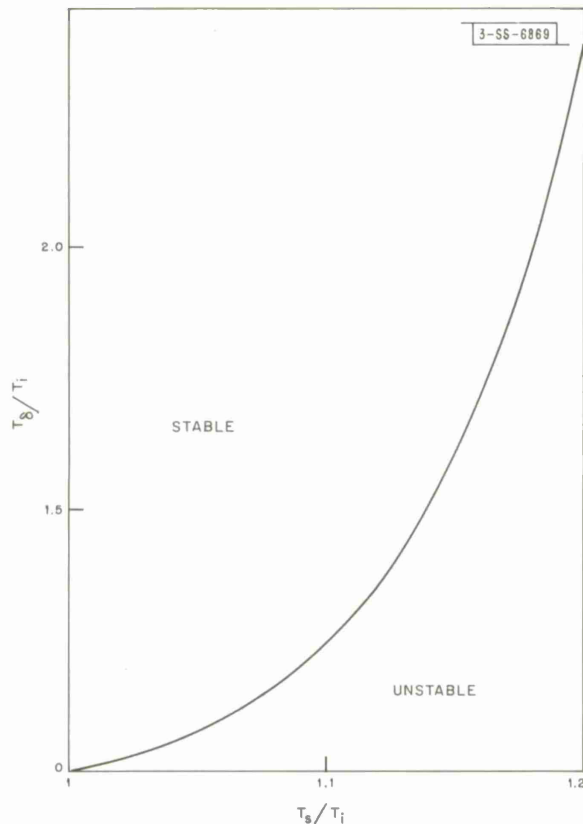
Fig. III-3. Dependence of T_δ/T_i on T_s/T_i, according to Eq. (9), for $\Delta H/RT_i = 15$.

in Eq. (9). Therefore, once a suitable temperature profile is established, the growth velocity may be increased indefinitely, without causing interface instability, by increasing the carrier gas velocity.

T. B. Reed
A. J. Strauss

B.   OPTICAL TRANSMISSION OF $Cd_{1-x}Mg_xTe$ ALLOYS

The first investigation of the pseudo-binary CdTe-MgTe system was recently reported by Itoh.[4] Since CdTe has the zincblende structure and MgTe has the wurtzite structure, a complete series of solid solutions cannot be formed. However, Itoh found that there is extensive mutual solid solubility. Alloys with zincblende structure are formed for compositions up to about 60 mole-percent MgTe, and wurtzite-structure alloys are stable for compositions above about 75 mole-percent MgTe. Itoh found that the energy gap of the zincblende-structure alloys increases monotonically with increasing MgTe content.[4]

In the present study, optical transmission measurements have been made on alloy crystals containing up to 46 mole-percent MgTe. The alloys were prepared from the elements in an open-tube reactor,[5] where synthesis can be carried out quite rapidly without the danger of explosion encountered when sizable quantities of the elements are reacted in a sealed quartz ampoule. To obtain single crystals, ingots of the alloys were prepared by the Bridgman method. The fine-grained material prepared in the reactor was placed in a 24-mm i.d. fused silica ampoule, tapered

to a point at the lower end, which had been coated with pyrolytic graphite. After the ampoule was evacuated and sealed, it was heated in a vertical resistance furnace to melt the alloy, and then lowered through the furnace to produce directional crystallization of the melt. Thermal analysis experiments on CdTe-rich melts have shown that the liquidus temperature initially increases linearly with increasing MgTe content. For 35 mole-percent MgTe, the liquidus temperature is 1150°C. The value of 1114°C reported by Itoh[4] for this composition is much too low.

Single-crystal samples between 1 and 3 mm thick were cut from the Bridgman-grown ingots with a wire saw and then mechanically polished. After the initial transmission measurements, a number of samples were annealed several days in saturated Cd vapor at 900°C and then remeasured.
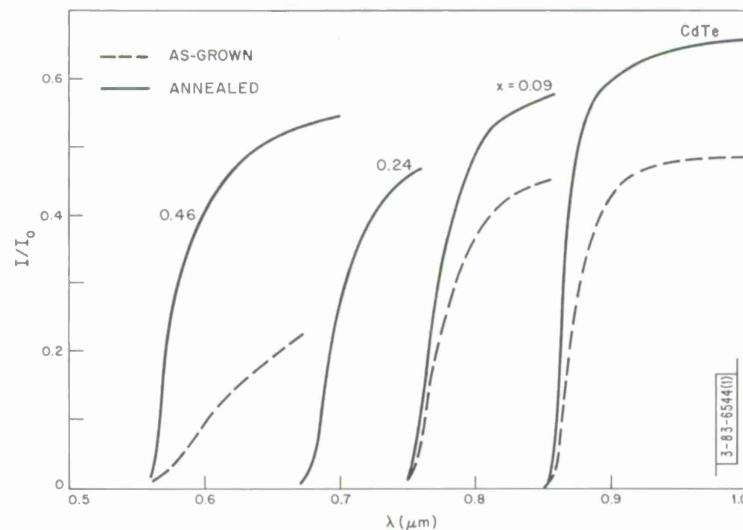
Fig. III-4. Optical transmission at room temperature vs wavelength for $Cd_{1-x}Mg_xTe$ alloys.

Optical transmission measurements in the vicinity of the fundamental absorption edge were made at room temperature with a single-beam, prism spectrometer. Figure III-4 shows the transmission curves obtained for CdTe and three representative alloy samples. These results illustrate the monotonic decrease in the absorption edge wavelength with increasing MgTe content, from about 0.86 μm in the infrared for CdTe to about 0.56 μm in the visible for x = 0.46. They also illustrate the marked increase in transmission at wavelengths beyond the absorption edge which generally resulted from annealing in saturated Cd vapor. (The as-grown data for the sample with x = 0.24 have been omitted from Fig. III-4, since annealing produced no appreciable change in its transmission.) It is probable that the increase in transmission is due primarily to the removal of Te-rich inclusions or microprecipitates formed during growth. This explanation is consistent with microscopic observations made on alloy samples which contained enough MgTe to be transparent to visible light. The as-grown samples contained large numbers of small opaque areas which were greatly reduced in size by annealing.

Transmission measurements between 2 and 15 μm were made on annealed samples at room temperature with a double-beam, prism spectrometer. For each sample, the transmission is
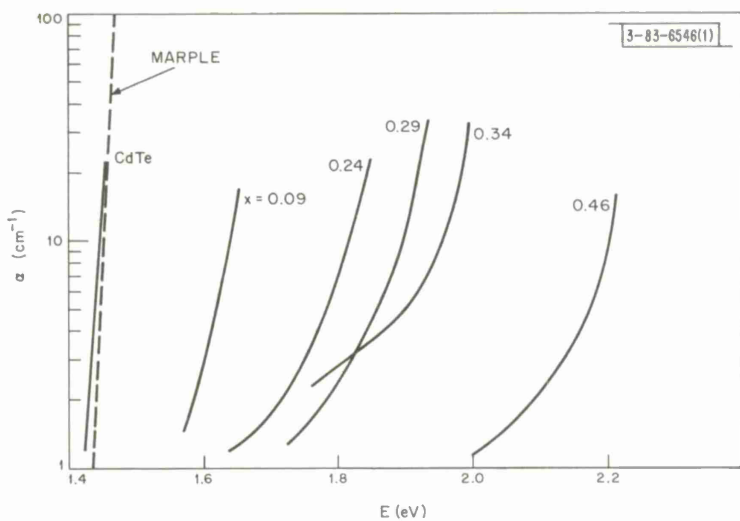
Fig. III-5. Absorption coefficient at room temperature vs photon energy for $Cd_{1-x}Mg_xTe$ alloys.
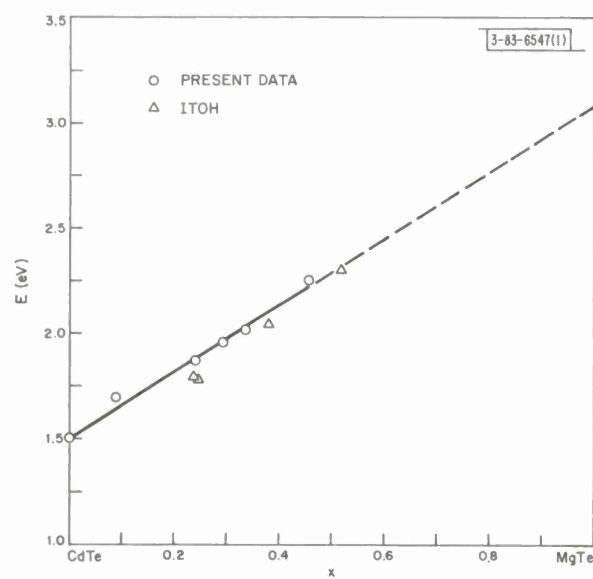
Fig. III-6. Energy gap at room temperature vs composition for $Cd_{1-x}Mg_xTe$ alloys.

almost independent of wavelength and lies between 50 and 65 percent. These results indicate that the transmission in this region was determined primarily by reflection losses.

In order to determine the energy gaps of the alloys, absorption coefficients were calculated from the transmission data in the vicinity of the absorption edge. The reflectivity for all samples was taken to be 0.24, the value for CdTe at its absorption edge. The results are shown in Fig. III-5, where the absorption coefficient is plotted on a logarithmic scale as a function of photon energy. The results for CdTe are in reasonably good agreement with those reported by Marple.[6] The absorption edge is not as steep as Marple's, presumably because of the higher purity and surface perfection of Marple's sample which was zone-refined and chemically polished. The absorption edges for the alloy samples are considerably less steep than the edge for CdTe. This difference could easily be due to the lower purity of the alloys. Although they were synthesized from the best commercially available Mg, this material is much less pure than the Cd and Te used.

An arbitrary but consistent method was used to evaluate the energy gaps of the alloys. The energy gap for each sample was obtained by adding 0.056 eV to the photon energy for which the absorption coefficient of the sample was $10\,\mathrm{cm}^{-1}$. The correction term of 0.056 eV was adopted in order to yield the published value, 1.50 eV, for the energy gap of CdTe at room temperature. The energy gap values obtained in this manner are plotted against mole-fraction MgTe in Fig. III-6. The data are well represented by a straight line. Extrapolation to $x = 1$ gives 3.08 eV as the energy gap of hypothetical cubic MgTe. As shown in Fig. III-6, energy gap values calculated from the absorption edge wavelengths reported by Itoh[4] are in fairly good agreement with the present values. However, the present values are not consistent with Itoh's conclusion that the absorption edge wavelength, rather than the energy gap, varies linearly with MgTe content. Extrapolation of his wavelength vs composition line gives 5.0 eV for the energy gap of cubic MgTe. This value seems much too high, since published[7] optical absorption data for thin films of hexagonal MgTe indicate that the energy gap of this phase is less than 3.6 eV. At this energy, the absorption coefficient has already risen to about $10^5\,\mathrm{cm}^{-1}$, and there is a peak in the curve of absorption coefficient vs energy.

<div align="right">A. J. Strauss</div>

C. PHOTOLUMINESCENCE DUE TO OXYGEN IN ZnTe ALLOYS

Thomas and co-workers[8] were the first to observe mirror luminescence and absorption bands in ZnTe due to a center lying about 0.4 eV below the conduction band. They proposed[9] that this center is an isoelectronic trap resulting from the substitution of an oxygen atom on a tellurium site. At low temperatures, the luminescence band peaks close to $6500\,\mathring{A}$, and the absorption band peaks near $5900\,\mathring{A}$. Both bands exhibit marked structure due to phonon cooperation.

According to the proposed model, the oxygen acts as an acceptor-like electron trap, since oxygen is more electronegative than the tellurium it replaces. In the no-phonon process, the absorption of a photon of energy E_o results in the formation of a bound exciton, which is composed of an electron strongly bound to the oxygen center and a hole weakly bound to the electron. Luminescence is observed when the exciton is annihilated. In the no-phonon case, the energy of the emitted photon is again E_o. The electron trapping energy E_t is equal to the band gap energy E_g minus E_o. For ZnTe at 4.2°K, where we have performed our luminescence experiments, E_g is 2.39 eV, E_o is 1.986 eV, and E_t is therefore 0.40 eV.
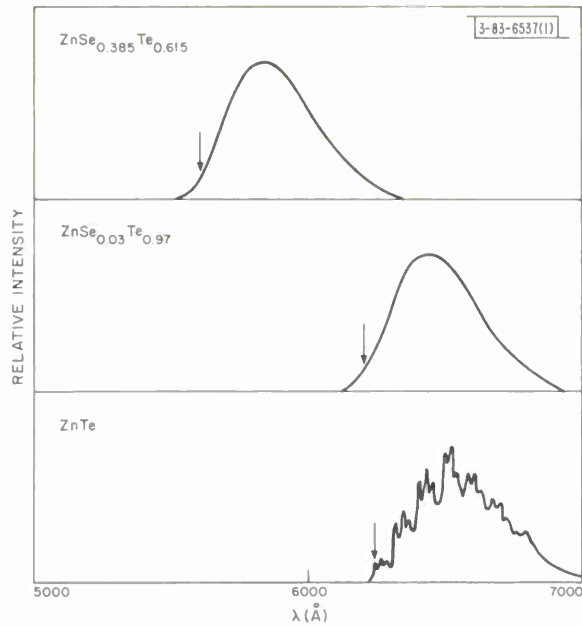
Fig. III-7. Spectra of photoluminescence at 4.2°K due to oxygen in $ZnTe_{1-x}Se_x$ alloys. Wavelengths corresponding to no-phonon energy E_o are indicated by arrows.

Fig. III-8. Photoluminescence energies and energy gap for $ZnTe_{1-x}Se_x$ alloys at 4.2°K, plotted against mole-fraction ZnSe.
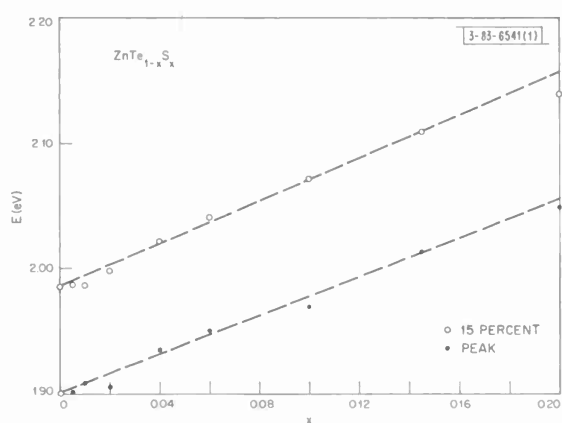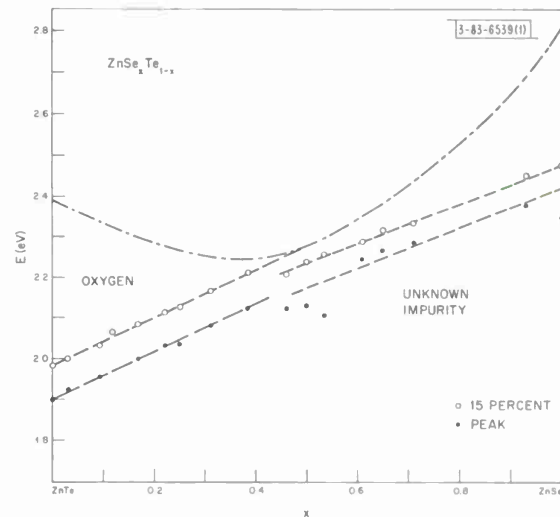

Fig. III-9. Photoluminescence energies for $ZnTe_{1-x}S_x$ alloys at 4.2°K, plotted against mole-fraction ZnS.

At the beginning of our investigation, oxygen had not been conclusively identified as the center responsible for the mirror luminescence and absorption, although Hopfield, Thomas, and Lynch[9] had reported observing the most intense absorption in samples grown from a melt doped with ZnO. Similarly, we have found that the absorption coefficient in vapor-grown crystals increases with increasing partial pressure of oxygen in the growth ampoule. Merz[10] has recently presented much more direct evidence for the oxygen model based on isotope substitution and Zeeman experiments.

In this investigation, we have observed the variation in the oxygen luminescence spectrum which results when ZnTe is alloyed with ZnSe, ZnS, or CdTe. On the basis of the oxygen model, the trapping energy E_t is expected to decrease with increasing ZnSe or ZnS content, since oxygen and tellurium differ more in electronegativity than do oxygen and selenium or oxygen and sulfur. On the other hand, E_t is expected to remain essentially constant in the ZnTe-CdTe alloys, since changes in the cation lattice should not strongly affect the trapping process. These predictions have been confirmed by the data.

Alloy samples were prepared by annealing weighed mixtures of the powdered compounds in sealed quartz ampoules. In order to enhance the luminescence, excess zinc metal was added to the powder mixtures, and the ampoules were backfilled with oxygen at 400 torrs. The samples were annealed at 1050°C or above for 3 days and then either furnace-cooled or quenched in water. The alloy compositions were determined from x-ray lattice parameters and did not vary from the nominal compositions by more than 2 mole-percent.

Figure III-7 shows representative photoluminescence spectra for ZnTe-ZnSe alloys at 4.2°K excited by 3650 Å radiation. The luminescence band is shifted to higher energies with increasing ZnSe content. Addition of as little as 3 mole-percent ZnSe causes the phonon structure to disappear. This makes it impossible to determine E_o for the alloys from the position of a distinguishable no-phonon line. On the basis of the data for ZnTe, E_o for each alloy has been taken as the energy corresponding to the wavelength on the high-energy side of the luminescence band at which the intensity is 15 percent of the maximum intensity for the band.

In Fig. III-8, the 4.2°K values of E_o and of the photon energy at the peak of the luminescence band are plotted against x, the mole-fraction of ZnSe in the $ZnTe_{1-x}Se_x$ alloys. Up to x = 0.4, both energies increase as x increases, and the data are well represented by two parallel straight lines. This indicates that the shape of the band remains essentially the same over this composition range. Near x = 0.4, however, there appears to be an abrupt change in the character of the luminescence, and we believe that the luminescence above x = 0.4 is not due to oxygen but rather to some unknown impurity.

Figure III-8 also gives the values of the energy gap E_g for the $ZnTe_{1-x}Se_x$ alloys at 4.2°K. The E_g curve, which passes through a minimum at x = 0.4, was obtained by scaling the room-temperature values determined by Larach, Shrader, and Stocker.[11] It is seen that the trapping energy E_t, which is the difference between E_g and E_o, decreases with increasing ZnSe content, as expected for the isoelectronic trap model. Extrapolation of the E_o line indicates that the trapping energy becomes zero at about x = 0.5. Consequently, there is no luminescence due to oxygen at higher concentrations of ZnSe. For these concentrations, the luminescence observed is due to the unknown impurity mentioned above.

Figure III-9 shows the oxygen luminescence data for ZnTe-ZnS alloys containing up to 20 mole-percent ZnS. The photon energies at the peak of the luminescence band and at 15-percent

intensity increase with increasing ZnS content. The data are well represented by two parallel straight lines, whose slope is somewhat greater than the slope of the corresponding lines in the ZnTe-ZnSe system. Although energy gap data for the ZnTe-ZnS system are very limited, Larach, Shrader, and Stocker[11] have found that E_g initially decreases with increasing ZnS content. Therefore, E_t decreases with increasing ZnS content, as expected for the isoelectronic trap model.
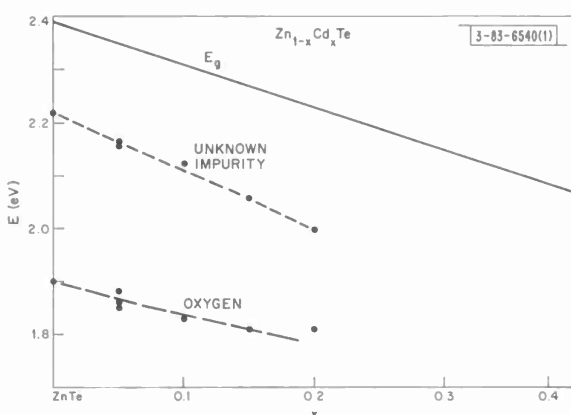
Fig. III-10. Photoluminescence energies and energy gap for $Zn_{1-x}Cd_xTe$ alloys at 4.2°K, plotted against mole-fraction CdTe.

Figure III-10 shows the luminescence data for the ZnTe-CdTe alloys. In addition to the oxygen band, a second band at somewhat higher energy was observed in all these samples. Because there is some overlap between the oxygen band and the second band (which is presumably due to an unknown impurity originating in the CdTe), the no-phonon energy for the oxygen band cannot be determined from the wavelength at 15-percent intensity. Therefore, Fig. III-10 includes only the photon energy at the peak of the oxygen band, the energy at the peak of the second band, and the energy gap for the ZnTe-CdTe alloys, which is reported to vary linearly[12] or almost linearly[13] with composition. In contrast to the results for the alloys with ZnSe or ZnS, the energy of the oxygen luminescence band decreases with increasing CdTe content. The data are well represented by a straight line whose slope is approximately the same as the slope of the energy gap. Thus, E_t remains essentially constant over the composition range investigated, as expected for the isoelectronic trap model.

<div align="right">

G. W. Iseler
A. J. Strauss

</div>

D. COMPOSITION- AND PRESSURE-INDUCED STRUCTURAL CHANGES IN THE $Ba_{1-x}Sr_xRuO_3$ SYSTEM

The structural chemistry of many inorganic compounds with the general formula ABX_3, where A and B are cations and X is an anion, can be described in terms of hexagonal and/or cubic close packing of AX_3 layers with the B cations filling the X_6 octahedra thus formed.[14] When all layers are hexagonal close packed, the octahedra share faces with each other to form chains [Fig. III-11(a)]. When all layers are cubic close packed, the octahedra form a three-dimensional array by sharing only corners, giving the perovskite structure [Fig. III-11(b)].

If structures with mixtures of hexagonal and cubic close-packed layers are allowed, one might expect an infinite number of possible structures. However, there appear to be only three intermediate stacking sequences in actual compounds. The one most closely resembling cubic close packing has a 6-layer (6L) sequence cchcch [Fig. III-11(c)], where c and h represent cubic and hexagonal closed-packed layers, respectively. The structure having equal amounts of hexagonal and cubic close packing has a 4-layer (4L) sequence chch [Fig. III-11(d)]. The last known
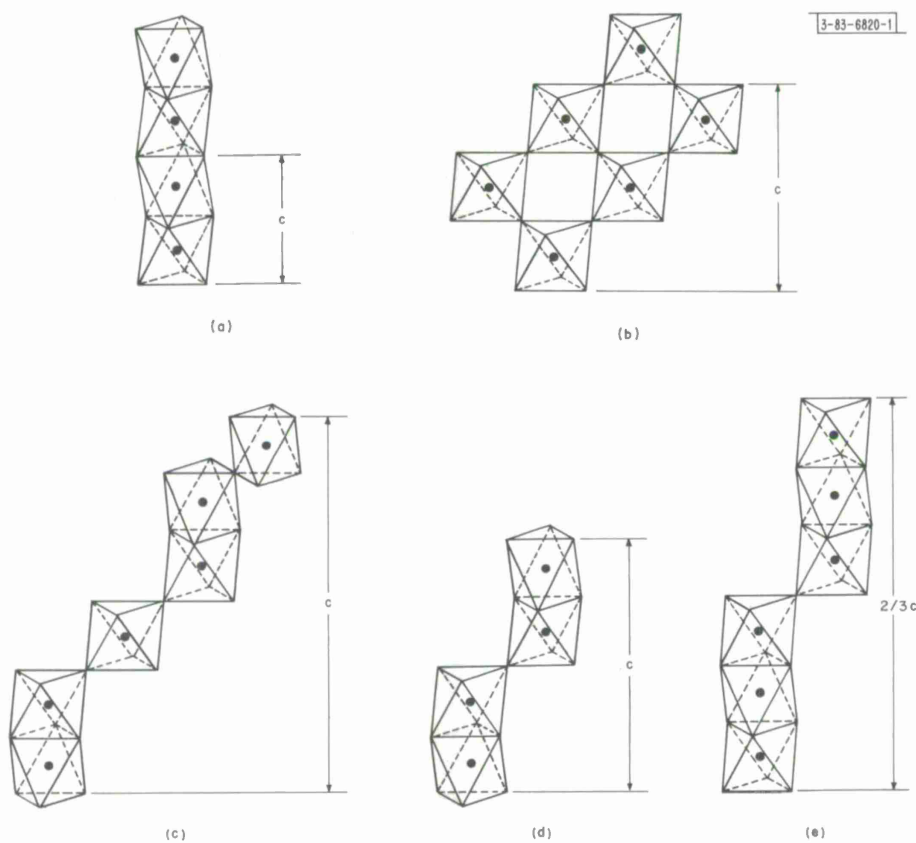
Fig. III-11. Schematic of [110] plane of hexagonal cell for ABX$_3$ structures showing face and corner sharing by octahedra between AX$_3$ layers; c represents c-parameter of crystal.

intermediate structure has predominantly hexagonal close packing with the 9-layer sequence hhchhchhc [Fig. III-11(e)]. Katz and Ward[15] have discussed in detail the structural relation of all these types plus some of the unknown possibilities. The system Ba$_{1-x}$Sr$_x$RuO$_3$ (Ref. 16) is of interest since one is able to study the effects both of A cation size and of pressure on the structural transformations from the 9-layer compound (BaRuO$_3$) through the 4- and 6-layer phases to the perovskite (SrRuO$_3$). The strontium-rich members are also interesting since they exhibit spontaneous magnetism.

In the present investigation, ambient pressure material was prepared by the solid state reaction of BaCo$_3$-SrCO$_3$ mixtures with Ru metal at temperatures up to 1100°C. The preparation of high-pressure phases was carried out in cylindrical gold or platinum capsules in a belt apparatus. The temperature was raised after application of pressure, held for one-half hour, and then rapidly quenched before the pressure was released. Phase and structural data were obtained by analyzing x-ray diffraction patterns for powdered samples measured with a Norelco x-ray diffractometer using monochromatic CuKα radiation. The concentration of the components in two-phase samples was estimated from the relative intensities of the lines in the diffraction patterns.
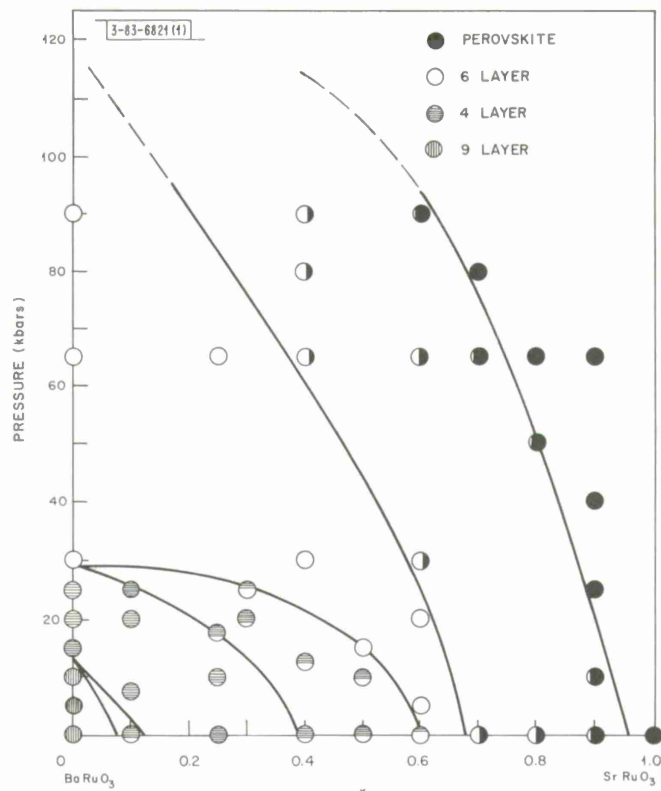
Fig. III-12. Pressure-vs-composition phase diagram for $Ba_{1-x}Sr_xRuO_3$ system at 1000°C.

The results of this investigation are summarized in the pressure-vs-composition plot shown in Fig. III-12 for the system at 1000°C. It can be seen that the addition of strontium and the application of pressure both favor structures with more cubic close packing. Both effects tend to decrease the B-B distances and therefore to make the face sharing of octahedra (associated with hexagonal close packing) less stable. In the 6-layer region with high strontium content, distortion of the normal hexagonal unit cell (a $\cong$ 5.6 Å, c $\cong$ 13.9 Å) produces diffraction line splitting. The splitting can be attributed to a monoclinic distortion with a $\neq$ b and $\gamma \neq 60°$. Even in the most distorted structures, the deviation from a hexagonal unit cell is less than 4 percent.

<div style="text-align:right">

J. M. Longo   D. A. Batson
J. A. Kafalas   T. W. Hilton

</div>

E. DETERMINATION OF EXPERIMENTAL FORM FACTORS ON AN ABSOLUTE SCALE FROM RELATIVE X-RAY INTENSITIES

The controversy about experimental determination of atomic form factors in solids, by means of x-ray diffraction intensity measurements, relates only to results on an absolute scale. On a relative scale, all the available experimental results agree.[17] An alternate method of evaluating the scaling constant would thus be useful.

The form factor can be represented by the parametric expression

$$f(s) = \sum_j \alpha_j \exp[-\beta_j s^2]$$

where $s = |k|/4\pi = (\sin\Theta)/\lambda$, with Θ the Bragg angle and λ the wavelength, and the α's and β's are Gaussian coefficients. We require the form factor to satisfy the two conditions $f(s = 0) = Z$, where Z is the atomic number, and $f(s \geqslant s_c) = f°(s \geqslant s_c)$, where s_c is the reciprocal lattice vector value at which the outer electrons' contribution to the scattering is negligible and $f°(s)$ is the theoretical free atom form factor. This allows a least-squares determination of the scaling constant as well as the Debye-Waller temperature parameter $B(T)$ and the α's and β's.

This method has been applied to our relative x-ray intensity data on Ni metal (Table III-1), which are in excellent agreement with previous results[18] collected with the same radiation (filtered MoKα radiation). Figure III-13 shows our values for the relative structure factor $J(s) = [I(s)/mP(\Theta)]^{1/2}$, where $I(s)$ is the integrated intensity on a relative scale, m is the plane

TABLE III-1				
INTEGRATED INTENSITIES OF X-RAY DIFFRACTION LINES FOR Ni				
$\dfrac{\sin\theta}{\lambda}$	hkl	$I(s)^\dagger$	$I(s)\ cal^\ddagger$	$P(s)^\S$
0.2458	111	351.84	349.78	351.01
0.2838	200	169.84	169.06	170.82
0.4013	220	101.13	100.04	99.60
0.4706	311	104.65	104.43	103.23
0.4915	222	28.91	28.84	28.22
0.5676	400	11.48	11.42	10.88
0.6185	331	29.29	29.74	29.26
0.6346	420	26.03	25.56	25.70
0.6951	422	16.56	16.53	16.16
0.7373	333,511	16.21	16.29	15.88
0.8027	440	3.80	3.96	3.85
0.8394	531	12.79	12.80	12.63
0.8514	442,600	7.56	7.38	7.58
0.8974	620	4.45	4.57	4.44
0.9305	533	3.95	3.87	4.06
0.9412	622	3.67	3.68	3.75
0.9831	444	1.02	1.02	1.01
1.0133	551,711	5.59	5.44	5.58
1.0232	640	2.73	2.62	2.75
1.0618	642	4.61	4.62	4.79
1.0899	553,731	6.33	6.41	6.60
1.1351	800	0.53	0.48	0.51
1.1614	733	⎰1.89	1.88	1.92
1.1701	644,820	⎱3.71	3.69	3.80
1.2040	660,822	2.65	2.69	2.64
1.2288	555,751	⎰4.17	4.34	4.26
1.2370	662	⎱1.82	1.80	1.87
1.2691	840	1.85	1.83	1.90
1.2927	753,911	⎰5.79	5.73	5.95
1.3005	842	⎱3.91	3.87	4.02

$\dagger$ Observed intensities. The lines joined by a brace were overlapping. They have been counted together and resolved according to the theoretical ratio.

$\ddagger$ Values calculated from the Gaussian polynomial representing the data.

$\S$ Experimental results of Ref. 18.
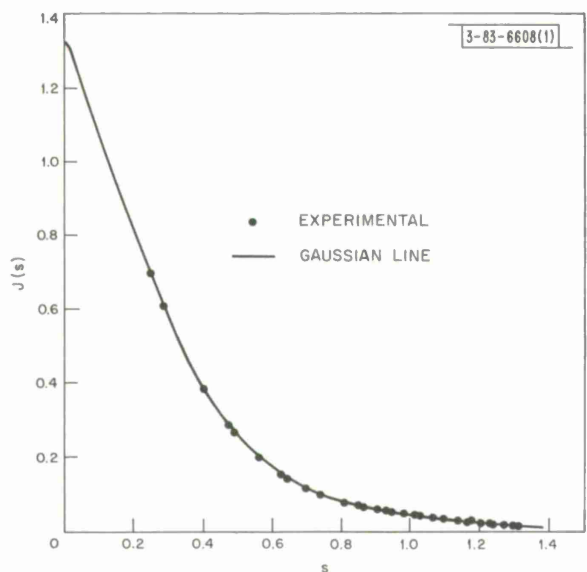
Fig. III-13. Relative structure factor J(s) as function of $s = (\sin \theta)/\lambda$ for Ni metal.

TABLE III-2		
VALUES OF X-RAY PARAMETERS FOR Ni BEFORE AND AFTER REFINEMENT		
	Initial	Final
c	0.0020	0.00166
α_1	1.2640	1.27705
β_1	0.0020	0.11825
α_2	13.2174	13.2296
β_2	3.7504	3.72131
α_3	7.1019	7.06452
β_3	0.2671	0.24092
α_4	4.1801	4.18757
β_4	12.4514	13.14709
α_5	2.2246	2.24115
β_5	60.3462	173.81097
B(T)	0.381	0.3705
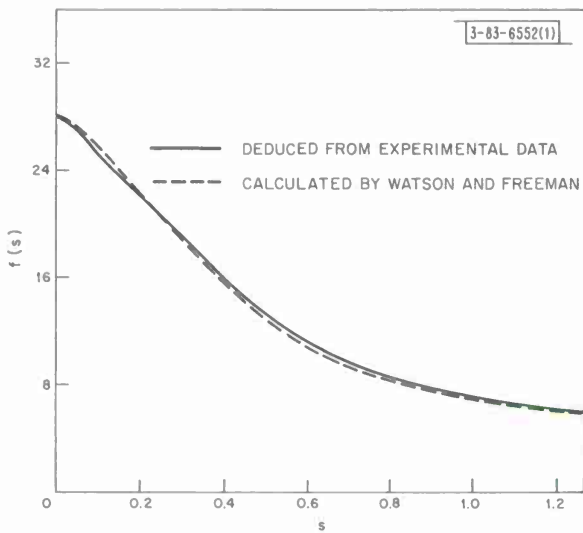
Fig. III-14. Atomic form factor obtained from experimental data for Ni metal compared with theoretical free atom form factor calculated by Watson and Freeman (Ref. 20).
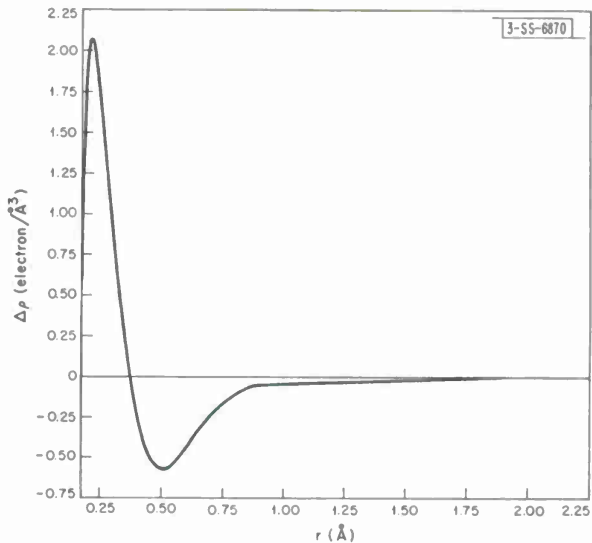
Fig. III-15. Difference ($\Delta\rho$) between charge distribution obtained from experimental data for Ni metal and theoretical charge distribution for free Ni atom, as function of distance (r).

multiplicity, and $P(\Theta)$ is the Lorentz and polarization correction. Figure III-13 also shows the Gaussian line best representing the J values. Table III-2 lists the parameters before and after least-squares refinement. The initial α and β values are those obtained by Cromer and Waber[19] for the free Ni atom. The accuracy of the fit in Fig. III-13 averages 2 percent, the same as our experimental error and our discrepancy with previous results. In this experiment, the major difficulty is in making the background determinations with sufficient accuracy.

In Fig. III-14, the theoretical free atom form factor for the electronic configuration $3d^8 4s^2$ (Ref. 20) is compared with the best Gaussian representation of our results for the form factor of solid Ni. One sees that there is a systematic deviation which reaches a maximum of 3 percent for $s \sim 0.6$. This is small but probably outside the experimental error. Fourier inversion of the two Gaussian representations yields the atomic charge distributions for the free atom and for the solid. The difference between these distributions is shown in Fig. III-15, where one sees that the atom in the solid has more electrons than the free atom in the region from 0.17 to 0.37 Å, and less between 0.37 Å and infinity. This suggests a transfer from the outer levels (4s) to the first inner levels (3d). Since 0.32 Å is the position of the 3d level in the free Ni atom,[20] numerical integration of the real space charge density suggests a transfer of 0.3 electron, a value smaller than suggested by the magnetic moment. However, the accuracy of this determination is poor, and the result should be considered as qualitative.

It appears that the scaling method proposed here preserves the information concerning the outer electron distribution which is lost when the theoretical free atom form factor is used in scaling over the whole experimental range. The very slight difference from the free atom distribution found for Ni suggests an electronic configuration $3d^{8+\delta} 4s^{2-\delta}$, where $\delta = 0.3$. Further work could convert this qualitative result to a quantitative value having a known accuracy.

P. M. Raccah
V. E. Henrich

33

REFERENCES

1. Solid State Research Report, Lincoln Laboratory, M.I.T. (1964:4), p. 23, DDC 613961, H-639.

2. Ibid. (1965:1), p. 41, DDC 622446, H-678.

3. T. B. Reed and W. J. LaFleur, Appl. Phys. Letters 5, 191 (1964), DDC 618455.

4. K. Itoh, J. Phys. Soc. Japan 22, 1119 (1967); Proceedings of the International Conference on II-VI Semiconducting Compounds (W. A. Benjamin, Inc., New York, 1967), p. 1296.

5. Solid State Research Report, Lincoln Laboratory, M. I. T. (1968:1), p. 19, DDC 668762.

6. D. T. F. Marple, Phys. Rev. 150, 728 (1966).

7. G. A. Saum and E. B. Hensley, Phys. Rev. 113, 1019 (1959).

8. R. E. Dietz, D. G. Thomas, and J. J. Hopfield, Phys. Rev. Letters 8, 391 (1962).

9. J. J. Hopfield, D. G. Thomas, and R. T. Lynch, Phys. Rev. Letters 17, 312 (1966).

10. J. L. Merz, Bull. Am. Phys. Soc. 13, 454 (1968).

11. S. Larach, R. E. Shrader, and C. F. Stocker, Phys. Rev. 108, 587 (1967).

12. B. T. Kolomiets and A. A. Mal'kova, Sov. Phys. – Tech. Phys. 3, 1532 (1958).

13. F. F. Morehead and G. Mandel, Phys. Rev. 137, A924 (1965).

14. A. F. Wells, Structural Inorganic Chemistry, 3rd edition (Oxford at Clarendon Press, London, 1962), pp. 112 – 129.

15. L. Katz and R. Ward, Inorg. Chem. 3, 205 (1964).

16. P. C. Donohue, L. Katz, and R. Ward, Inorg. Chem. 5, 335 (1966).

17. P. M. Raccah and R. J. Arnott, Phys. Rev. 153, 1028 (1967), DDC 651719.

18. O. Inkinen and P. Suortti, Ann. Acad. Sci. Fennicae, Ser. A. VI. 147 (1964).

19. D. T. Cromer and J. T. Waber, Acta Cryst. 18, 104 (1965).

20. R. E. Watson and A. J. Freeman, Phys. Rev. 120, 1125 (1960).

IV. PHYSICS OF SOLIDS

A. ELECTRONIC BAND STRUCTURE

1. Optical Properties of Nickel-Copper Alloys from 0.2 to 11 eV

Our investigation of the band structure of nickel, through optical studies, has led us to the nickel-copper disordered alloy system. Experimental measurements[1] and band calculations[2] indicate an energy band picture for copper and nickel, around the L point in the Brillouin zone, as shown in Fig. IV-1. Also given here are the low-energy transitions observed in nickel[1] and the reversal, between copper and nickel, of the L_{32} d-like and the L'_2 p-like states. It seemed logical to test the band model for nickel, which is less well established than that of copper, by looking at the optical properties of the alloy system of these two elements; they lie next to each other in the periodic table, copper having one more electron. As a result, we find that the alloy system is interesting in its own right.

We have measured the reflectance of single crystals of several alloys from 0.2 to 11 eV. Figure IV-2 shows the reflectance of a high-nickel and a high-copper alloy along with pure nickel and pure copper. The curves for the pure metals are virtually the same as those reported by Ehrenreich, et al.,[1] and Beaglehole.[3] The 0.4-eV shoulder in nickel is absent at room temperature in the 61-percent nickel alloy. At 77°K, in measurements not shown, a small kink in the curve for the 61-percent nickel alloy does seem to occur at 0.3 eV; this may be related to ferromagnetic behavior. We have previously interpreted this structure in nickel as a minority spin band transition from L'_2 to L_{32} (see Ref. 1).
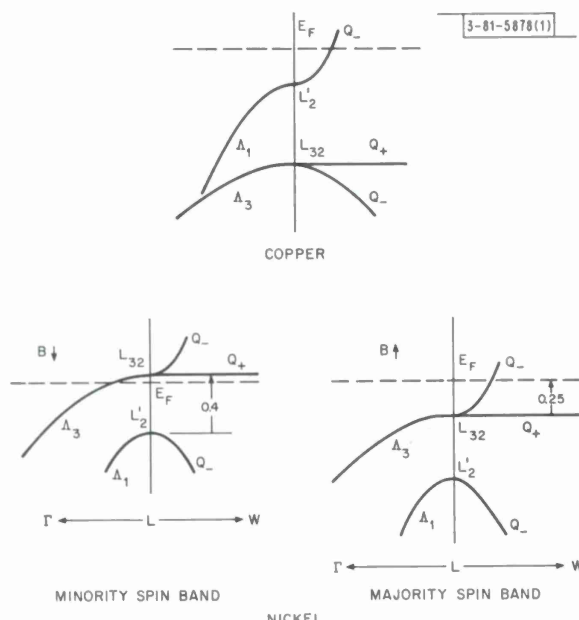
Fig. IV-1. Energy bands of nickel and copper near L point in Brillouin zone.
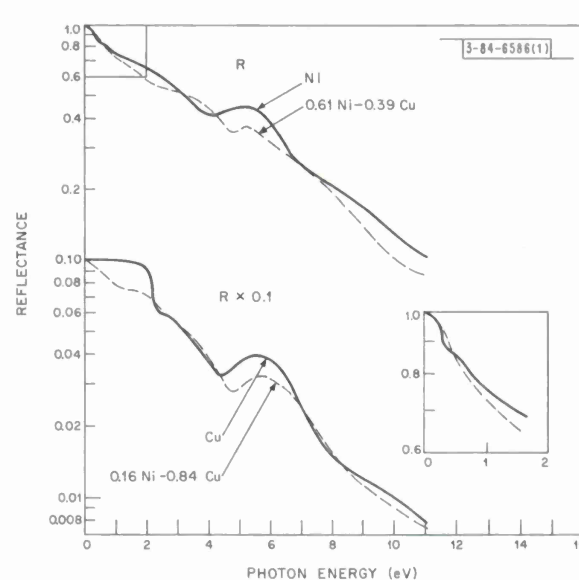
Fig. IV-2. Reflectance at room temperature of nickel, copper, and two alloys of these metals.

In the high-copper curves, even with 16-percent nickel, the reflectance starts dropping immediately rather than staying at a high value. In the three samples with copper, there is consistently a distinct change in slope near 2 eV, characteristic of the first interband transition in copper from the d-bands to the Fermi surface. This edge does not shift as we would expect if an average potential or rigid band model applied to the alloy system. In either of these models, adding nickel to copper would change the d-band Fermi surface separation and shift the energy of the first interband transition. The recent limited data of Schröder and Önengüt[4] on alloys with as low as 2-percent nickel also show a drop in the low-energy reflectance with the edge remaining at 2 eV.

At higher energies, other changes occur. The 61-percent nickel alloy shows a broad peak occurring between 2 and 5 eV, with a distinct narrowing and lowering of the peak at 5.2 eV. A similar but not so distinctive change occurs in the high-copper samples.

Our results are related to band models by using a Kramers-Kronig analysis to compute the imaginary part of the dielectric constant ϵ_2. Figure IV-3 shows ϵ_2, which is proportional to the joint density of states for interband transitions. The suggestion from the reflectance data, that the 2-eV transition in copper does not shift as nickel is added, is confirmed by the ϵ_2 curves. The nonshift of the 2-eV copper absorption is clearly evident as a knee in the 16-percent nickel alloy spectrum and an inflection point in the 61-percent nickel alloy. In the 16-percent nickel alloy, a rise in ϵ_2 above that of the free electron behavior of copper is obtained. This apparently comes from low-energy transitions to the Fermi surface from states near the Fermi surface.

At higher energies, the detailed picture for the alloys is less clear but it appears that other band models, such as the "virtual states" model of Friedel[5] and Anderson,[6] and the "minimum polarity" model recently discussed by Lang and Ehrenreich,[7] must be considered in order to explain the data below 4 eV. The "rigid band" model is inadequate. Recent optical and photoemission results of Seib and Spicer[8] should provide complementary information. We are planning further measurements on high-copper alloys where the change in optical properties is most drastic.
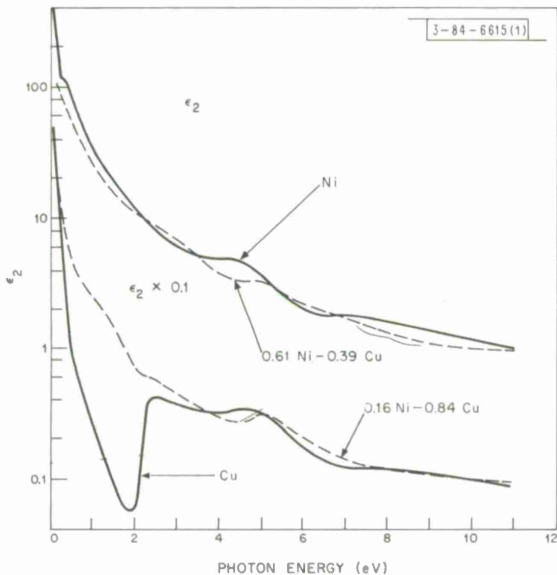
Fig. IV-3. Frequency variation of imaginary part of dielectric constant ϵ_2.

W. J. Scouler
J. Feinleib
J. Hanus

2. Optical Studies in Bismuth-Doped Silicon

Measurements (which were described in the previous Solid State Research Report[9]) have been completed of the optical absorption due to low-energy transitions of isolated bismuth impurity atoms in silicon at low temperatures as a function of the polarization of the infrared light beams

and the orientation of the uniaxial stress applied to the sample. Uniaxial stresses up to 6×10^8 dynes/cm^2 were applied in the [001], [110], and [111] crystal directions, with the $\vec{E}$ vector of the light parallel or perpendicular to the applied stress. An example of the data is given in Fig. IV-4, showing the transmission, in arbitrary units, for an applied stress of 1.17×10^8 dynes/cm^2 in a [001] crystal direction. The zero stress transition energies are also indicated on the figure.

All measured relative intensities and transition energies as a function of strain are in agreement with predictions based on the assumption that the transitions are from the $1s(A_1)$ ground level (of T_d symmetry) to the $1s(T_2)$ level, where the T_2 level is split by spin-orbit coupling, and the form of the strain Hamiltonian is derived from effective mass and deformation potential theory.

W. E. Krag
W. H. Kleiner
H. J. Zeiger

3. Interband Magnetoreflection in Gray Tin

Two sets of interband transitions have been observed in the magnetoreflection of gray tin. One set has been seen at photon energies between 0.425 and 0.55 eV. Points from these transitions extrapolate to a zero magnetic field energy gap of 0.413 eV. From the band structure of gray tin[10] shown in Fig. IV-5, we identify these transitions as taking place between the Γ_7^- valence band and the Γ_8^+ conduction band, and represent them by arrow A. The second set of transitions (arrow B in Fig. IV-5) has been observed in the range of photon energies between 0.045 and 0.55 eV. These take place from the Γ_8^+ valence band to the Γ_8^+ conduction band across the zero thermal energy gap.
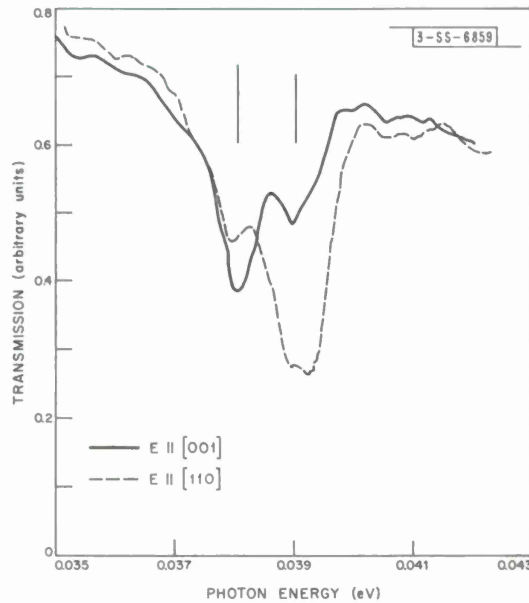
Fig. IV-4. Transmission vs photon energy of bismuth-doped silicon for uniaxial applied stress of 1.17×10^8 dynes/cm^2 in [001] crystal direction for $\vec{E}$ polarized parallel and perpendicular to applied stress. Zero stress positions of absorptions are indicated by vertical lines.
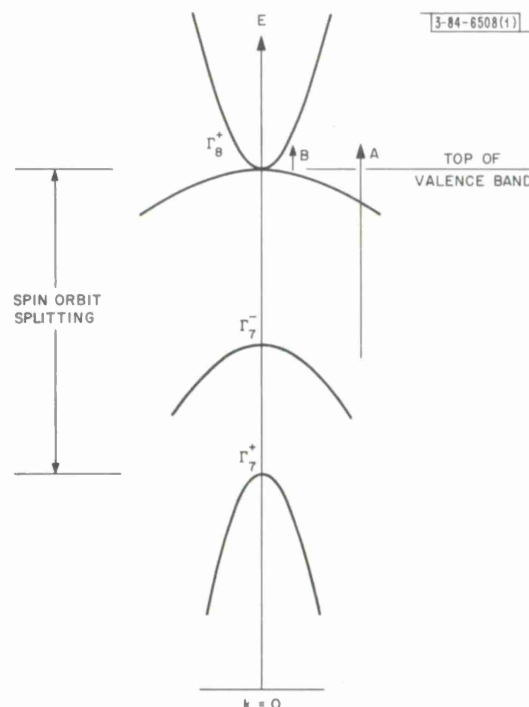
Fig. IV-5. Band structure of gray tin showing highest valence bands and lowest conduction band about $\vec{k} = 0$. Arrows show transitions seen in magnetoreflection.

For this experiment, we have used high-purity gray tin which has $n_o \sim 5 \times 10^{14}$ cm^{-3}, where n_o is the density of donor impurities minus the density of acceptor impurities. This impurity concentration is at least a factor of 10 lower than that found in the best commercially available tin. The improvement in purity is accomplished with a solvent extraction process using the tin-mercury alloy system. In our experiment, light is reflected off a natural facet of a crystal, and most of our measurements have been made on a crystal with a (100) face. We have worked in the Faraday configuration, with the direction of light propagation parallel to the magnetic field $\vec{H}$; therefore, our data are characteristic of $\vec{H}$ perpendicular to the (100) plane.

The magnetoreflection results for gray tin are very similar to those for HgTe (see Ref. 11) but are more interesting for a comparison with theory for several reasons. First, as mentioned above, they are characteristic of a single, high-symmetry direction; such results could not be achieved in HgTe because of a materials limitation. This is especially important for fitting the $\Gamma_8^+ \to \Gamma_8^+$ transitions. Second, the warping of the Γ_8^+ bands, a parameter which is needed in the theory, has been measured for gray tin.[12] Third, the complications which may be introduced by the inversion asymmetry of zincblende HgTe are absent for gray tin, which has inversion symmetry.

A matrix Hamiltonian, which includes the full interaction between Γ_7^+, Γ_7^-, and Γ_8^+ bands and includes higher band interactions to order k^2, has been used to calculate the magnetic energy levels.[13] A shortcoming of this theory for both gray tin and HgTe is that the interaction between Γ_8^+ and the Γ_{15} conduction band (using a mixture of single- and double-group notations) is included only to order k^2. Thus, while the nonparabolicity of the Γ_8^+ conduction band caused by the interaction between Γ_7^- and Γ_8^+ bands is included, the nonparabolicity of the band caused by the Γ_{15} band is not.

Figures IV-6 and IV-7 show the transition energies vs magnetic field for the $\Gamma_7^- \to \Gamma_8^+$ and $\Gamma_8^+ \to \Gamma_8^+$ transitions, respectively. The solid curves are theoretical and give a good fit to both
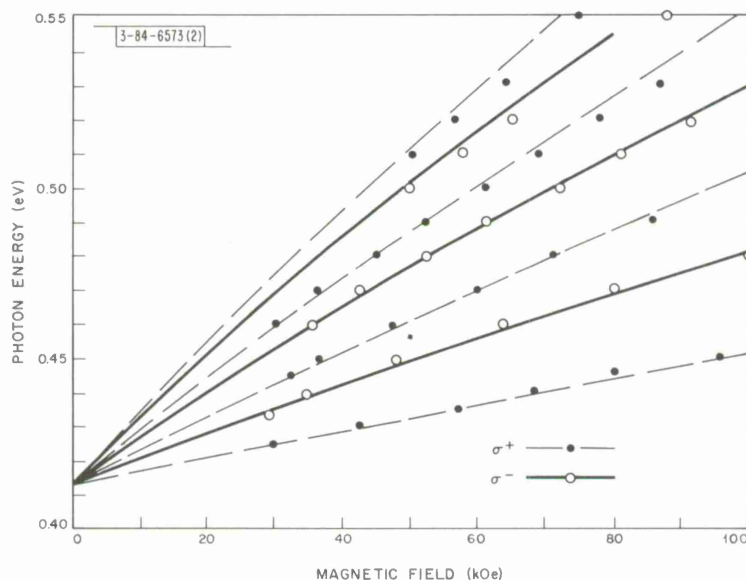
Fig. IV-6. Transition energies in σ^- and σ^+ polarizations for $\Gamma_7^- \to \Gamma_8^+$ transitions are indicated by open and closed circles. Solid and dashed curves are theoretical energies for two polarizations.
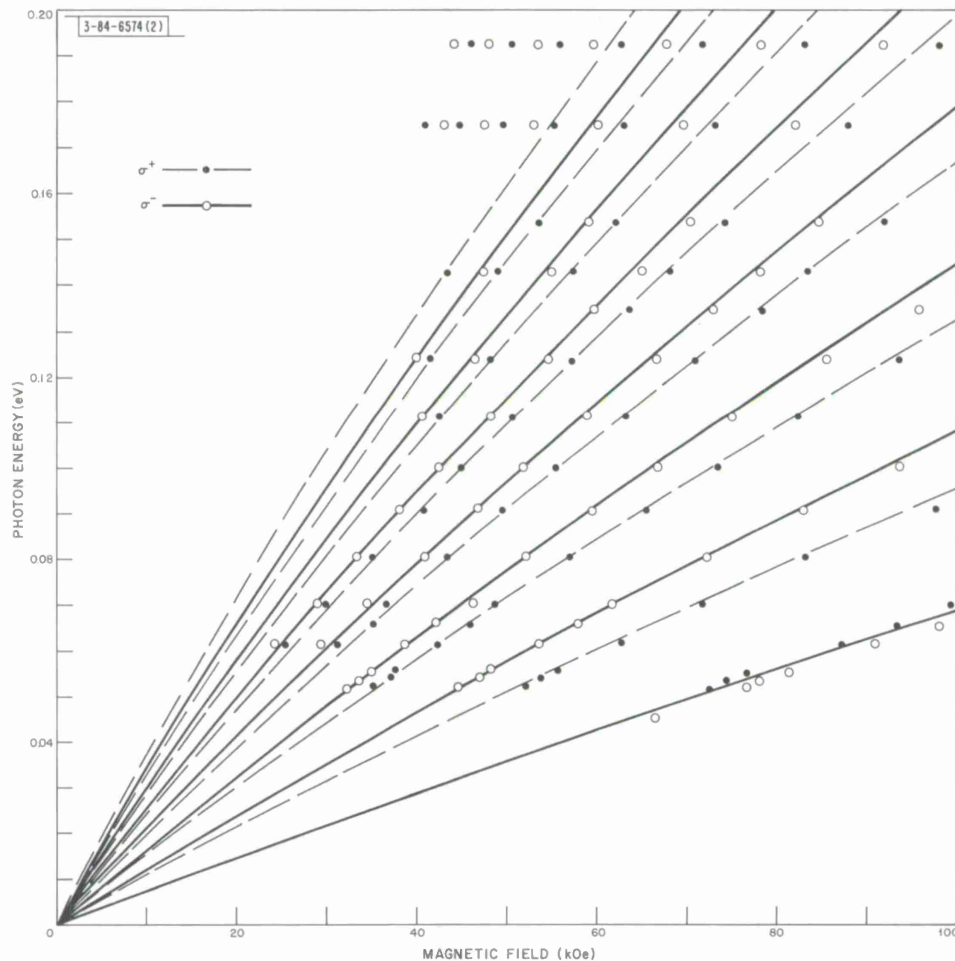
Fig. IV-7. $\Gamma_8^+ \to \Gamma_8^+$ transition energies showing experimental points and theoretical curves with same convention as in Fig. IV-6. These transitions have been seen up to 0.55 eV, but are plotted here to only 0.2 eV.

sets of transitions. The data of Fig. IV-6 were taken with the sample at ~1.5°K, and those of Fig. IV-7 with the sample at ~20°K. We have measured the transitions of Fig. IV-6 at 20° and ~85°K and cannot detect any shift of the resonant energies. This is in marked contrast to HgTe which shows large temperature-induced shifts.[14]

The systematic deviation at high photon energies for both sets of transitions, with the experimental points lying below the theoretical curves, is caused by the nonparabolicity of the Γ_8^+ conduction band induced by the Γ_{15} conduction band, as mentioned above. This effect has been discussed previously.[11] One interesting feature of the low-energy transitions is that they give the Γ_8^+ valence band mass directly. This is evident from an examination of the Landau levels for these transitions, shown in Fig. IV-8. The spin splittings of Γ_8^+ valence and conduction bands are nearly equal, which means the two σ^+ ($\Delta n = +1$) transitions from the n valence sub-band to the n + 1 conduction sub-band are nearly degenerate in energy. The same is true of the σ^- ($\Delta n = -1$) transitions. Thus, the spacing in Fig. IV-7 between σ^- transitions, or between σ^+ transitions, is

3-84-6767(1)

ENERGY (eV)

Γ_8^+

a SET   b SET
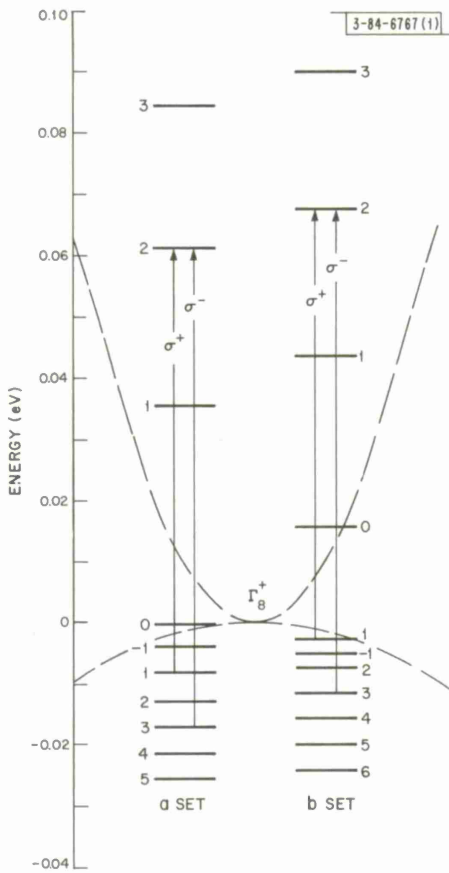
Fig. IV-8. Lowest Landau levels for Γ_8^+ bands at 70 kG. Arrows show optical transitions to n = 2 levels of conduction band. Difference between σ^+ and σ^- transition energies to a given conduction band level is direct measure of valence band level spacing.

the usual reduced mass cyclotron energy. However, the spacing between σ^+ and σ^- transitions to the same conduction sub-band is twice the valence band cyclotron energy.

The lowest σ^+ transition in Fig. IV-7 is at too high an energy to be part of the Landau level transitions shown in Fig. IV-8. Our suspicion is that it is a transition from an impurity ground state, associated with the n = 0 conduction band Landau level to an excited impurity state associated with, and lying below, the n = 2 conduction sub-band. The observation of impurity transitions similar to this in p-type InSb and germanium[15] makes this plausible from an experimental point of view. Evidence has been presented recently for discrete impurity levels in gray tin under uniaxial stress which causes the splitting of the Γ_8^+ bands.[16] It would not be surprising if a similar effect were caused by a high magnetic field.

The following parameters[11] have been used to generate the theoretical curves: $E(\Gamma_8^+) - E(\Gamma_7^-) = 0.413$ eV; $E(\Gamma_8^+) - E(\Gamma_7^+) = 0.80$ eV; $E_P = 24.5$ eV; $\gamma_1 = 4.42$; $\gamma_2 = -1.35$; $\gamma_3 = 1.35$; and $\kappa = -3.0$. The band edge masses corresponding to this set of parameters, in units of the free electron mass, are $m_c(\Gamma_8^+) = 0.028$, $m_v(\Gamma_8^+) = -0.195$, $m(\Gamma_7^-) = -0.057$, and $m(\Gamma_7^+) = -0.051$.

In addition to the work on the lowest σ^+ transition ($\Gamma_8^+ \rightarrow \Gamma_8^+$), we are hoping to obtain more information in the near future about the Γ_{15} conduction band, from its nonparabolic effect on the Γ_8^+ conduction band, and to make a detailed comparison of our magnetoreflectivity results with those from other experiments, especially the conduction band mass determinations from the oscillatory magnetoresistance.[12,17]

S. H. Groves   A. W. Ewald
C. R. Pidgeon   R. J. Wagner

4. Inversion Asymmetry and Warping-Induced Interband Magneto-Optical Transitions in InSb

We have completed a study of "extra" transitions in the interband magnetoreflection and magneto-electroreflection of InSb, caused by the warping and by the linear-$\vec{k}$ splitting of the valence band. An unambiguous assignment of the transitions is made from a study of the anisotropy of the spectra, using left- and right-circularly polarized light, with the magnetic field along [100], [110], [111], and [211] directions of the crystal. From the relative strength and energies of these transitions, we are able to determine the size of the warping and linear-$\vec{k}$ terms in the effective mass Hamiltonian. We find the warping parameter $(\gamma_3 - \gamma_2) = 1.0$, and the linear-$\vec{k}$ parameter C = 4.2 eV-cm. The error in the determination of $(\gamma_3 - \gamma_2)$ is about 15 percent, and that in the determination of C is about 30 percent. The result for $(\gamma_3 - \gamma_2)$ is in good agreement with the cyclotron resonance work of Bagguley, et al.,[18] but not with the more recent work of Tohver and Ascarelli.[19] The value of C is about three times smaller than suggested by Robinson,[20] but is in good agreement with the theoretical estimate of Kane.[21]

A short report of this work has been published in the Physical Review Letters.[22] A longer version, with full account of the experimental and theoretical details, is being prepared currently.

<div style="text-align: right">S. H. Groves
C. R. Pidgeon</div>

5. Determination of Debye Temperatures from Thermal Modulation of X-Ray Diffraction

The usual method of measuring the Debye temperature Θ_D, in terms of x-ray diffraction intensities, consists of measuring the difference between the Debye-Waller factors at two fairly distant temperatures.[23] This method precludes the possibility of making detailed studies of Θ_D in any small temperature range, and thus is not useful for studying critical transitions. We have measured the temperature derivative of the Debye-Waller factor at one temperature directly by synchronous detection of the diffracted x-ray beam from a thermally modulated sample. As the temperature of a crystal used as sample in an x-ray diffractometer is raised, thermal expansion of the lattice shifts the Bragg peaks toward lower angle. For a cubic crystal, this can be written as

$$\frac{d(2\Theta_o)}{dT} = - \frac{\lambda \sqrt{h^2 + k^2 + \ell^2}}{a \cos \Theta_o} \left(\frac{1}{a} \frac{da}{dT} \right) \tag{1}$$

where Θ_o is the Bragg angle, T is the temperature, λ is the x-ray wavelength, a is the cell edge, and (hkℓ) is the diffracting planes. At the same time, the increased atomic motion changes the intensities of the peaks, in general reducing them. For a simple lattice, this is taken into account by the Debye-Waller factor B(T), which multiplies the T = 0° intensity in the form

$$I(T) = I(0) e^{-2B(T) S^2} \tag{2}$$

where $S \equiv \sin \Theta / \lambda$. Thus,

$$\frac{dI}{dT} = -2 \left[\frac{dB(T)}{dT} \right] S^2 I(T) \quad . \tag{3}$$
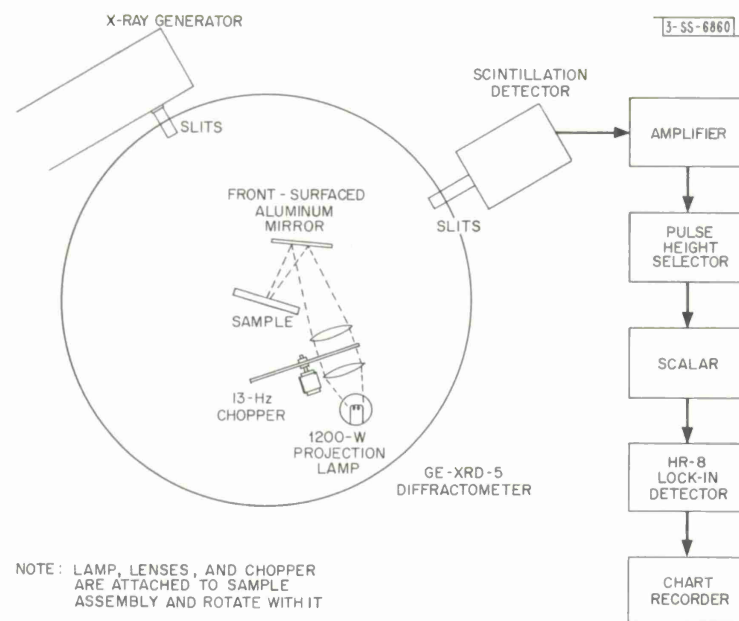
Fig. IV-9. Experimental setup for thermal modulation.

If the sample temperature is modulated and the diffractometer angle is held constant, the thermal expansion appears in the AC component of the diffracted beam as the angular derivative of the lineshape, while the intensity change gives a signal proportional to the lineshape. Analysis of the resulting signal yields the relative amounts of these two components. Then, if $(1/a)$ (da/dT) is known, dB/dT can be determined.

By using chopped radiation from a projection lamp focused on the sample (Fig. IV-9) to modulate the temperature (modulation amplitude $\sim 0.01°$ to $0.1°C$), signals of the form shown in Fig. IV-10 have been obtained with single-crystal NaCl. Most of the signal is due to thermal expansion, but careful examination shows the presence of a small contribution from the changing phonon density. In practice, only the region near the zero of signal is measured, since the location of the zero uniquely determines the amount of each component present. Several runs have been made with both CuKα and MoKα radiation, and the results are presented in Table IV-1.

When the theory is extended to a diatomic crystal, an average Debye-Waller factor can be defined, and this is the quantity whose derivative is given in Table IV-1. Within the limits of the Debye theory, which predicts $dB/dT > 0$ always, the usual Debye temperature can be determined directly from dB/dT. This has been done for the CuKα result, and there is good agreement with the values of $\Theta_D \cong 290°K$ determined by other methods.

Fig. IV-10. Thermal modulation signal vs 2Θ. Kα_1 and Kα_2 were partially resolved in x-ray lineshape.

TABLE IV-1			
dB/dT COMPUTED FROM THERMAL MODULATION DATA			
(hkℓ)	Radiation	dB/dT (Å/°C) × 10³	θ_D (°K)
(400)	CuKα	+5.11 ± 1.2	281 $\begin{cases} +26 \\ -31 \end{cases}$
(400)	MoKα	+0.107 ± 1.24	−
(600)	MoKα	−0.76 ± 1.26	−
(800)	MoKα	−1.79 ± 0.70	−
(10,0,0)	MoKα	−2.34 ± 0.76	−

Under any reasonable assumptions, dB/dT should be independent of (hkℓ) and the x-ray wavelength, and we should obtain the same value in all our measurements. We believe that the strange results obtained with MoKα radiation are due to extinction.[24] CuKα radiation penetrates only about 60 μm into NaCl, and any surface damage probably extends this far into the crystal, resulting in a mosaic structure with little extinction. However, MoKα radiation extends about 560 μm into NaCl, where surface damage should be absent and extinction could be expected to occur. Since the amount of extinction depends on the state of perfection of the lattice, we believe that the thermal gradients set up in the sample cause periodic variations in strain which modulate the strength of the extinction and hence the intensity of the diffracted beam. This effect has been observed directly in quartz,[25] and its size could easily be orders of magnitude larger than the Debye-Waller factor contribution. Tests are currently under way to determine the amount of extinction quantitatively.

Several criteria affect the accuracy obtainable from this type of measurement. Clearly, extinction effects must be eliminated. Sandblasting of the crystal surface and use of very soft x-rays which do not penetrate deeply into the sample should overcome this difficulty in most materials. Also, materials with lower thermal conductivities will have larger temperature oscillations and hence larger signals. The use of faster detector and electronics would permit use of a larger photon flux (we are limited to 30,000 photons per second). Digital rather than analog measurement of the signal would both simplify data analysis and increase accuracy.

With the improvements mentioned above, this technique could be improved to the point of surpassing existing DC methods. In addition, the ability to measure θ_D at only one temperature gives this method excellent resolution in temperature, making it valuable in the study of phonon densities around critical transitions.

V. E. Henrich
P. M. Raccah

6. Microwave Acoustic Amplification in n-InSb at 9 GHz

Acoustic amplification was observed on applying a pulsed electric field, up to 40 V/cm, to a rod-shaped sample of n-InSb at 4.2°K. The electric field, which was on during the transit time of the acoustic pulse down the sample (about 2 μsec), produced a maximum observed change in attenuation of −41 db/cm. Typical results are shown in Fig. IV-11 for an applied field of 40 V/cm.

A — CAVITY EXCITATION PULSE
B — VIDEO DETECTOR OUTPUT
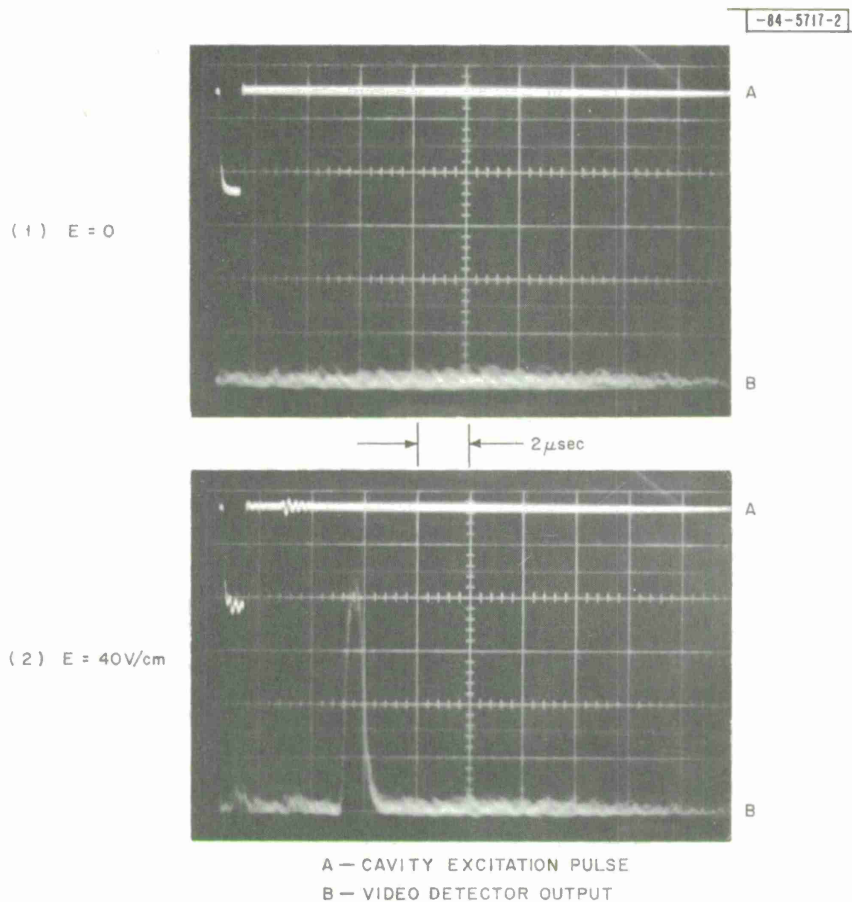
Fig. IV-11. Output of receiver video detector with and without electric field applied.

The observed amplification was enhanced by a small magnetic field (typically less than 50 gauss) applied perpendicular to the current flow which presumably eliminated the effect of injection by the end contacts. This small field is sufficient to move any injected plasma away from the center of the rod[26] (Suhl effect) and out of the 1-mm-diameter path of the acoustic pulse. Since $\omega_c \tau \ll 1$ for B = 50 gauss, this small magnetic field was neglected in our theoretical calculations. One end of the rod-shaped sample was coated with aluminum on which a CdS transducer was evaporated. This end extended into a 9.05-GHz coaxial re-entrant cavity which was excited by a 5-W microwave pulse, $\frac{1}{2}$ to 1 μsec wide. The receiver was the highly sensitive interferometer described previously.[27] With a sample electron concentration of n = 5 × 10^{13} cm^{-3}, the mobility at 4.2°K is strongly electric field dependent[28] below E ≈ 0.1 V/cm, approaching the nitrogen mobility at high electric fields E > 10 V/cm. In addition, the electron temperature is affected by the electric field for fields of the order of 10 V/cm. These two effects complicate the theoretical interpretation of the data. Since most of the data were taken with electric fields above E = 1 V/cm, we have used a value of mobility (i.e., qℓ, where q is the sound wave vector, and ℓ is the electron mean free path) in the theoretical calculations appropriate to the higher electric fields.

It should be noted that the zero-field attenuation decreases about 5 db/cm on increasing the temperature to T = 16°K (see Ref. 29), where the attenuation reaches a minimum. Hence, if the

pulsed electric field were simply heating the sample, an apparent amplification would result. This effect was minimized by bonding one contact end of the sample to the copper cavity with indium and by using low duty cycle (100-Hz) short electric field pulses. Also, in order to monitor the temperature, a carbon resistor thermistor was placed in good thermal contact with the sample.

Calculation of the amplification due to the free electrons requires essentially only a knowledge of the longitudinal dielectric constant ϵ_ℓ. The lattice dispersion relation for a piezoelectric semiconductor can be written[30]

$$\omega = qv_{so} \left[1 + K_p^2 \left(\frac{\kappa\epsilon_o}{\epsilon_\ell} \right) + K_d^2 \left(\frac{\epsilon_\ell - \kappa\epsilon_o}{\epsilon_\ell} \right) \right]^{1/2} \tag{4}$$

where ω and v_{so} are the frequency and sound velocity in the insulating crystal if the piezoelectric coupling is vanishingly small ($K_p^2 \ll 1$). K_p^2 and K_d^2 are the dimensionless piezoelectric and deformation potential coupling parameters, $\kappa\epsilon_o$ is the lattice contribution to the dielectric constant, ϵ_ℓ is the total longitudinal dielectric constant $\epsilon_\ell = \kappa\epsilon_o - \sigma/i\omega$, and σ is the electrical conductivity. Since K_p^2 and K_d^2 are small, the attenuation constant α can be written

$$\alpha = 2q_i = -(K_p^2 + K_d^2) \, q\mathrm{Im} \left(\frac{\kappa\epsilon_o}{\epsilon_\ell} \right) \tag{5}$$

where q_i is the imaginary part of the wave vector, and Im refers to the imaginary part. On substituting the value of $K^2 = K_p^2 + K_d^2 = 3.6 \times 10^{-4}$ obtained previously,[30]

$$\alpha = 2.26 \times 10^2 \, \mathrm{Im} \left(\frac{\kappa\epsilon_o}{\epsilon_\ell} \right) \, \mathrm{db/cm} \quad . \tag{6}$$

The longitudinal dielectric constant was calculated assuming a shifted Maxwellian electron distribution with the effect of the DC electric field on the AC response included through the use of a complex temperature.[31] We note that the classical Boltzmann equation results for the amplification in our experiments differ from the quantum mechanical density matrix results by less than 0.0025 percent, despite the size of the quantity $\hbar q/2mV_o \sim 1$. Also, note that, while the complex temperature results from an exact solution of the AC Boltzmann equation, the density matrix equation does not yield this simple result. As in the classical calculation, the quantum mechanical solution for $\omega\tau \gg 1$ includes the electric field in the AC conductivity exactly through the use of a drifted distribution and a complex temperature. However, when diffusion current is present (i.e., $\omega\tau < 1$), the quantum mechanical solution does not include the DC electric field in this simple manner.[32] Experimental data on the change in attenuation with electric field are shown in Fig. IV-12. We are unable to measure the absolute attenuation at zero electric field; however, the calculated value lies between 6 and 10 db/cm for our measured low-field mobilities ($\mu < 100,000 \, \mathrm{cm}^2/\mathrm{V \, sec}$). The initial sharp decrease in the attenuation is probably the result of the rapid increase of mobility with electric field in this range.

The results of the theoretical calculations are shown in Fig. IV-13. The value of $q\ell = 2$ corresponds to a mobility $\mu \approx 200,000 \, \mathrm{cm}^2/\mathrm{V \, sec}$ which is nearly the experimentally observed mobility at this temperature for fields $>1 \, \mathrm{V/cm}$. The mobility and concentration at $T = 77°K$ were $\mu = 630,000 \, \mathrm{cm}^2/\mathrm{V \, sec}$ and $n = 5 \times 10^{13} \, \mathrm{cm}^{-3}$, respectively.
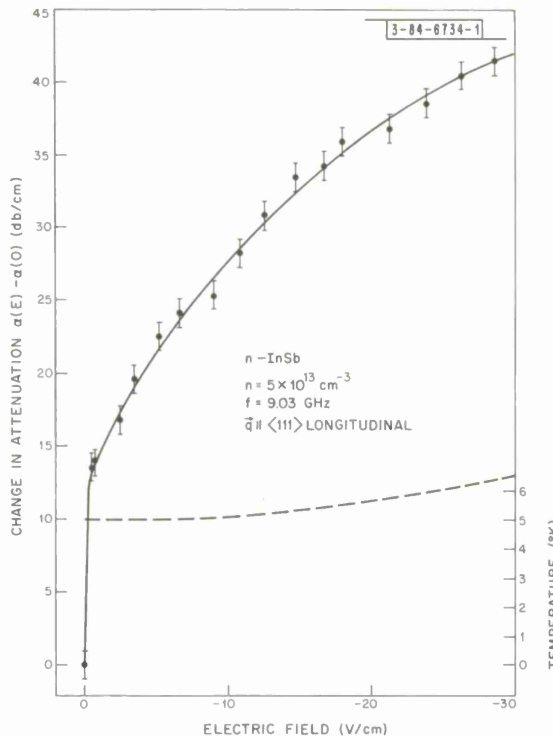
Fig. IV-12. Experimental change in attenuation with electric field.

Fig. IV-13. Theoretical dependence of amplification on electric field.

The considerable discrepancy between the theoretical curve and experimental data may result from a variety of effects, among which are injection at the contacts and the electric field dependence of the electron mobility and temperature. The latter has not been considered and this may introduce a considerable error.

K. W. Nill

B. MAGNETISM

1. Magnetic Properties of MnAs in the High-Pressure Phase

We have continued our study of the magnetic properties of the high-pressure (orthorhombic) phase of MnAs. Our measurements of the magnetic moment vs temperature in a magnetic field of 10 kOe, as reported in the previous Solid State Research Report,[33] have been extended to a pressure of 11 kbars. In addition, we have now studied the magnetic moment vs temperature in various applied fields throughout the pressure range. A set of such measurements (taken at a pressure of 9 kbars), as given in Fig. IV-14, illustrates the flattening of the magnetization curves in an intermediate temperature region, as well as the onset of a low-temperature transition. Re-expressing the data in terms of isotherms, as shown in Fig. IV-15, enables us to define the magnetic state of the sample in pressure-temperature (P-T) space. Thus, Fig. IV-15 illustrates the apparent ferromagnetism in the intermediate temperature region as well as the metamagnetic behavior of orthorhombic MnAs at both higher [Meta (1)] and lower [Meta (2)] temperatures. These two regions are distinguished from each other by the fact that in state Meta (1), $dH_{cr}/dT < 0$,

Fig. IV-14. Variation of magnetic moment of orthorhombic MnAs at 9 kbars with temperature, for various applied magnetic fields.
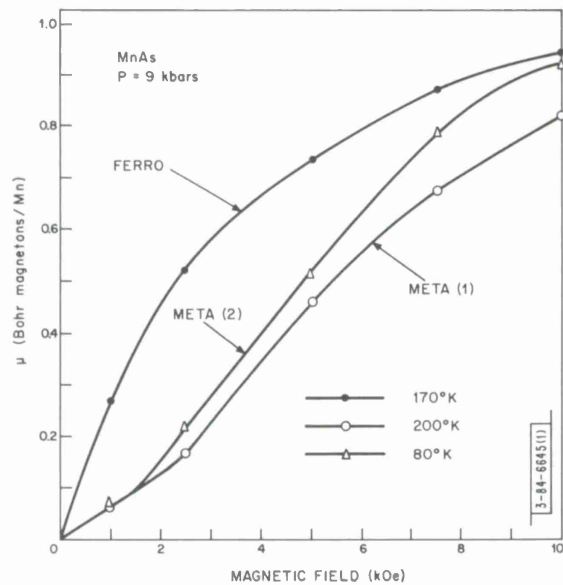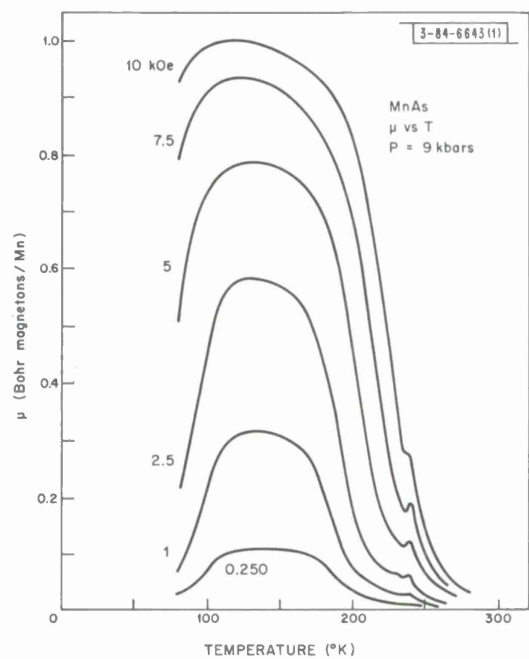
Fig. IV-15. Magnetic moment of orthorhombic MnAs at 9 kbars as function of applied field at various temperatures, indicating both ferromagnetic and metamagnetic behavior.
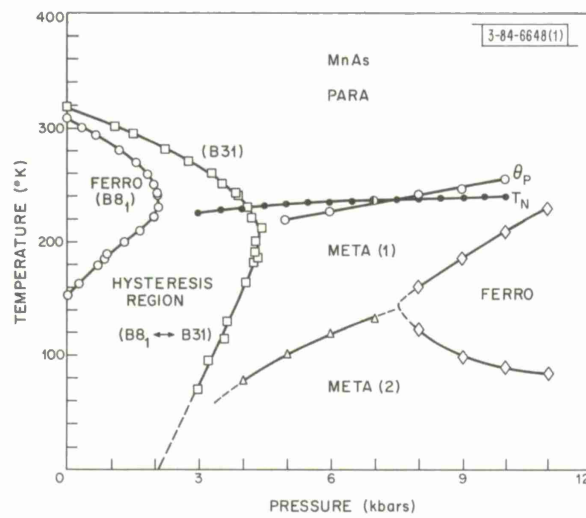
Fig. IV-16. Magnetic phase diagram for MnAs.
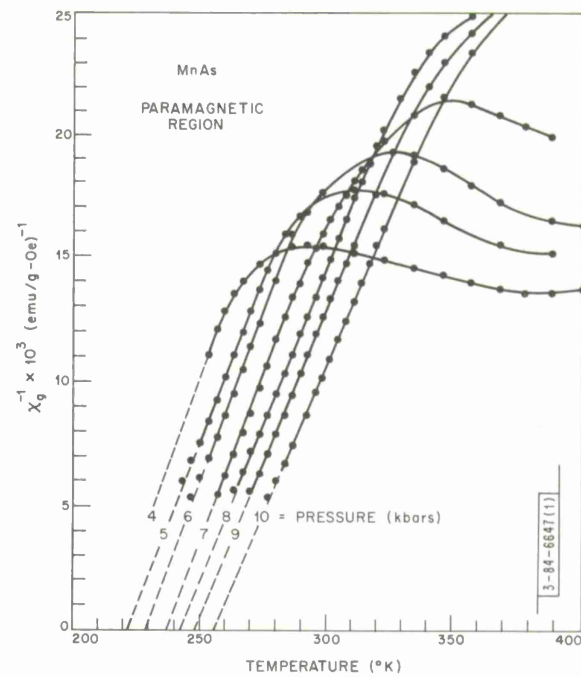
Fig. IV-17. Inverse susceptibility vs temperature curves of orthorhombic MnAs at indicated pressures.

TABLE IV-2		
VALUES OF EFFECTIVE MOMENT AND CURIE TEMPERATURE OF ORTHORHOMBIC MnAs AT VARIOUS PRESSURES, AS DETERMINED FROM PARAMAGNETIC SUSCEPTIBILITY		
Pressure (kbars)	μ_{eff} (Bohr magnetons)	θ_P (°K)
5	1.91	220.5
6	1.87	228
7	1.83	238
8	2.02	242.5
9	2.02	248.5
10	2.06	256

while in Meta (2), $dH_{cr}/dT > 0$; here, H_{cr} is the critical transition field for departure from anti-ferromagnetic behavior. Curves similar to those shown in Figs. IV-15 and IV-16 were obtained for various pressures and temperatures. These enabled us to define the region in P-T space in which the high-pressure phase is ferromagnetic or one of the metamagnetic states. These regions are delineated in Fig. IV-16.

In addition, Fig. IV-16 shows the hexagonal-rhombohedral phase transitions,[34] the Néel temperatures (T_N),[33] and the paramagnetic Curie points Θ_P. These latter points are based on para-magnetic susceptibility data taken just above T_N in the pressure range from 4 to 10 kbars. At these temperatures and pressures, MnAs is still in the B31 phase. The resultant curves of in-verse susceptibility in this region follow a Curie-Weiss relationship, as seen in Fig. IV-17, and the corresponding values of μ_{eff} and Θ_P are given in Table IV-2. The variation of μ_{eff} observed over this pressure range is small and falls within the experimental uncertainties. However, the value of approximately $2\mu_B$ is far below the value $\mu_{eff} = 4.56\mu_B$ which was observed in the hexag-onal phase of MnAs.[35] This indicates that virtually the entire change in μ_{eff} occurs discontinu-ously at the first-order hexagonal-orthorhombic transition, and directly confirms the hypothesis of Goodenough, Ridgley, and Newman[36] that this transition is accompanied by a change from a high- to a low-spin manganese configuration.

The paramagnetic moment value is consistent with the saturation moment value of slightly over $1\mu_B$ obtained in the ferromagnetic state at 11 kbars. In addition, the positive $d\Theta_P/dP$ indi-cates a net increase in ferromagnetic interactions with increasing pressure, which is also con-sistent with the magnetic behavior observed below the ordering temperature.

N. Menyuk
J. A. Kafalas
K. Dwight

2. Magnetic Resonance in Spiral Spin Structure Compounds

In an effort to gain some insight into the nature of the normal modes of a conical spiral sys-tem, we have studied the equilibrium configurations and spin wave spectra for the linear chain model mentioned in the previous Solid State Research Report.[37] In this model, two species of spins, S_A and S_B, are coupled by nearest and next-nearest neighbor A-B and B-B interactions. It is found that there exist ranges of exchange interactions for which a conical spiral ground state is stable. Spin wave spectra have also been computed for a number of conical spiral cases. Figure IV-18 shows the spin wave spectrum for the particular choice (in normalized units) $J_{AB}^1 = 3.5$, $J_{AB}^2 = 1.0$, $J_{BB}^1 = 2.0$, $J_{BB}^2 = 1.0$, and $S_A = 1$, $S_B = 0.8$. These parameters lead to a ferrimagnetic conical spiral structure, with cone angle $\psi_A = 5.81°$, $\psi_B = 121.9°$, and turn angle $74.8°$.

The modes of particular interest in a microwave resonance experiment are those at $\vec{k} = \vec{k}_o$, and $\vec{k} = 0$. For the $\vec{k} = \vec{k}_o$ modes, those marked 1, 2, and 3 in Fig. IV-18 are exchange modes, while the mode marked 4 is the uniform mode. For modes 1 and 4, each conical spiral precesses rigidly about the cone axis, while for modes 2 and 3, the cones distort as they precess about the cone axis (see Fig. IV-19). Modes 2, 3, and 4 all have net oscillating moment in the plane perpen-dicular to the cone axes, while mode 1 has no net moment.

3-84-6796-1
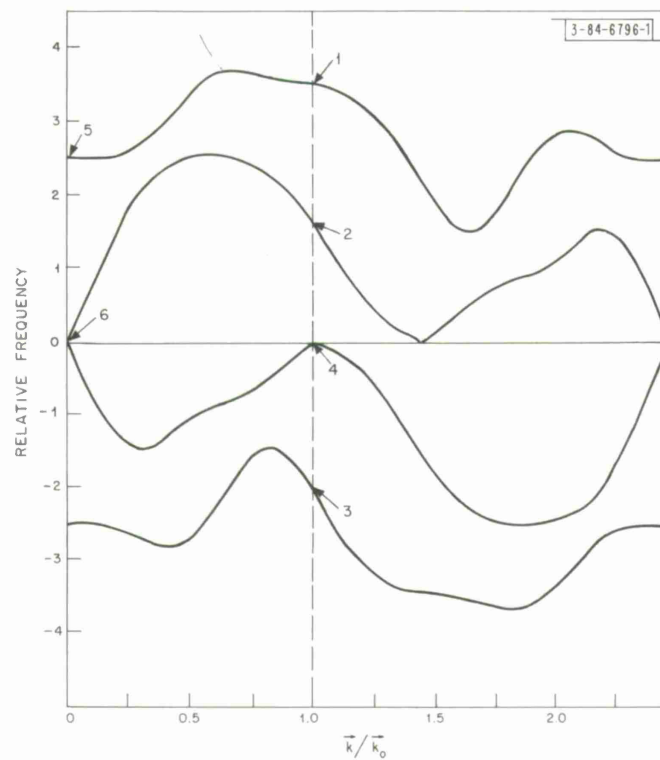
Fig. IV-18. Spin wave spectrum for linear chain-conical spiral configuration.
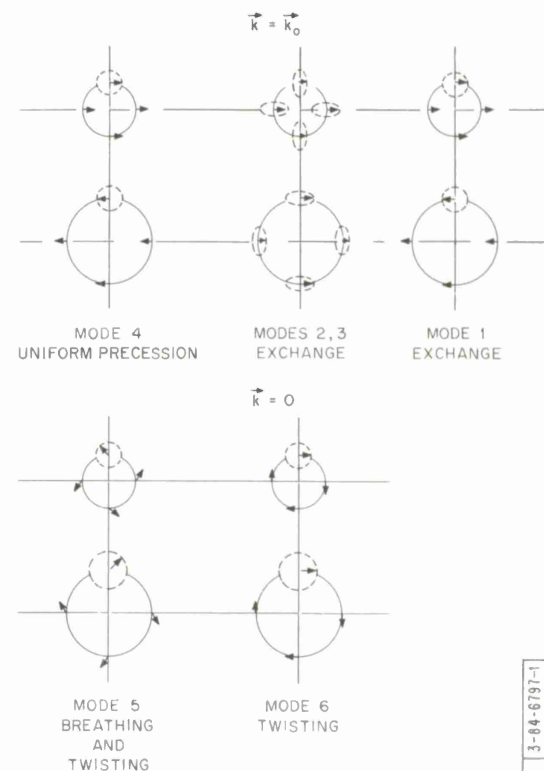
Fig. IV-19. Schematic diagram of spin wave modes of linear chain-conical spiral configuration. Arrows show instantaneous displacement of spins in plane perpendicular to spiral axis.

$\vec{k} = \vec{k}_o$

MODE 4
UNIFORM PRECESSION

MODES 2,3
EXCHANGE

MODE 1
EXCHANGE

$\vec{k} = 0$

MODE 5
BREATHING
AND
TWISTING

MODE 6
TWISTING

3-84-6797-1

For the $\vec{k} = 0$ case, mode 6 is a pure "twisting" mode, with the two cones moving rigidly, and therefore $\omega = 0$. Mode 5 is a "breathing-twisting" mode (see Fig. IV-19), for which the net oscillating moment in the plane vanishes. Each cone separately has an oscillating moment along its cone axis, but the two oscillating moments exactly cancel.

<div align="right">

J. J. Stickler
H. J. Zeiger

</div>

3. Spherical Model as the Limit of Infinite Spin Dimensionality

Consider the Hamiltonian

$$\mathcal{H}^{(\nu)} = -\frac{1}{2} J \sum_{i,j=1}^{N} v_{ij} S_i^{(\nu)} \cdot S_j^{(\nu)} \tag{7}$$

where $S_j^{(\nu)} \equiv [\sigma_1(j), \sigma_2(j), \ldots, \sigma_\nu(j)]$ are ν-dimensional vectors of magnitude $\sqrt{\nu}$. Although it is perhaps not generally appreciated, it seems clear that $\mathcal{H}^{(\nu)}$ reduces to the $S = 1/2$ Ising, classical planar, and classical Heisenberg models for $\nu = 1, 2$, and 3, respectively.

Here we argue that in the limit $\nu \to \infty$, the free energy of $\mathcal{H}^{(\nu)}$ approaches that of the spherical model. This result is of particular current interest, besides the geometrical interpretation it attaches to the spherical model, because of recent evidence[38] that various "critical properties" of $\mathcal{H}^{(\nu)}$ are monotonic functions of ν. Hence, the critical properties of the fairly realistic but hopelessly insoluble Heisenberg model (three-dimensional spins) would appear to be bounded on one side by those of the Ising model (one-dimensional spins) and on the other by those of the spherical model (infinite-dimensional spins). Moreover, the spherical model has in the past been interpreted as a soluble approximation to the Ising model, whereas, in fact, the spherical model would appear to be a much better approximation to the more "realistic" Heisenberg model.

The normalized partition function corresponding to $\mathcal{H}^{(\nu)}$ is

$$Q_N^{(\nu)}(K) = Z_N^{(\nu)}(K)/Z_N^{(\nu)}(0) \tag{8}$$

where

$$Z_N^{(\nu)}(K) = \int_{-\infty}^{\infty} \cdots \int_{-\infty}^{\infty} d\sigma_1(1), \ d\sigma_2(1), \ldots, d\sigma_\nu(1) \ d\sigma_1(2), \ d\sigma_2(2), \ldots, d\sigma_\nu(N)$$

$$\times \prod_{j=1}^{N} \left\{ \delta \left[\nu - \sum_{n=1}^{\nu} \sigma_n^2(j) \right] \right\} \times \exp[K \Sigma_{ij} v_{ij} \Sigma_{n=1}^{\nu} \sigma_n(i) \ \sigma_n(j)] \tag{9}$$

and $K \equiv J/2kT$. The N constraints are then represented as N delta functions, and we obtain

$$Z_N^{(\nu)}(K) = \left(\frac{K}{2\pi i}\right)^N \left(\frac{\pi}{K}\right)^{\nu N/2} \int_{\alpha-i\infty}^{\alpha+i\infty} \cdots \int_{\alpha-i\infty}^{\alpha+i\infty} dt_1, \ldots, dt_N \ \exp[\nu F(K, \{t_j\})] \tag{10}$$

where $F(K, \{t_j\}) \equiv K \Sigma_j t_j - [1/2 \ln \Delta(\{t_j\})]$, and where $\Delta(\{t_j\})$ is the determinant of the quadratic form $\Sigma_{ij} (t_j \delta_{ij} - v_{ij}) \ \sigma_n(i) \ \sigma_n(j)$.

The requirement that $F(K, \{t_j\})$ be stationary leads to the set of conditions

$$K = \frac{1}{2} \left(\frac{\partial}{\partial t_\ell} [\ln \Delta(\{t_j\})] \right)_{t_s} \quad ; \quad \ell = 1, 2, \ldots, N \tag{11}$$

Next, expand $F(K, \{t_j\})$ about the stationary points $\{t_s\}$,

$$F(K, \{t_j\}) = F(K, \{t_s\}) + \frac{1}{2!} \sum_{m, n=1}^{N} \left(\frac{\partial^2 F}{\partial t_m \partial t_n} \right) (t_m - t_s) (t_n - t_s) + \ldots \tag{12}$$

We then factor $\nu F(K, \{t_s\})$ out of the integrand of Eq. (10), calling the remaining integral R. Thus, from Eq. (10),

$$\ln Z_N^{(\nu)}(K) = \frac{1}{2} \nu N \ln [\pi/K] + \nu F(K, \{t_s\}) + \ln R \tag{13}$$

The limiting free energy $\psi^{(\infty)}$ is related to $Z_N^{(\nu)}(K)$ by

$$-\beta \psi^{(\infty)} \equiv \lim_{\nu, N \to \infty} \frac{1}{\nu N} \ln [Z_N^{(\nu)}(K)/Z_N^{(\nu)}(0)] \tag{14}$$

where $\beta \equiv (kT)^{-1}$. From Eq. (13), we obtain

$$-\beta \psi^{(\infty)} = -\frac{1}{2} - \frac{1}{2} \ln 2K + \frac{1}{N} F(K, \{t_s\}) + \lim_{\nu, N \to \infty} \frac{1}{\nu N} \ln R \tag{15}$$

The last term on the right-hand side of Eq. (15) can be shown to be zero. Now, $F(K, \{t_s\}) = NKt_s - [1/2 \ln \Delta(\{t_s\})]$ and $\ln \Delta(\{t_s\}) = \ln 2^N + \ln |(1/2\, t_s \delta_{ij}) - (1/2\, v_{ij})|$. Thus, Eq. (15) is precisely the spherical model free energy.

<div align="right">H. E. Stanley</div>

4. Eigenvalue Degeneracy as a "Mathematical Mechanism" for Phase Transitions

Kac[39] has noted a striking analogy between the Ising model

$$\mathcal{H}_I = -J \sum_{\langle i, j \rangle} S_i^{(1)} S_j^{(1)} \tag{16}$$

(with strong, short-range forces) and the "Kac model"

$$\mathcal{H}_K = -\gamma J \sum_{i, j} e^{-\gamma |i-j|} S_i^{(1)} S_j^{(1)} \tag{17}$$

(with weak, long-range forces for γ small). In the Ising model, the summation is over nearest-neighbor pairs of sites $\langle i, j \rangle$, whereas, in the Kac model, the summation is over all sites i and j in the lattice. Kac observed that (for both models) the onset of a spontaneous magnetization below a certain transition temperature T_c is characterized, mathematically, by the asymptotic degeneracy of the maximum eigenvalue of a certain linear operator.

Since the "mathematical mechanisms" responsible for the phase transitions in a strong, short-range force model and in a weak, long-range force model are identical for "one-dimensional"

(i.e., Ising) spins, it seems natural to inquire whether this same mathematical mechanism is responsible for the phase transitions in other spin dimensionalities. To this end, we consider the Hamiltonians obtained by replacing the one-dimensional scalar spins $S^{(1)}$ in Eqs. (16) and (17) by isotropically interacting ν-dimensional vector spins $S^{(\nu)}$ and obtain

$$\mathcal{H}_I^{(\nu)} = -J \sum_{\langle i, j \rangle} \vec{S}_i^{(\nu)} \cdot \vec{S}_j^{(\nu)} \tag{18}$$

$$\mathcal{H}_K^{(\nu)} = -\gamma J \sum_{i, j} e^{-\gamma |i-j|} \vec{S}_i^{(\nu)} \cdot \vec{S}_j^{(\nu)} \quad . \tag{19}$$

Thus far, we have observed that, for Eq. (18) with $\nu = 1$, 2, 3, and ∞, the onset of infinite-range order may indeed be described mathematically by the collapse of the entire (discrete) eigenvalue spectrum of an appropriate linear operator into a single value. In particular, the spin-spin correlation function $\langle \vec{S}_O^{(\nu)} \cdot \vec{S}_R^{(\nu)} \rangle$ may be expressed as $[\lambda_1^{(\nu)}/\lambda_O^{(\nu)}]^R$, where λ_O is the largest, and λ_1 the next-largest, eigenvalue. Hence, the spontaneous magnetization $M \equiv \lim_{R \to \infty} \langle \vec{S}_O^{(\nu)} \cdot \vec{S}_R^{(\nu)} \rangle^{1/2}$ is zero so long as $\lambda_1^{(\nu)} < \lambda_O^{(\nu)}$, but it becomes nonzero as the eigenvalues become degenerate.

H. E. Stanley

5. Finite Temperature Single-Slater Determinant Theory

We have applied[40] standard temperature-dependent Hartree-Fock (HF) theory (without any symmetry restrictions) to a system of N infinitely separated hydrogen atoms in zero external fields. We find that, as temperature $T \to 0$, it leads to the entropy $S \to 0$ rather than to the correct value $S \to Nk \ln 2$, although the zero-temperature energy and the absence of spin ordering are correctly predicted. Another, closely related failure of that theory is that as $T \to 0$, the spin susceptibility $\chi \to 0$ rather than ∞ as in the (correct) Curie law. This serious failure was traced to the use of a one-electron operator for the effective or approximate Hamiltonian $\tilde{H}$ [defined in Eq. (24) below]. Furthermore, a new finite-temperature HF theory, still involving single determinants as approximate energy eigenstates, was shown to give the correct behavior for the system of isolated hydrogen atoms.

We describe here some of the essential details of this new generalization of HF theory. Basic is the well-known variational principle[41]

$$F(\rho) \equiv \text{tr}(H - \mu N) \rho + kT \, \text{tr} \, \rho \, \ln \rho \geqslant F_T \tag{20}$$

where the true free energy, appropriate to a grand canonical ensemble, is

$$F_T = -kT \ln \text{tr} \exp[-\beta(H - \mu N)] \tag{21}$$

ρ is any density operator, $\beta = 1/kT$, and H is the Hamiltonian

$$H = \Sigma \, t_{ij} c_i^+ c_j + \frac{1}{2} \Sigma \, v_{ij,k\ell} c_i^+ c_j^+ c_\ell c_k \quad ; \tag{22}$$

c_i^+ are the usual fermion creation operators for some set of orthonormal, one-electron states φ_i. The equality of Eq. (20) is attained when ρ is the true density operator ρ_T, where

$$\rho_T = Z^{-1} \exp\left[-\beta(H - \mu N)\right] \quad . \tag{23}$$

It is convenient to define an approximate Hamiltonian $\widetilde{H}$ such that

$$\rho = \exp\left[-\beta(\widetilde{H} - \mu N)\right] / \mathrm{tr} \, \exp\left[-\beta(\widetilde{H} - \mu N)\right] \quad . \tag{24}$$

Standard T-dependent HF theory is derived from Eq. (20) as follows. First, $\widetilde{H}$ is restricted to be a one-electron operator

$$\widetilde{H} \equiv \Sigma \, \epsilon_i N_i \qquad \text{(standard HF theory)} \tag{25}$$

where N_i are the occupation number operators for a set of one-electron states ψ_i (called "orbitals," involving both space and spin, in general), and ϵ_i are c-numbers. The ψ_i and ϵ_i are then chosen to minimize $F(\rho)$, yielding the standard T-dependent HF equations

$$(\psi_i, t\psi_j) + \Sigma_k \, [(\psi_i\psi_k, v\psi_j\psi_k) - (\psi_i\psi_k, v\psi_k\psi_j)] \, \overline{N}_k = \epsilon_i \delta_{ij} \tag{26}$$

where

$$\overline{N}_k \equiv \mathrm{tr} \, \rho \, N_k = 1 / \exp\left[\beta(\epsilon_i - \mu) + 1\right] \quad . \tag{27}$$

As indicated by Blatt,[41] this "standard T-dependent HF theory" (which he calls "Husimi theory") is a natural extension of zero-temperature Hartree-Fock theory to finite temperature.

However, it is not the only such extension. Our purpose here is to describe another, more general, and quite natural extension. Recall that the basic idea of zero-temperature HF theory is to look for a single Slater determinant D_o which minimizes the energy $(D, HD)/(D, D)$ over all Slater determinants D. Since the eigenfunctions of the $\widetilde{H}$ in Eq. (25) are determinants, it is clear that the minimum free energy computed with Eq. (25) will, as $T \to 0$, approach $E_o = (D_o, HD_o)/(D_o, D_o)$, the correct zero-temperature HF value. Clearly, all that is needed for this is that all the eigenfunctions of $\widetilde{H}$ be single Slater determinants. But $\widetilde{H}$, as given in Eq. (25), is by no means the most general form such that all the eigenfunctions are single determinants. For example, an operator of the form $\Sigma \, \epsilon_i N_i + \Sigma \, \epsilon_{ij} N_i N_j$ would also have a complete set of single determinantal eigenfunctions — in fact, $\widetilde{H}$ would have single determinantal eigenfunctions if it were an arbitrary function $E(N_1, N_2, \dots)$ of the occupation number operators. Thus, we are led to a new extension to finite temperature of zero-temperature HF theory — choose the ψ_i and the function $E(N_1, N_2, \dots)$ to minimize the free energy F. This theory is just as natural as the standard or Husimi extension, since it has single Slater determinants as "approximate energy eigenfunctions";[†] furthermore, it can be expected to be "better" in that it will probably yield a lower free energy. It clearly cannot give a higher free energy.

The formal minimization of F in the new context can be carried out. It requires that the function E be

$$E(N_1, N_2, \dots) = \Sigma \, (\psi_i, t\psi_i) \, N_i + \frac{1}{2} \Sigma \, [(\psi_i\psi_j, v\psi_i\psi_j)$$
$$- (\psi_i\psi_j, v\psi_j\psi_i)] \, N_i N_j \tag{28}$$

[†] We feel that the most general $\widetilde{H}$ having its eigenfunctions be Slater determinants would lead to a theory which should be considered the most general extension to finite temperature of zero-temperature HF theory. We have not shown that the class of $\widetilde{H}$'s considered here has that degree of generality.

(which is just the energy of the determinant defined by occupation numbers ... N_i ...), and that the ψ_i be solutions of

$$(\overline{N}_i - \overline{N}_j)(\psi_i, t\psi_j) + \sum_k [(\psi_i\psi_k, v\psi_j\psi_k) - (\psi_i\psi_k, v\psi_k\psi_j)]\overline{(N_i - N_j)N_k} = 0 \qquad \text{all } i \neq j \quad . \qquad (29)$$

Note the similarity between these and the standard HF equations [Eq. (26)]; if it were not for the terms in E which are quadratic in the N's, the average in Eq. (29) $\overline{(N_i - N_j)N_k}$ would factor into $(\overline{N}_i - \overline{N}_j)\overline{N}_k$, and cancellation of $\overline{N}_i - \overline{N}_j$ would lead back to Eq. (26) for $i \neq j$.

As we have said, this theory completely corrects the physically serious deficiency of the standard theory in the case of infinitely separated hydrogen atoms, but we will not go into the details here. At present, we are studying this theory as applied to hydrogen atoms separated by large but finite distances.

<div align="right">T. A. Kaplan</div>

C. LASER SCATTERING AND NONLINEAR EFFECTS

1. Hypersonic Attenuation in Quartz by Thermal Brillouin Scattering

The velocity and attenuation of 28-GHz longitudinal phonons along the x-axis of α-quartz have been measured in a temperature range from 300° to 600°K. High-resolution Brillouin scattering techniques are employed in this regime where conventional ultrasonics techniques are not applicable. The Brillouin spectrometer consists of a single-mode He-Ne laser and a multiscanned confocal spherical Fabry-Perot interferometer. Photoelectron count data from a low dark current photomultiplier are accumulated in a multichannel analyzer for arbitrarily long times to improve the signal-to-noise ratio.

The velocity, or Brillouin shift, variation with temperature agrees within experimental error with previous low-frequency quartz-controlled oscillator measurements. The hypersonic attenuation is obtained from the spectral width of the Brillouin lines and may be compared with theoretical extrapolations of ultrasonics data. There is order of magnitude agreement with the single relaxation theories of Woodruff and Ehrenreich[42] and of Bömmel and Dransfeld[43]; however, both theories generally overestimate the absorption, and poorly represent the details of the temperature dependence.

Further work is in progress to extend the temperature range of the measurements.

<div align="right">A. S. Pine</div>

2. Light Scattering from Single-Particle Electron and Hole Excitations in Semiconductors

Light scattering has been observed for the first time from screened single-particle electron excitations in GaAs, InP, AlSb, and CdTe, as well as from the screened single-particle hole excitations in p-type GaAs doped with cadmium, zinc, and magnesium. The Raman scattering from plasmons and coupled plasmons and phonons,[44] as well as the polarization properties[45] of the scattered light from these excitations, have been reported previously. Both these cases dealt with the collective excitations of the electron gas in a solid. Present results yield the single-particle excitation spectrum of the electron gas. The single-particle scattering is compared with effective-mass calculations based on simple parabolic bands,[46] which involves scattering from

electron density fluctuations, as well as a more recent effective-mass calculation which predicts a large enhancement due to nonparabolicity.[47] The experimental results, however, are in disagreement with both of those theories.

The scattered light was generated using a 1.06-μ YAG:Nd^{3+} laser which could operate with a continuous output power in excess of 10 W. Figure IV-20 shows the Raman spectrum of an n-type GaAs sample at 300°, 30°, and 5°K. The peaks labeled L_-, L_+, and TO have been described elsewhere,[45] and refer to the coupled modes of the longitudinal optical phonons and the plasmons (L_-, L_+), and the transverse optical phonon (TO). The scattering from the single-particle excitation spectrum of the conduction electrons is seen at lower frequencies near the laser line. At
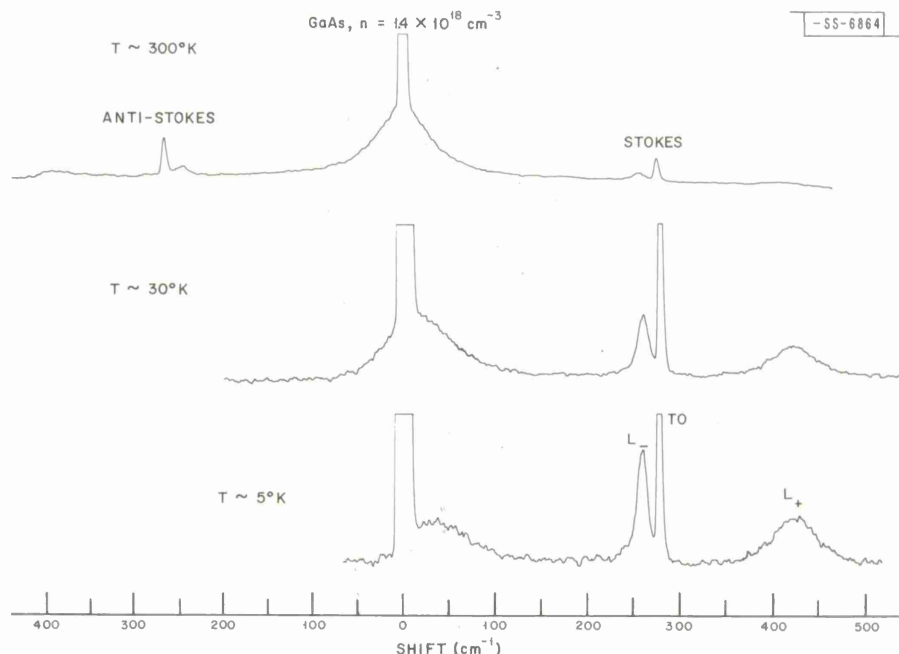

Fig. IV-20. Raman spectrum of GaAs (n = 1.4×10^{18} cm^{-3}), at 300°, 30°, and 5°K. Scattering angle was 90° with incident and scattered light propagating along [100] crystal axes.

T = 0°K, the single-particle excitation spectrum comes from electrons with momentum $\vec{p}$ that are excited from occupied states below the Fermi surface to unoccupied states just above the Fermi surface with momentum $\vec{p} + \vec{q}$, where $\vec{q}$ is the momentum change of the scattered electron. At T = 0°K and for infinite lifetime, the existing theories[46,47] predict a continuum spectrum increasing linearly with ω to a peak near $0.7\,qv_F$, for the parameter values involved here, and cutting off at qv_F, where v_F is the Fermi velocity. Samples with electron concentrations ranging from 2×10^{15} to 2.8×10^{18} cm^{-3} were measured. At low temperature, the single-particle spectrum, while smeared by a finite collision time, did show a cutoff consistent with $\omega = qv_F$. At higher temperatures, more electrons can participate in the scattering as the electron distribution becomes Maxwellian. In the high-temperature limit, the spectral shape of the scattered light should resemble[47] a Maxwellian velocity distribution, which was found to be consistent with the experimental results. In the p-type GaAs, scattering from both the heavy and light hole

single-particle excitations was observed at 300°K in samples with hole concentrations of about 1×10^{16} cm^{-3}. A more complete discussion of these results is published elsewhere.[48]

A. Mooradian

3. Steady-State Thermal Defocusing of Laser Light

In the previous Solid State Research Report,[49] the time dependence of thermal defocusing of laser light was discussed experimentally and the theory was presented.[50] We have carried out further work on the steady state and the approach to steady state, which includes a number of new experimental results. A steady-state condition arises when the temperature change due to heat deposition is just counterbalanced by that due to either heat conduction out of the region of the beam or convection currents where material is transported from the volume. In the case of convection, the hot material rises and is replaced by cooler material from below. As a result, a vertical asymmetry will develop for a horizontal laser beam, and the beam will appear to be bent downward and considerably distorted. This is to be contrasted with conduction which is cylindrically symmetric, and should therefore result in no distortions.

Examining convection more carefully shows that the acceleration a, which a particle experiences in the center of the beam, will be proportional to the total power per unit volume absorbed, which is approximately αI; here, α is the absorption coefficient, and I is the incident intensity. Also, one would expect convection to be important when $(1/2) \times a t_C = q$, where t_C is the convection time constant, and q is the characteristic vertical dimension associated with the beam. In the case of a horizontal laser beam, q is the beam diameter d_o. From this relation, it follows that

$$t_C \propto 1/\sqrt{a} \propto 1/\sqrt{\alpha I} \quad . \tag{30}$$

The acceleration is also proportional to the viscosity of the material. In Fig. IV-21, a plot of the time to reach a maximum beam diameter t_{max} vs $1/\alpha I$ is presented for all our CCl$_4$ data. However, t_{max} differs from the convection time by only a constant. Also included is the best straight line with a slope of $1/2$, and it is clear that the fit is quite good.

The theory for conduction effects was presented by Gordon, et al.,[51] and was discussed further in Ref. 50 where it was indicated that $1/t$ should be replaced by $1/t + 1/t_c$, where

$$t_c = \frac{d^2 K}{16 \rho C_p} \tag{31}$$

K = thermal conductivity, ρ = density, and C_p = heat capacity at constant pressure. In order to study conduction effects, it is necessary to make the conduction time very much shorter than the convection time. There are at least three ways
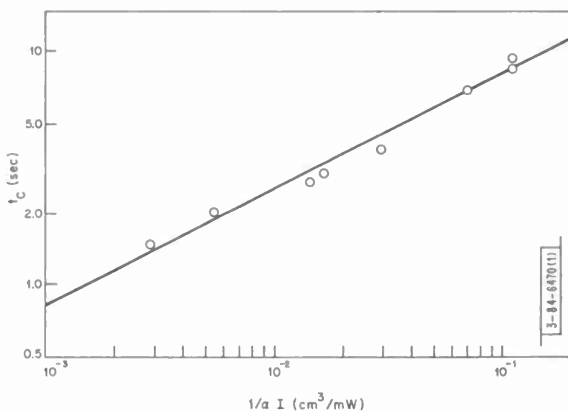

Fig. IV-21. A log-log plot of absorbed power per unit volume αI dependence of convection time, demonstrating square-root dependence of t_C on $(\alpha I)^{-1}$. Liquid here is CCl$_4$, with iodine as absorber.

in which this may be accomplished. The first method is to change the liquid from a material whose ratio of conduction time to convection time is small, to one whose ratio is large. A second technique is to change the direction of propagation of the beam from horizontal to vertical. Now, instead of $q = d_o$, q will be of the order of the cell length ℓ, or $1/\alpha$, depending on which is shorter. Thus, the convection time is greatly increased without changing the conduction time. A third method is to use very low absorption lengths $1/\alpha$, as in Ref. 51. The first two of these techniques were tried, and some results are presented in Fig. IV-22. Data were taken with a vertical laser beam and a 10-cm long vertical cell of both CS_2 (curve A) and CCl_4 (curve B). In both cases, the intensity ($0.8 \, W/cm^2$), beam diameter (0.294 cm), and absorption length (9.7 cm)
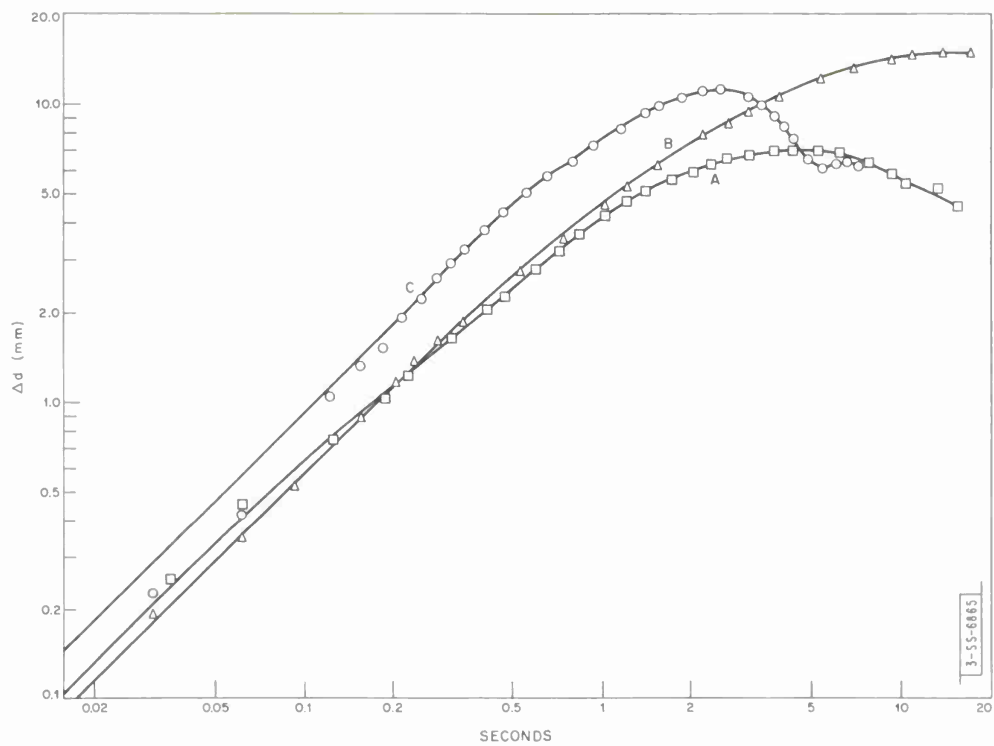

Fig. IV-22. A log-log plot of time dependence of beam diameter change for 10-cm liquid cell containing small amounts of iodine, which results in $1/\alpha = 9.7$ cm. For curves A (CS_2) and B (CCl_4), both laser beam and cell are vertical. For curve (C), beam propagates horizontally and cell contains CS_2.

were the same. Also, in both cases, cylindrically symmetric patterns resulted for the entire time development. Using the theory for a parabolic intensity profile[51] gives the conduction times of t_c (CCl_4) = 7.33 sec, and t_c (CS_2) = 4.33 sec. Curve B can be very accurately reproduced theoretically by using this conduction time for CCl_4 and replacing $1/t$ by ($1/t + 1/t_c$). Also given in Fig. IV-22 is a comparison of the vertical cell data for CS_2 (curve A) with that of a horizontal cell with the same constants (curve C). The exception is that the input laser intensity was ~50-percent higher in the horizontal cell, causing the intercept to be 50-percent larger in this case. A pronounced ringing or underdamped character was displayed by the change in beam diameter Δd for the case of CS_2 in both the vertical and horizontal cell arrangements. The period of the oscillations was much longer for the vertical than for the horizontal cell and, in both cases, the

oscillations were highly damped. Apparently, the value of q increased when switching from the horizontal to vertical cell, but not by as much as expected ($1/d_o\alpha = 32$). Probably because of this, only the early effects of conduction could adequately be predicted by the theory in the case of the CS_2 vertical cell data. More careful analysis of the CCl_4 data indicated that this ringing was also present in the horizontal, but not in the vertical, cell data. The reason the theory does not predict this oscillation undoubtedly lies with two approximations. One is that

$$\int_\infty^t I(t') \, dt' = It \quad . \tag{32}$$

If the past history of the intensity profile is included with the instantaneous variations, an effective time lag should result, thus causing the oscillations. A second reason is that replacing $1/t$ by $(1/t + 1/t_c)$ is correct only to first order, and higher order terms may be significant for some situations.

<div align="right">R. L. Carman
P. L. Kelley</div>

4. Single-Mode Operation of a High-Power Pulsed Ruby Laser

a. Transverse-Mode Selection

Our most reliable transverse-mode selection technique employed a diamond pinhole and two long focal length lenses, as illustrated in Fig. IV-23(a). The resulting cavity length is approximately 1.5 meters. The output beam from this configuration, using the prism as a Q-switch, is
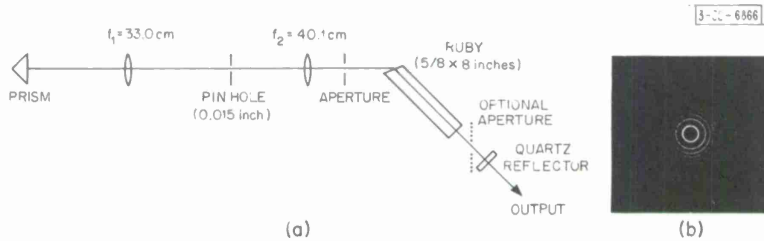

Fig. IV-23. (a) Schematic illustrating experimental arrangement used for transverse-mode selection. (b) Interferogram of non-Q-switched longitudinal-mode structure made with a Fabry-Perot etalon (inter-order spacing 11.8 GHz, resolution ~600 MHz).

a 4-mm-diameter beam with a 0.5- (theoretical limit) to 1-mrad divergence, and a power of 0.1 to 1 MW which is limited by air breakdown in the pinhole. When the prism was fixed and Q-switching was accomplished with a passive dye, then peculiar near-field patterns as well as air breakdown in the pinhole were unavoidable, even with total output power as low as 50 kW. The air breakdown appears to produce a plasma which is opaque, and thus cuts off further lasing.

In the case of the passive Q-switch, a second method of transverse-mode selection was also tried; this consisted of removing the pinhole and placing a second aperture (optional aperture) as indicated in Fig. IV-23(a). Both apertures were identical in size and centered on a common axis. Using 4-mm-diameter apertures, the laser output consisted of three beams, each approximately 1 mm in diameter with about 1.5-mrad divergence. It was concluded that the passive dye used in conjunction with a flame fusion-grown ruby produces spatial inhomogeneities whose characteristic dimensions are too small to render these beams useful.

For the case of the pinhole, the existence of several diffraction-limited hot spots could result in power densities high enough to cause localized air breakdown and, from the ensuing scattering and absorption, a peculiar output near-field pattern. Using the passive dye as a mode-locking element, the requirements on spatial inhomogeneities may well be too high for reliable operation of a diffraction-limited mode-locked laser.

b. Longitudinal-Mode Selection

For non-Q-switched operation, the arrangement in Fig. IV-23(a) produced sufficient mode selection near threshold to allow for operation with linewidths of less than 600 MHz, the resolution limit of our present Fabry-Perot interferometer; i.e., less than six modes were present. A typical interferogram is shown in Fig. IV-23(b). An interferometer with a resolution less than 100 MHz is now being constructed to confirm single-mode operation.

When the laser was Q-switched by rotating a prism, the scheme illustrated in Fig. IV-23(a) was insufficient for producing single-longitudinal-mode operation. By adding a second feedback arrangement, which comprised the second arm of an inverted Michelson interferometer, single-mode operation was obtained. The 45° beamsplitter had a 60-percent reflectivity, while the remaining mirror had a 100-percent reflectivity. The only mode which will oscillate in this scheme is the one for which reflection from the 100-percent mirror destructively interferes with the light directly reflected out of the cavity by the beamsplitter. Reliable longitudinal-mode selection requires stable mirror mounts; we are now investigating this problem.

<div style="text-align: right">

R. L. Carman
F. H. Perry

</div>

REFERENCES

1. J. Hanus, J. Feinleib, and W. J. Scouler, Phys. Rev. Letters 19, 16 (1967), DDC 658919; H. Ehrenreich, H. R. Philipp, and D. J. Olechna, Phys. Rev. 131, 2469 (1963); U. Gerhardt (to be published); H. Ehrenreich and H. R. Philipp, Phys. Rev. 128, 1622 (1962).

2. J. W. D. Connolly, Phys. Rev. 159, 415 (1967); B. Segall, Phys. Rev. 125, 109 (1962); G. A. Burdick, Phys. Rev. 129, 138 (1963).

3. D. Beaglehole, Proc. Phys. Soc. 85, 1007 (1965).

4. K. Schröder and D. Önengüt, Phys. Rev. 162, 628 (1967).

5. J. Friedel, J. Phys. Rad. 19, 573 (1958).

6. P. W. Anderson, Phys. Rev. 124, 41 (1961).

7. N. D. Lang and H. Ehrenreich, Phys. Rev. 168, 605 (1968).

8. D. H. Seib and W. E. Spicer, Bull. Am. Phys. Soc. II 13, 486 (1968).

9. Solid State Research Report, Lincoln Laboratory, M. I. T. (1968:1), p. 34, DDC 668762.

10. S. H. Groves and W. Paul, Phys. Rev. Letters 11, 505 (1963).

11. S. H. Groves, R. N. Brown, and C. R. Pidgeon, Phys. Rev. 161, 779 (1967).

12. B. L. Booth and A. W. Ewald, to be published in Phys. Rev.

13. C. R. Pidgeon and R. N. Brown, Phys. Rev. 146, 575 (1966).

14. C. R. Pidgeon and S. H. Groves, II-VI Semiconducting Compounds, 1967 International Conference, edited by D. G. Thomas (W. A. Benjamin, Inc., New York, 1967), p. 1080.

15. R. Kaplan, Phys. Rev. Letters 20, 329 (1968).

16. B.J. Roman and A.W. Ewald, Bull. Am. Phys. Soc. 13, 408 (1968).

17. E.D. Hinkley and A.W. Ewald, Phys. Rev. 134, A1261 (1964).

18. D.M.S. Bagguley, M.L. Robinson, and R.A. Stradling, Phys. Letters 6, 143 (1963).

19. H.T. Tohver and G. Ascarelli, Bull. Am. Phys. Soc. 11, 94 (1968).

20. M.L. Robinson, Phys. Rev. Letters 17, 963 (1966).

21. E.O. Kane, J. Phys. Chem. Solids 1, 249 (1957).

22. C.R. Pidgeon and S.H. Groves, Phys. Rev. Letters 20, 1063 (1968).

23. B.W. Batterman and D.R. Chipman, Phys. Rev. 127, 690 (1962).

24. R.W. James, The Optical Principles of the Diffraction of X-rays (G. Bell and
    Sons, Ltd., London, 1958), Chapter II.

25. Y. Sakisaka and I. Sumoto, Proc. Math.-Phys. Soc. Japan 13, 211 (1931).

26. I. Melngailis and R.H. Rediker, Proc. IRE 50, 2428 (1962).

27. K.W. Nill and A.L. McWhorter, 1965 Ultrasonics Symposium, Boston, Massa-
    chusetts, 1 – 4 December 1965.

28. H. Miyazawa and H. Ikoma, Solid State Commun. 5, 229 (1967).

29. K.W. Nill and A.L. McWhorter, J. Phys. Soc. Japan (Suppl.) 21, 755 (1966),
    DDC 646478.

30. K.W. Nill, "Microwave Magnetoacoustic Effects in Indium Antimonide," Ph.D.
    Thesis, Department of Electrical Engineering, M.I.T. (13 May 1966) (unpublished).

31. D. Pines and J.R. Schrieffer, Phys. Rev. 124, 1387 (1961).

32. K.W. Nill, to be published.

33. Solid State Research Report, Lincoln Laboratory, M.I.T. (1968:1), p.41, DDC 668762.

34. Ibid. (1967:4), pp.39 – 41, DDC 665465.

35. C. Guillaud, J. Phys. Rad. 12, 223 (1951).

36. J.B. Goodenough, D.H. Ridgley, and W.A. Newman, Proceedings of the
    International Conference on Magnetism, Nottingham, England, September 1964
    (Gresham Press, Old Woking, Surrey, England, 1964), p.542.

37. Solid State Research Report, Lincoln Laboratory, M.I.T. (1968:1), p.42, DDC 668762.

38. H.E. Stanley, Phys. Rev. Letters 20, 589 (1968).

39. M. Kac, 1966 Brandeis Institute for Theoretical Physics, edited by M. Chretien
    (Gordon and Breach, New York, 1968).

40. T.A. Kaplan, Bull. Am. Phys. Soc. 13, 386 (1968).

41. J.M. Blatt, Theory of Superconductivity (Academic Press, New York, 1964), p.396 and p.265.

42. T.O. Woodruff and H. Ehrenreich, Phys. Rev. 123, 1553 (1961).

43. H.E. Bömmel and K. Dransfeld, Phys. Rev. 117, 1245 (1960).

44. A. Mooradian and G.B. Wright, Phys. Rev. Letters 16, 999 (1966), DDC 642230.

45. A. Mooradian and A.L. McWhorter, Phys. Rev. Letters 19, 849 (1967), DDC 668193.

46. P.M. Platzman, Phys. Rev. 139, A379 (1965); A.L. McWhorter, Physics of Quantum
    Electronics, edited by P.L. Kelley, B. Lax, and P.E. Tannenwald (McGraw-Hill,
    New York, 1966), p.111.

47. P.A. Wolff, Phys. Rev., to be published.

48. A. Mooradian, Phys. Rev. Letters 20, 1102 (1968).

49. Solid State Research Report, Lincoln Laboratory, M.I.T. (1968:1), p.49, DDC 668762.

50. R.L. Carman and P.L. Kelley, Appl. Phys. Letters 12, 241 (1968).

51. J.P. Gordon, R.C.C. Leite, R.S. Moore, S.P.S. Porto, and J.R. Whinnery,
    J. Appl. Phys. 36, 3 (1965).

DOCUMENT CONTROL DATA - R&D

(Security classification of title, body of abstract and indexing annotation must be entered when the overall report is classified)

1. ORIGINATING ACTIVITY (Corporate author)	2a. REPORT SECURITY CLASSIFICATION
Lincoln Laboratory, M.I.T.	Unclassified
	2b. GROUP
	None

3. REPORT TITLE

Solid State Research

4. DESCRIPTIVE NOTES *(Type of report and inclusive dates)*

Quarterly Technical Summary — 1 February through 30 April 1968

5. AUTHOR(S) *(Last name, first name, initial)*

McWhorter, Alan L.

6. REPORT DATE	7a. TOTAL NO. OF PAGES	7b. NO. OF REFS
15 May 1968	80	95

8a. CONTRACT OR GRANT NO.	9a. ORIGINATOR'S REPORT NUMBER(S)
AF 19(628)-5167	
b. PROJECT NO.	Solid State Research (1968:2)
649L	
c.	9b. OTHER REPORT NO(S) *(Any other numbers that may be assigned this report)*
d.	ESD-TR-68-88

10. AVAILABILITY/LIMITATION NOTICES

This document has been approved for public release and sale; its distribution is unlimited.

11. SUPPLEMENTARY NOTES	12. SPONSORING MILITARY ACTIVITY
None	Air Force Systems Command, USAF

13. ABSTRACT

This report covers in detail the solid state research work at Lincoln Laboratory for the period 1 February through 30 April 1968. The topics covered are Solid State Device Research, Optical Techniques and Devices, Materials Research, and Physics of Solids.

14. KEY WORDS

solid state devices	electron band structure	photovoltaic detectors	magnetoabsorption
optical techniques and devices	magnetism	crystal growth	laser scattering
	laser research	magnetoreflection	Raman scattering
materials research	infrared	magneto-optical research	